Universidad Autónoma de Madrid
Escuela Politécnica Superior

Trabajo Fin de Máster

Development of Advanced Techniques for Efficient Simulation and Fast 3D-printed Prototypes of Horn Antennas

Máster Universitario en
Ingeniería de Telecomunicación

Lucas Polo López
Junio 2016

Development of Advanced Techniques for Efficient Simulation and Fast 3D-printed Prototypes of Horn Antennas

Autor: Lucas Polo López
Tutor: Jorge A. Ruiz Cruz

RFCAS
Dpto. de Tecnología Electrónica y de las Telecomunicaciones
Escuela Politécnica Superior
Universidad Autónoma de Madrid
Junio 2016

Abstract

Horn antennas are widely used in communication systems. They are typically used as feeds for reflector antennas and, due to its robustness, they can also be mounted on the fuselage of airplanes and are used on-board satellites. Horn antennas also present great directivities, gains, and efficiencies. The main drawback of this antenna family is (as it happens with most microwave devices) that they are complicated to simulate with full-wave electromagnetic methods.

Most of the commercial tools available at the market for simulating microwave devices (CST Microwave Studio, HFSS,...) use general numerical methods such as finite elements or finite differences in time or frequency domain, whose main advantage is that they can tackle a wide range of problems. The main drawback of these general methods is that this generality makes the simulation inefficient, causing long computation times for some problems in comparison with other more analytical techniques.

This leads to the first goal of this work, which consists in developing a software tool capable of analysing, simulating and designing horn antennas efficiently based on a numerical method, called Mode-Matching, which is known to be very efficient for this type of problems. In order to compute the radiation pattern of the antennas, the radiation integral of the electromagnetic field at the horn aperture has to be calculated. An important part of this work will be devoted to the derivation of the necessary formulas that will allow to compute these integrals, since the literature does not usually cover these derivations with enough detail (typically the integrations are just solved for a simplified case), while here we will address the complete modal excitations. The use of this software would not only lead to shorter simulation and design times but would also permit to design horn antennas using low/moderate performance computers like notebooks.

The construction of horn antennas (and once again, of most microwave devices) is usually a process with a high economic cost. But in the recent years, additive manufacturing techniques like 3D printing have opened the door to the low cost manufacturing of three-dimensional structures. Therefore the second goal of this work is to develop a construction process for the prototyping of horn antennas using a 3D printer. This process must be fast and inexpensive.

To test the validity of these manufacturing techniques different devices will be constructed like conical, pyramidal and choke horns. In addition hollow and gap waveguides will be also studied and their performance will be evaluated. The fabrication of these devices will be performed locally by the author of this work. Moreover, the resulting devices will be also fully experimentally characterized in this work, in order to compare their characteristics with the simulations performed using the developed models. This will produce a convergence of the two goals of the work, joining the advanced electromagnetic modelling of microwave devices with one of the newest and trendiest manufacturing techniques.

Keywords

3D printer, additive manufacturing, antenna, beamwidth, circular waveguide, corrugations, directive gain, directivity, discontinuity, evanescent mode, far field, fundamental mode, gap waveguide, generalized scattering matrix, high order mode, horn, main lobe, microwave, Mode-Matching, perfect electric wall, perfect magnetic wall, PEW, PMW, propagating mode, radiation pattern, rectangular waveguide, scattering matrix, side lobe, waveguide, waveguide mode

Resumen

Las antenas de bocina son ampliamente usadas en los sistemas de comunicación. Típicamente se utilizan como alimentadores de antenas reflectoras y, debido a su robustez, también pueden montarse directamente sobre el fuselaje de aviones o usuarse a bordo de satélites. Las bocinas también tienen la virtud de presentar grandes valores de directividad, ganancia y eficiencia. La principal desventaja de esta familia de antenas es (como suele ocurrir con la mayoría de los dispositivos de microondas) que son bastante complicadas de simular con métodos electromagnéticos de onda completa.

La mayoría de las herramientas comerciales existentes en el mercado para la simulación de dispositivos de microondas (CST Microwave Studio, HFSS,...) usan métodos numéricos genéricos como son el de elementos finitos o el de diferencias finitas (bien en el dominio del tiempo o bien en el de la frecuencia), cuya principal ventaja es que permiten atacar un amplio rango de problemas. La mayor debilidad de estos métodos genéricos es precisamente que su generalidad hace la simulación ineficiente provocando largos tiempos de computación para ciertos problemas en comparación con otras técnicas más analíticas.

Esto pone de manifiesto el primer objetivo de este trabajo, el cual consiste en desarrollar una herramienta *software* capaz de analizar, simular y diseñar antenas de bocina eficientemente basada en un método numérico, llamado Análisis Modal, del cual se sabe que es muy eficiente para operar con este tipo de problemas. Para calcular el diagrama de radiación de las antenas deberán resolverse las integrales de radiación del campo electromagnético en la apertura de la bocina. Una parte importante de este trabajo se dedicará a la obtención de las fórmulas necesarias para poder computar dichas integrales dado que la literatura no suele cubrir estos desarrollos con suficiente detalle (típicamente las integrales sólo suelen aparecer resueltas para un caso simplificado). El uso de este *software* permitirá no sólo reducir los tiempos de simulación y diseño si no también el diseñar antenas de bocina utilizando ordenadores de bajo/moderado rendimiento como los *notebook*.

La construcción de las antenas de bocina (y de nuevo, también de la mayoría de dispositivos de microondas) es un proceso de un elevado coste. Sin embargo en los últimos años las técnicas de fabricación aditiva como la impresión 3D han abierto la puerta a la manufactura de bajo coste de estructuras tridimensionales. Por lo tanto el segundo objetivo de este trabajo consiste en desarrollar un proceso de construcción para el prototipado de antenas de bocina empleando una impresora 3D. Este proceso deberá ser rápido y económico.

Para comprobar la validez de estas técnicas de fabricación se construirán distintos dispositivos como bocinas cónicas, piramidales o *choke*. Además, también se fabricarán y estudiarán guías de ondas huecas y de tipo *gap*. La fabricación de estos dispositivos se llevará a cabo localmente por el autor de este trabajo y se realizará una caracterización experimental completa de los mismos, para comparar sus características con las simulaciones realizadas utilizando los modelos desarrollados. Esto producirá una convergencia de los dos objetivos del trabajo, juntando el modelado electromagnético avanzado de dispositivos de microondas con una de las técnicas de fabricación más novedosas y modernas.

Palabras Clave

Impresora 3D, fabricación aditiva, antena, ancho de haz, guía de onda circular, corrugaciones, ganancia directiva, directividad, discontinuidad, modo evanescente, campo lejano, modo fundamental, guía de onda *gap*, matriz de dispersión generalizada, modo de orden superior, bocina, lóbulo principal, microondas, Análisis Modal, pared eléctrica perfecta, pared magnética perfecta, *PEW*, *PMW*, modo propagante, diagrama de radiación, guía de onda rectangular, matriz de dispersión, lóbulo secundario, guía de onda, modo en guía de onda

Agradecimientos

Antes de agradecer nada me gustaría disculparme.

Si estás leyendo esto es posible que hace dos años leyeses [1]. Seguramente abriste el documento y lo primero que buscaste fueron los agradecimientos (sí, todos lo hacemos. ¿Para qué ocultarlo?). Me figuro que tu sorpresa fue mayúscula al descubrir que no había ningunos. "¿Pero este tío de qué va?" te preguntarías, "¿cómo se puede ser tan arrogante?". En mi defensa debo decir que si no incluí una sección de "Agradecimientos" en mi TFG no fue porque no tuviese nada que agradecer a nadie sino porque con las prisas del momento me olvidé de hacerlo. Seré un torpe y un despistado, pero desde luego no soy un ingrato. Antes de comenzar pues pido disculpas a todas aquellas personas a las cuales haya podido ofender con este gesto. No os juzgaré si vuestra primera reacción fue coger la memoria y tirarla por la ventana.

En esta ocasión quiero hacerlo bien y no dejarme a nadie en el tintero, pero como el espacio del cual dispongo es limitado voy a aplicar un pequeño truco:

Muchas gracias a ti, lector, *seas quien seas*, por leer este trabajo. Nos esperan 50 divertidas páginas en las cuales nos deleitaremos con las maravillas del mundo de las microondas.

Bien, creo que con esto ya debería tener las espaldas cubiertas. Sin embargo, hay algunas personas a las cuales me gustaría dar las gracias incluso aunque no se lean el trabajo. Vamos pues con ello:

Por supuesto tengo que dar las gracias a Jorge, por aceptarme como su padawan hace ya unos dos años y orientarme tanto académica como profesionalmente durante este tiempo. Muchas gracias por aguantar mis infinitas preguntas y correos...

... lo cual me recuerda que también debo dar las gracias a todos los profesores que han tenido la desdicha de sufrir mis interminables preguntas durante sus clases. Muchas gracias por resolver todas mis dudas y no mandarme a paseo.

Se merecen también un agradecimiento mis compañeros del RFCAS Ana, Edu, Diego, Pablo y Paula, quienes siempre han estado dispuestos a echar una mano con cualquier cosa, resolver una duda, tomar un café o unas cañas, comentar el último capítulo de Juego de Tronos y, en defintiva, hacer cualquier cosa menos trabajar. Sin vosotros, este trabajo no habría sido ni la mitad de divertido.

No me olvido tampoco de mis compañeros de promoción que, si bien este último curso nos hemos visto menos, siempre han contribuido a crear buen rollo durante las clases y descansos, consiguiendo que estos últimos 6 años se me hayan pasado volando. Sin intención de hacerle un feo a nadie quiero agradecer especialmente su compañía y amistad a Alex, Álvaro, Antonio, Carlos, Miriam, Raquel y Víctor Hugo.

Entrando ya en el ámbito familiar (vais a tener que disculpar si me pongo aún más moñas) quiero dar las gracias a mis dos abuelas, Chari y Manolita, por haber creído siempre en mí y con ello haberme motivado a esforzarme cada día. Si este trabajo tuviese que ir dedicado a una única persona sin duda sería a ellas.

A mis padres, Luis y Marga, tengo que agradecer (entre otras muchas cosas) el que desde niño me inculcasen el gusto por el aprendizaje, la cultura y el estudio, lo cual ha contribuído en gran medida a definirme como persona. Por supuesto, también debo agradecerles que me hayan brindado la oportunidad de cursar esta carrera, subvencionándome las matrículas y pagándome un alojamiento a pensión completa en Casa Marga.

Por último, pero no por ello menos importante, quiero dar las gracias a Sofía por acompañarme durante estos últimos 4 años y darme su apoyo siempre que lo he necesitado. Muchas gracias por escuchar mis disertaciones sobre transformadas de Fourier, antenas y circuitos; muchas gracias por aguantar mis manías y rarezas; muchas gracias, en definitiva, por quererme tal y como soy, un ingeniero vocacional.

Y ahora... ¡que empiece el rock&roll!

Contents

List of Figures

List of Tables

1 Introduction

1.1 Motivation

Horn antennas are widely used in communication systems. They are, basically, a waveguide (see an example at Figure 1.1(a) on the following page) whose transverse section increases progressively along its longitudinal axis. Therefore horns (see an example at Figure 1.1(b) on the next page) share the main advantages that waveguides present. Horn antennas tend to be very robust and, since the dielectric filling them is usually air (or vacuum), these devices present small losses.

These two properties along with the high directivity gain levels achieved by horn antennas make them specially suited for aerospace applications. Horns can be used as a feed for a parabolic reflector antenna or they can be mounted on the fuselage of an airplane or spacecraft.

The main disadvantage of horns (as it happens with most waveguide devices) lies in the analysis procedures for their accurate characterization. Traditionally the approach to model waveguide devices has been based on equivalent circuits using transmission lines and lumped components. Despite these models have permitted to design many devices they also have some important limitations. The most significant is that they are only focused on modelling the fundamental response and the localized effects of higher order modes, but they do not take on account interactions between higher order modes and other complex electromagnetic effects that appear inside a waveguide. These simplifications usually lead to a mismatch between the design and the measured results.

Fortunately, the development of computers and Computer Aided Design (CAD) tools has provided engineers with the ability to perform more sophisticated simulations of these devices.

Another disadvantage of horn antennas is that the traditional construction processes usually have a high economical cost. This may not necessary be a disadvantage since it is thanks to them that horn antennas achieve some of its properties like low loss values and reliability. Anyway, the high cost associated with the fabrication can be a limitation in prototyping or teaching environments.

In the recent years, additive manufacturing techniques have become very popular thanks to

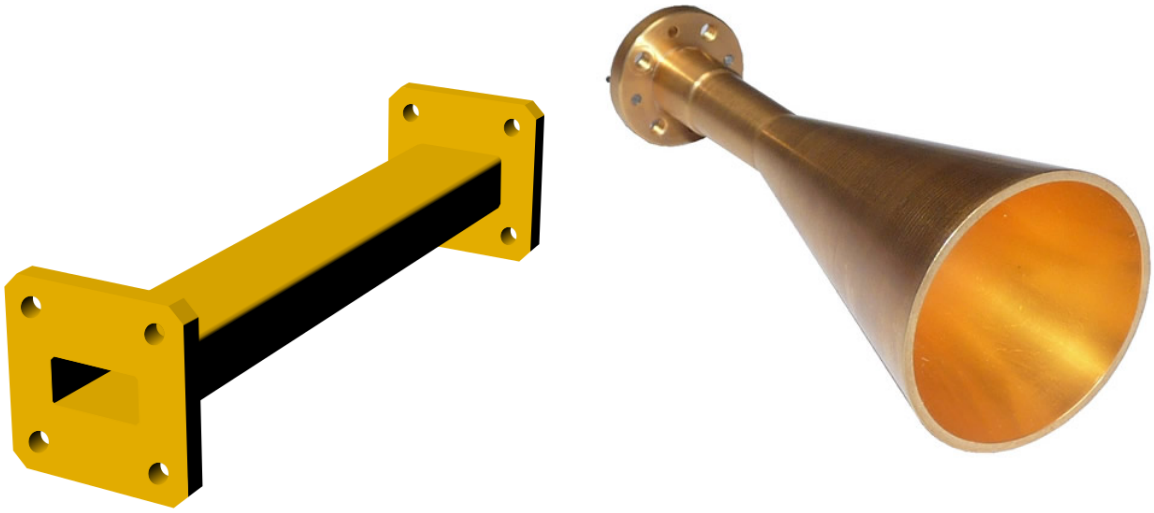

(a) Rectangular waveguide

(b) Conical horn antenna

Figure 1.1: Waveguide extracted from Wikimedia Commons (Author: Vanessa Ezekowitz). Horn antenna extracted from http://www.radiometerphysics.de .

the exponential growth of 3D printers. Since nowadays printers are relatively affordable and can achieve notable precision this work will try to use them to construct horn antennas. However, a careful study of this type of construction has to be done to asses its suitability, especially for the power losses or the sensitivity to manufacturing tolerances. This work intends to contribute in this area by developing some test examples, which are also analysed with our own developed software.

1.2 State of the Art

Nowadays the numeric methods implemented by CAD tools can be classified in two main families, general numeric techniques (like Finite Differences Method and Finite Elements Method) and quasi-analytical techniques (such as the Mode-Matching Method) [2, 3, 4]. General numeric methods are the option habitually chosen for commercial tools and they have a clear advantage over quasi-analytical methods which can tackle a wide range of problems.

Of course this generality comes at a price and the main disadvantage of general numeric methods is that they are inefficient for some particular problems, giving therefore longer computation times. On the other hand, quasi-analytical methods [2, 5, 6] are usually more efficient but they can just work with a narrow spectrum of problems.

In the recent years additive manufacturing has received an increasing interest and has even been emphasized as *the next industrial revolution* [7]. The technique chosen for the construction part of this work (3D-printing) belongs to the family of additive manufacturing processes. The key idea of these processes is to construct arbitrary 3D objects by the deposition, layer by layer, of the construction material. Additive manufacturing allows to construct complex geometries

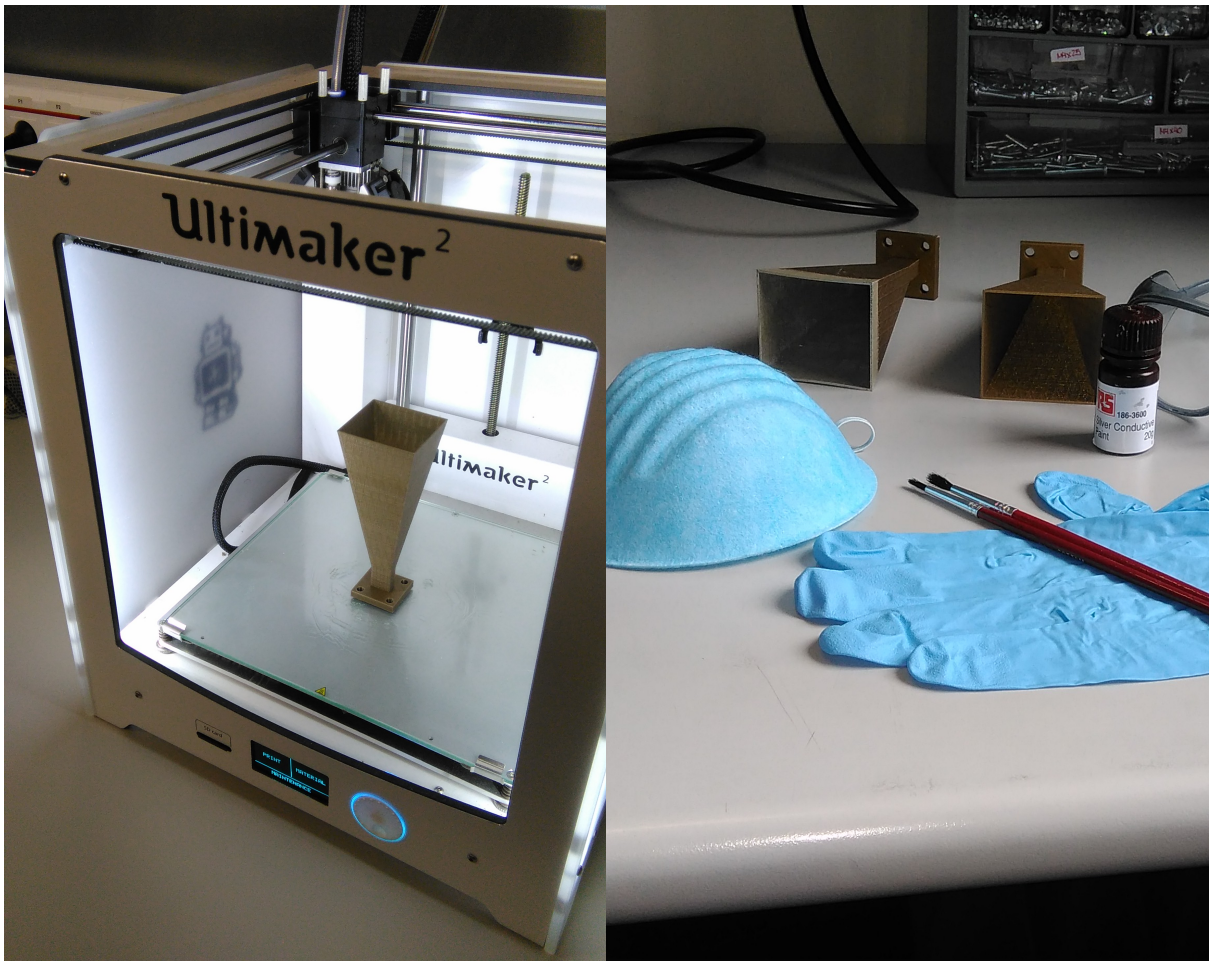

(a) 3D printer after constructing a horn antenna (b) Some of the tools used for the metallization

Figure 1.2: Photographs illustrating the manufacturing process followed in this work to construct the designed horn antennas.

that were unachievable using the traditional subtractive manufacturing (like computer numerical controlled machining).

3D-printing belongs to the additive manufacturing category known as Fused Filament Fabrication (FFF), which are characterized by the creation of a three-dimensional object by the deposition of molten plastic extruded through a nozzle. An example of a 3D-printer can be found in Figure 1.2(a). Figure 1.2(b) shows the additional elements needed to convert the model from the 3d printer in a microwave device, used in this work. Figure 1.3 shows the facilities required to test the developed components in the Escuela Politécnica Superior EPS-UAM, also used in this work.

1.3 Goals

This work has been focused on the fast and low-cost prototyping of horn antennas. To achieve this two parallel and complementary work paths have been set: one related with software (electromagnetic modelling translated into computational code) and other related with hardware

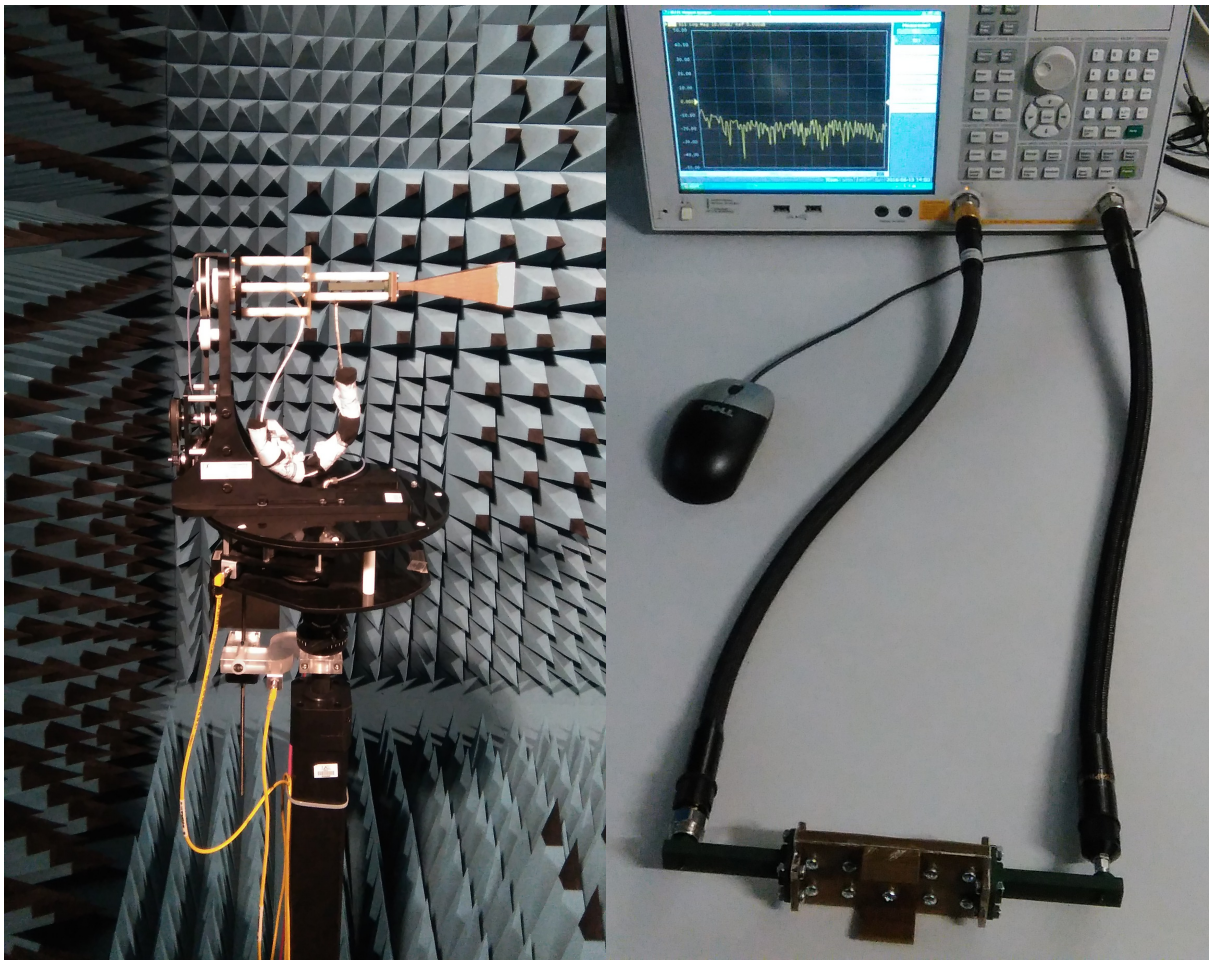

(a) Horn antenna in the anechoic chamber (b) Measurement of a hollow waveguide

Figure 1.3: Photographs illustrating the measurement process followed in this work.

(construction of the modelled devices with low-cost tools).

The software path is devoted to improve the analysis and design software for this type of antennas used in the research group where this work has been developed. This improvement will be focused on three different aspects:

1. The new software will be capable of simulating rectangular horn antennas, while refining the model of conical horns.
2. It will allow to work with any arbitrary modal electromagnetic field configuration (the original code only allowed to work with the electromagnetic fields produced when only the fundamental mode is excited at the horn input).
3. The topology of the model will be improved to achieve a better modelling of the lateral radiation. New models, which at first sight seem very sophisticated, will be developed using three-waveguide ports and hybrid perfect electric wall and perfect magnetic wall boundary conditions. Later on, these models will turn to have a simple implementation.

The hardware path will have the task of creating a process for the construction of horn antennas based on 3D printing technology. The key lines that this process must follow are:

1. It must be fast and inexpensive since it will be used as a prototyping technique. Ideally it should also be applicable to the manufacturing of other waveguide devices.
2. The behaviour of the constructed devices must agree with the simulations, and thus, careful simulations will have to be addressed using the simulation software developed in this project.
3. All the manufactured components will be experimentally characterized in the EPS-UAM, requiring to acquire the skills for performing network-analyzer measurements (calibrations, transitions,...) and anechoic chamber characterizations (positioning, measurement of different planes...)

1.4 Structure

To achieve the proposed goals the work has been divided in three different parts. Each part is covered by one or more chapters of the present document:

- **Part 1 (Theoretical fundamentals):** The first task of this work consisted in studying the electromagnetic concepts involved in the horn antenna problems. In Chapter 2 the formulations of the waveguide modes for both circular and rectangular waveguide modes are developed. The special case of perfect magnetic boundary conditions, not always treated in detail in the literature, will be shown. Chapter 3 is devoted to the radiation integrals of circular and rectangular apertures. These topics are usually just outlined (or developed for a simplified situation) in the literature, but a complete formulation suitable for programming an advanced software is not easy to find. The output of this stage was a dossier with all the developed formulas.
- **Part 2 (Horn antenna simulation):** Using the results of the previous stage a technique to efficiently simulate horn antennas has been developed. In Chapter 4 the starting point

set by [1] is presented and its limitations are highlighted. Additionally this approach is extended to support working with rectangular horns. In Chapter 5 a new and more sophisticated topology for the horn modelling technique is presented. The new topology is strongly based on the results of Chapter 2. The output of this stage was a software capable of simulating horn antennas efficiently that provides with more accurate results than the one presented in [1] and can also work with rectangular horns.

- **Part 3 (Manufacturing of horn antennas and other waveguide components):** The final stage of this work was to develop a process for low-cost horn antenna prototyping that could be implemented in a laboratory of the research group. This task has two main advantages; first, it will allow to construct and measure (locally) some of the antennas designed using the developed software, which will serve to validate the usefulness of the models created in this work; and second, the research carried out to design and implement the construction process will produce a valuable know-how that will be used in future projects since, as Chapters 6 and 7 show, these techniques can be easily extended to the construction other waveguide devices different from horn antennas (for example hollow or gap waveguides).

2

Modes of Circular and Rectangular Waveguides

2.1 Motivation

The electromagnetic field inside a waveguide can be written as a summation of modes [8, 9]. This modal series constitutes the formal solution of the Maxwell equations inside the waveguide. The decomposition of the electromagnetic field in a summation of modes is used by several techniques that characterize waveguide devices, such as the Mode-Matching used in this work.

Given the deep theoretical background of this work, this chapter shows the expressions of the waveguide modes for circular and rectangular waveguides since they constitute the basis for all the calculations that will be done. Moreover, boundary conditions not always covered in detail in the technical literature will be addressed, emphasizing the importance of a solid electromagnetic background for the development of this work.

2.2 General Considerations About Waveguide Modes

As it can be seen in Figure 2.1 a waveguide is a transmission medium composed of a dielectric (typically air) with a defined section (i.e.: rectangular, circular, elliptical...) surrounded by a perfect conductor [8, 9]. This conductor can be Perfect Electric Conductor (PEC) or Perfect Magnetic Conductor (PMC). It is well-known that magnetic conductors do not exist in nature but they can be theoretically defined as the dual case to electric conductors. As it will be seen in Chapter 5, PMC waveguides can be very useful when creating advanced models to simulate waveguide devices.

The electromagnetic field inside the waveguide can be written as a summation of modes [2], which are each of the infinite solutions for the Maxwell equations inside the waveguide.

From Maxwell's curl equations:

$$\nabla \times \vec{\mathbf{E}} = -j\omega\mu\vec{\mathbf{H}}, \tag{2.1}$$

$$\nabla \times \vec{\mathbf{H}} = j\omega\epsilon\vec{\mathbf{E}}, \tag{2.2}$$

applying vector calculus the following equations, known as the Helmholtz equations [8] for $\vec{\mathbf{E}}$ and $\vec{\mathbf{H}}$, can be obtained:

$$\nabla^2\vec{\mathbf{E}} + \omega^2\mu\epsilon\vec{\mathbf{E}} = 0, \tag{2.3}$$

$$\nabla^2\vec{\mathbf{H}} + \omega^2\mu\epsilon\vec{\mathbf{H}} = 0. \tag{2.4}$$

By solving this equations the modal fields of the waves propagating inside the waveguide can be obtained [8]. The derivation of the Transverse Electric (TE) and Transverse Magnetic (TM) modes is well known and can be found in the literature [8], therefore it will not be presented in this chapter. The longitudinal electric or magnetic field inside a waveguide (depending on the type of mode) can be computed by solving

$$\nabla_t^2 F_{E,H} + k_c^2 F_{E,H} = 0, \tag{2.5}$$

where $\binom{E_z}{H_z} = F_{E,H}e^{-\gamma z}$ and $\gamma = \sqrt{k_c^2 + \gamma_0^2} = \sqrt{k_c^2 - \omega^2\mu\epsilon}$, applying the appropriate boundary conditions imposed by the surrounding conductor.

In a PEC waveguide the electric field must satisfy that:

$$\hat{\mathbf{n}} \times \vec{\mathbf{E}}\rfloor_{C_\sigma} = \mathbf{0} \tag{2.6}$$

and therefore:

$$\left.\frac{\partial F_H}{\partial n}\right\rfloor_{C_\sigma} = 0 \tag{2.7}$$

for TE modes and:

$$F_E\rfloor_{C_\sigma} = 0 \tag{2.8}$$

for TM modes. C_σ is the metallic boundary of the waveguide (the contour surrounding the surface S of the waveguide filled by dielectric), the perfect electric conductor in the theoretical analysis.

In a PMC waveguide the magnetic field must satisfy that:

$$\hat{\mathbf{n}} \times \vec{\mathbf{H}}\rfloor_{C_\mu} = \mathbf{0} \tag{2.9}$$

and therefore:

$$F_H\rfloor_{C_\mu} = 0 \tag{2.10}$$

for TE modes and:

$$\left.\frac{\partial F_E}{\partial n}\right\rfloor_{C_\mu} = 0 \tag{2.11}$$

for TM modes. C_μ is the contour of the waveguide assuming perfect magnetic conductor.

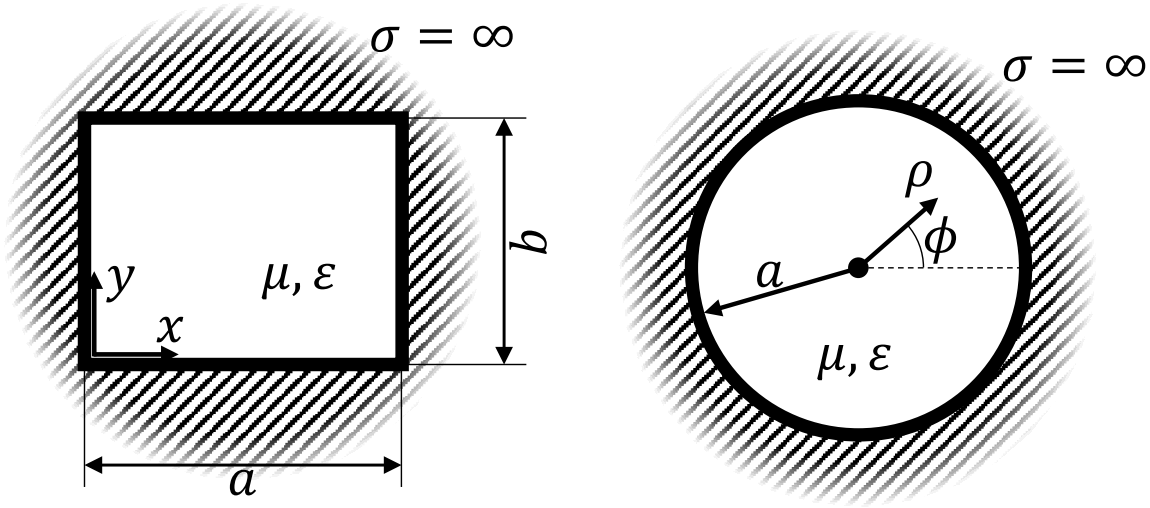

(a) Rectangular waveguide

(b) Circular waveguide

Figure 2.1: Section of different waveguides used in microwave systems, with their main parameters. The bounding perfect conductor can be either electric or magnetic. The inner part is filled by dielectric of dielectric permittivity ϵ and magnetic permeability μ.

In the following sections the Helmholtz equation will be solved for a rectangular and a circular waveguide, using both PEC and PMC boundary conditions. It is important to note that the formulation with PMC is not usually found in the common literature. On the other hand the formulation for a PEC waveguide can be found in [8] but it will be presented in this chapter in order to establish a coherent notation for both PEC and PMC cases, since the modal expressions will be used in Chapter 3 intensively.

2.3 Rectangular Waveguides with PEC and PMC Boundary Conditions

It is known that the solution of the Helmholtz equation for the problem in Figure 2.1(a) is

$$F(x,y) = (A\sin(k_x x) + B\cos(k_x x x))(C\sin(k_y y) + D\cos(k_y y)), \tag{2.12}$$

where $k_c^2 = k_x^2 + k_y^2$ and constants A, B, C, D, k_x, k_y would be defined depending on the boundary conditions imposed by the conductor [8].

2.3.1 Perfect Electric Conductor Waveguides

TE Modes

The condition of (2.7) is imposed on each of the four walls to obtain the values of A, C, k_x, k_y:

$$\left.\frac{\partial F_H}{\partial y}\right\rfloor_{\binom{y=0}{0\le x\le a}} = 0 \Rightarrow C = 0 \tag{2.13}$$

$$\left.\frac{\partial F_H}{\partial y}\right\rfloor_{\binom{y=b}{0\le x\le a}} = 0 \Rightarrow k_y = \frac{n\pi}{b}, \forall n \in \mathbb{N} \tag{2.14}$$

$$\left.\frac{\partial F_H}{\partial x}\right\rfloor_{\binom{x=0}{0\le y\le b}} = 0 \Rightarrow A = 0 \tag{2.15}$$

$$\left.\frac{\partial F_H}{\partial x}\right\rfloor_{\binom{x=a}{0\le y\le b}} = 0 \Rightarrow k_x = \frac{m\pi}{a}, \forall m \in \mathbb{N} \tag{2.16}$$

which gives the following value for the longitudinal component of the magnetic field:

$$H_z = F_H e^{-\gamma z} = P\cos(\frac{m\pi x}{a})\cos(\frac{n\pi y}{b})e^{-\gamma z} \tag{2.17}$$

and applying the traverse gradient, the rest of the components are computed.

$$\vec{\mathbf{H}}_t = \frac{-\gamma}{k_c^2}\nabla_t H_z \Rightarrow \begin{cases} H_x = \frac{\gamma k_x}{k_c^2}\sin(k_x x)\cos(k_y y)e^{-\gamma z} \\ H_y = \frac{\gamma k_y}{k_c^2}\cos(k_x x)\sin(k_y y)e^{-\gamma z} \end{cases} \tag{2.18}$$

Finally, the electric field can be obtained from the magnetic field since they are related by the modal impedance:

$$\vec{\mathbf{E}}_t = Z_{TE}(\vec{\mathbf{H}}_t \times \hat{\mathbf{z}}) \Rightarrow \begin{cases} E_x = \frac{j\omega\mu k_y}{k_c^2}\cos(k_x x)\sin(k_y y)e^{-\gamma z} \\ E_y = \frac{-j\omega\mu k_x}{k_c^2}\sin(k_x x)\cos(k_y y)e^{-\gamma z} \end{cases} \tag{2.19}$$

TM Modes

The condition of (2.8) is imposed on each of the four walls to obtain the values of B, D, k_x, k_y:

$$F_E\rfloor_{\binom{y=0}{0\le x\le a}} = 0 \Rightarrow D = 0 \tag{2.20}$$

$$F_E\rfloor_{\binom{y=b}{0\le x\le a}} = 0 \Rightarrow k_y = \frac{n\pi}{b}, \forall n \in \mathbb{N} \tag{2.21}$$

$$F_E\rfloor_{\binom{x=0}{0\le y\le b}} = 0 \Rightarrow B = 0 \tag{2.22}$$

$$F_E\rfloor_{\binom{x=a}{0\le y\le b}} = 0 \Rightarrow k_x = \frac{m\pi}{a}, \forall m \in \mathbb{N} \tag{2.23}$$

Which gives the following value for the longitudinal component of the electric field:

$$E_z = F_E e^{-\gamma z} = Q\sin(\frac{m\pi x}{a})\sin(\frac{n\pi y}{b})e^{-\gamma z} \tag{2.24}$$

and applying the traverse gradient, the rest of the components are computed.

$$\vec{\mathbf{E}}_t = \frac{-\gamma}{k_c^2}\nabla_t E_z \Rightarrow \begin{cases} E_x = \frac{-\gamma k_x}{k_c^2}\cos(k_x x)\sin(k_y y)e^{-\gamma z} \\ E_y = \frac{-\gamma k_y}{k_c^2}\sin(k_x x)\cos(k_y y)e^{-\gamma z} \end{cases} \tag{2.25}$$

Finally, the magnetic field can be obtained from the electric field since they are related by the modal impedance:

$$\vec{\mathbf{H}}_t = \frac{1}{Z_{TM}}(\hat{\mathbf{z}} \times \vec{\mathbf{E}}_t) \Rightarrow \begin{cases} H_x = \frac{j\omega\epsilon k_y}{k_c^2}\sin(k_x x)\cos(k_y y)e^{-\gamma z} \\ H_y = \frac{-j\omega\epsilon k_x}{k_c^2}\cos(k_x x)\sin(k_y y)e^{-\gamma z} \end{cases} \tag{2.26}$$

2.3.2 Perfect Magnetic Conductor Waveguides

TE Modes

The condition of (2.10) is imposed on each of the four walls to obtain the values of D, B, k_x, k_y:

$$F_H\big\rfloor_{\left(\substack{y=0 \\ 0\le x\le a}\right)} = 0 \Rightarrow D = 0 \tag{2.27}$$

$$F_H\big\rfloor_{\left(\substack{y=b \\ 0\le x\le a}\right)} = 0 \Rightarrow k_y = \frac{n\pi}{b}, \forall n \in \mathbb{N} \tag{2.28}$$

$$F_H\big\rfloor_{\left(\substack{x=0 \\ 0\le y\le b}\right)} = 0 \Rightarrow B = 0 \tag{2.29}$$

$$F_H\big\rfloor_{\left(\substack{x=a \\ 0\le y\le b}\right)} = 0 \Rightarrow k_x = \frac{m\pi}{a}, \forall m \in \mathbb{N} \tag{2.30}$$

Which gives the following value for the longitudinal component of the magnetic field:

$$H_z = F_H e^{-\gamma z} = P\sin(\frac{m\pi x}{a})\sin(\frac{n\pi y}{b})e^{-\gamma z} \tag{2.31}$$

and applying the traverse gradient, the rest of the components are computed.

$$\vec{\mathbf{H}}_t = \frac{-\gamma}{k_c^2}\nabla_t H_z \Rightarrow \begin{cases} H_x = \frac{-\gamma k_x}{k_c^2}\cos(k_x x)\sin(k_y y)e^{-\gamma z} \\ H_y = \frac{-\gamma k_y}{k_c^2}\sin(k_x x)\cos(k_y y)e^{-\gamma z} \end{cases} \tag{2.32}$$

Finally, the electric field can be obtained from the magnetic field since they are related by the modal impedance:

$$\vec{\mathbf{E}}_t = Z_{TE}(\vec{\mathbf{H}}_t \times \hat{\mathbf{z}}) \Rightarrow \begin{cases} E_x = \frac{-j\omega\mu k_y}{k_c^2}\sin(k_x x)\cos(k_y y)e^{-\gamma z} \\ E_y = \frac{j\omega\mu k_x}{k_c^2}\cos(k_x x)\sin(k_y y)e^{-\gamma z} \end{cases} \tag{2.33}$$

TM Modes

The condition of (2.11) is imposed on each of the four walls to obtain the values of A, C, k_x, k_y:

$$\left.\frac{\partial F_E}{\partial y}\right]_{\binom{y=0}{0\le x\le a}} = 0 \Rightarrow C = 0 \tag{2.34}$$

$$\left.\frac{\partial F_E}{\partial y}\right]_{\binom{y=b}{0\le x\le a}} = 0 \Rightarrow k_y = \frac{n\pi}{b}, \forall n \in \mathbb{N} \tag{2.35}$$

$$\left.\frac{\partial F_E}{\partial x}\right]_{\binom{x=0}{0\le y\le b}} = 0 \Rightarrow A = 0 \tag{2.36}$$

$$\left.\frac{\partial F_E}{\partial x}\right]_{\binom{x=a}{0\le y\le b}} = 0 \Rightarrow k_x = \frac{m\pi}{a}, \forall m \in \mathbb{N} \tag{2.37}$$

Which gives the following value for the longitudinal component of the electric field:

$$E_z = F_E e^{-\gamma z} = Q\cos(\frac{m\pi x}{a})\cos(\frac{n\pi y}{b})e^{-\gamma z} \tag{2.38}$$

and applying the traverse gradient, the rest of the components are computed.

$$\vec{\mathbf{E}}_t = \frac{-\gamma}{k_c^2}\nabla_t E_z \Rightarrow \begin{cases} E_x = \frac{\gamma k_x}{k_c^2}\sin(k_x x)\cos(k_y y)e^{-\gamma z} \\ E_y = \frac{\gamma k_y}{k_c^2}\cos(k_x x)\sin(k_y y)e^{-\gamma z} \end{cases} \tag{2.39}$$

Finally, the magnetic field can be obtained from the electric field since they are related by the modal impedance:

$$\vec{\mathbf{H}}_t = \frac{1}{Z_{TM}}(\hat{\mathbf{z}} \times \vec{\mathbf{E}}_t) \Rightarrow \begin{cases} H_x = \frac{-j\omega\epsilon k_y}{k_c^2}\cos(k_x x)\sin(k_y y)e^{-\gamma z} \\ H_y = \frac{j\omega\epsilon k_x}{k_c^2}\sin(k_x x)\cos(k_y y)e^{-\gamma z} \end{cases} \tag{2.40}$$

for the TM modes.

2.4 Circular Waveguides with PEC and PMC Boundary Conditions

The modes of a circular waveguide as that in Figure 2.1(b) are well known and have a closed analytical formula that can be found in the literature, like [8]:

$$E_\rho = \frac{-j\omega\mu n}{k_c^2\rho}C_n(k_c\rho)\begin{pmatrix}-\sin(n\phi)\\ \cos(n\phi)\end{pmatrix}e^{-\gamma z} \tag{2.41}$$

$$E_\phi = \frac{j\omega\mu}{k_c}C_n'(k_c\rho)\begin{pmatrix}\cos(n\phi)\\ \sin(n\phi)\end{pmatrix}e^{-\gamma z} \tag{2.42}$$

$$H_\rho = \frac{-\gamma}{k_c}C_n'(k_c\rho)\begin{pmatrix}\cos(n\phi)\\ \sin(n\phi)\end{pmatrix}e^{-\gamma z} \tag{2.43}$$

$$H_\phi = \frac{-\gamma n}{k_c^2\rho}C_n(k_c\rho)\begin{pmatrix}-\sin(n\phi)\\ \cos(n\phi)\end{pmatrix}e^{-\gamma z} \tag{2.44}$$

$$H_z = C_n(k_c\rho)\begin{pmatrix}\cos(n\phi)\\ \sin(n\phi)\end{pmatrix}e^{-\gamma z}, \tag{2.45}$$

for the TE modes and

$$E_\rho = \frac{-\gamma}{k_c}C_n'(k_c\rho)\begin{pmatrix}\cos(n\phi)\\ \sin(n\phi)\end{pmatrix}e^{-\gamma z} \tag{2.46}$$

$$E_\phi = \frac{-\gamma n}{k_c^2\rho'}C_n(k_c\rho)\begin{pmatrix}-\sin(n\phi)\\ \cos(n\phi)\end{pmatrix}e^{-\gamma z} \tag{2.47}$$

$$E_z = C_n(k_c\rho)\begin{pmatrix}\cos(n\phi)\\ \sin(n\phi)\end{pmatrix}e^{-\gamma z} \tag{2.48}$$

$$H_\rho = \frac{j\omega\epsilon n}{k_c^2\rho}C_n(k_c\rho)\begin{pmatrix}-\sin(n\phi)\\ \cos(n\phi)\end{pmatrix}e^{-\gamma z} \tag{2.49}$$

$$H_\phi = \frac{-j\omega\epsilon}{k_c}C_n'(k_c\rho)\begin{pmatrix}\cos(n\phi)\\ \sin(n\phi)\end{pmatrix}e^{-\gamma z}, \tag{2.50}$$

for the TM modes, where $\gamma = \sqrt{k_c^2+\gamma_0^2}$, $C_n(u) = AJ_n(u) + BY_n(u)$ and k_c are the wave numbers of each mode, which are determined by the contour conditions of the problem and depend on the type of conductor used to create the waveguide.

It is interesting to note that the electromagnetic field must be finite at all the non-singular space points and therefore B must be zero since $Y_n(u) \to -\infty$, when $u \to 0$. So $C_n(u) = AJ_n(u)$. However, the expressions have been written in this way with a general $C_n(u)$ to emphasize the similarities with a coaxial waveguide, where both A and B are non-zero and are related by the boundary conditions [8].

Now the generic equations presented above will be particularized for the case of a PEC and PMC waveguide, taking on account the different boundary conditions that each conductor impose to the electromagnetic field.

2.4.1 Perfect Electric Conductor Waveguides

In a Perfect Electric Conductor (PEC) waveguide the wave numbers are calculated as:

$$F_H = C_n(k_c\rho)\begin{pmatrix}\cos(n\phi)\\ \sin(n\phi)\end{pmatrix}, \left.\frac{\partial F_H}{\partial\rho}\right\rfloor_{\substack{\rho=a\\ 0\le\phi\le 2\pi}} = 0 \Rightarrow \tag{2.51}$$

$$k_c C_n'(k_c a)\begin{pmatrix}\cos(n\phi)\\ \sin(n\phi)\end{pmatrix} = 0, \forall\phi \Rightarrow C_n'(k_c a) = 0 \Rightarrow k_c a = p'_{mn}, \tag{2.52}$$

for TE modes, where p'_{mn} are the zeros of the derivative of the Bessel function [9], and

$$F_E = C_n(k_c\rho)\begin{pmatrix}\cos(n\phi)\\ \sin(n\phi)\end{pmatrix}, F_E\rfloor_{\substack{\rho=a\\ 0\le\phi\le 2\pi}} = 0 \Rightarrow \tag{2.53}$$

$$k_c C_n(k_c a)\begin{pmatrix}\cos(n\phi)\\ \sin(n\phi)\end{pmatrix} = 0, \forall\phi \Rightarrow C_n(k_c a) = 0 \Rightarrow k_c a = p_{mn}, \tag{2.54}$$

for the TM modes, where p_{mn} are the zeros of the Bessel function [9]. F_H and F_E represent the longitudinal components of the magnetic and electric fields respectively.

2.4.2 Perfect Magnetic Conductor Waveguides

In a Perfect Magnetic Conductor (PMC) waveguide the wave numbers are calculated as:

$$F_H = C_n(k_c\rho)\begin{pmatrix}\cos(n\phi)\\ \sin(n\phi)\end{pmatrix}, F_H\rfloor_{\left(\substack{\rho=a\\ 0\leq\phi\leq 2\pi}\right)} = 0 \Rightarrow \tag{2.55}$$

$$k_c C_n(k_c a)\begin{pmatrix}\cos(n\phi)\\ \sin(n\phi)\end{pmatrix} = 0, \forall\phi \Rightarrow C_n(k_c a) = 0 \Rightarrow k_c a = p_{mn}, \tag{2.56}$$

for TE modes and

$$F_E = C_n(k_c\rho)\begin{pmatrix}\cos(n\phi)\\ \sin(n\phi)\end{pmatrix}, \left.\frac{\partial F_E}{\partial\rho}\right\rfloor_{\left(\substack{\rho=a\\ 0\leq\phi\leq 2\pi}\right)} = 0 \Rightarrow \tag{2.57}$$

$$k_c C_n'(k_c a)\begin{pmatrix}\cos(n\phi)\\ \sin(n\phi)\end{pmatrix} = 0, \forall\phi \Rightarrow C_n'(k_c a) = 0 \Rightarrow k_c a = p_{mn}', \tag{2.58}$$

for the TM modes. Where F_H and F_E represent the longitudinal components of the magnetic and electric fields respectively [8].

2.5 Conclusions

In this chapter the formulation of the modes for both a circular and rectangular waveguide, made either of PEC and PMC walls, has been presented. These modes constitute the basis of the numerical method that will be employed in this work, the Mode-Matching.

Additionally, in the spite that PMC does not have a direct material equivalent in nature the concept of a PMC waveguide can be exploited in simulation to model certain boundary conditions, as it will be shown in Chapter 5. This case is not treated in detail in the technical literature and has been addressed here for the sake of the clarity, showing the duality with the PEC case.

3

Radiation Integrals of Open Waveguides

3.1 Motivation

When using the Mode-Matching approach presented later in this work to simulate a horn antenna, the radiation patter is obtained computing the radiation integral of the electromagnetic field at the horn aperture.

In [1] a simplified version of this integral for circular apertures was presented. Despite being a correct solution it was not a complete solution for more general cases. As it is known the electromagnetic field inside a waveguide can be written as a summation of modes [2, 8] and therefore a complete solution must consider each one of the infinite possible modes. The integrations presented in [1] only considered the subset of modes that appear inside the horn when only the fundamental mode is excited at its input.

When dealing with complex problems or designs this result may render insufficient. For example, when designing an OMT (Orthomode Transducer) [10] undesired high order modes might be excited at its output and the microwave engineer may want to know how they will affect to the radiation pattern of the antenna mounted after the OMT.

In this chapter the radiation integrals for both circular and rectangular apertures will be developed for any waveguide mode configuration. This part has been fully developed in this work since it is crucial for the analysis models shown later and the technical literature only provides intermediate results, used here for obtaining the complete formulation.

Another limitation of the radiation model employed in [1] is the use of the equivalence principle known as "Equivalent principle of great apertures" [11], which simplifies the development of an analytical formula but provides with worse results when the antenna does not have a great directivity value. The integrations developed in this chapter will not use this approximation.

Since there is a lot of algebra involved in this calculations only the main steps will be outlined in this chapter. The complete calculation can be found in Appendices A and B. This is an important derivation because it has been necessary for the development of the simulation software, since the expressions are not detailed in the literature.

3.2 Equivalence Principles

To calculate the field radiated by an antenna the magnetic and electric vector potentials ($\vec{\mathbf{A}}$ and $\vec{\mathbf{F}}$, respectively) must be used. These potentials are typically computed based on electric and magnetic currents. Since there are no surface currents over an aperture, the equivalence principle allows to define "equivalent" magnetic and electric currents based on the electric and magnetic fields at the aperture [4].

By introducing PEC or PMC boundary conditions in the plane of the aperture different formulations can be developed [11]. The "first principle" does not include any of this boundaries and therefore both electric and magnetic currents have to be considered. The "second principle" introduces a PEC boundary condition at the aperture plane and applies the image theory to cancel out the electric current. The "third principle" consists on the dual situation, where a PMC boundary is introduced to cancel the magnetic current.

Using the second and third principles the computation of the radiation pattern can be simplified since they allow to avoid the calculation of one of the vector potentials. Nevertheless, in this work they will be of reduced use since, as it is shown in (3.11), thanks to the well defined formulation of the rectangular and circular waveguide modes the integration associated to the electric vector potential can be computed from the integration associated to the magnetic vector potential and vice versa.

The expressions to compute the farfield radiation pattern using each of the mentioned principles are as follows:

$$\begin{cases} E_\theta(r,\theta,\phi) = j\dfrac{k_0}{4\pi}\dfrac{e^{-jk_0r}}{r}\left(P_x\cos\phi + P_y\sin\phi - \eta_0\cos\theta\left(Q_x\sin\phi - Q_y\cos\phi\right)\right) & (3.1) \\ E_\phi(r,\theta,\phi) = -j\dfrac{k_0}{4\pi}\dfrac{e^{-jk_0r}}{r}\left(\cos\theta\left(P_x\sin\phi - P_y\cos\phi\right) + \eta_0\left(Q_x\cos\phi + Q_y\sin\phi\right)\right) & (3.2) \end{cases}$$

$$\begin{cases} E_\theta(r,\theta,\phi) = j\dfrac{k_0}{2\pi}\dfrac{e^{-jk_0r}}{r}\left(P_x\cos\phi + P_y\sin\phi\right) & (3.3) \\ E_\phi(r,\theta,\phi) = -j\dfrac{k_0}{2\pi}\dfrac{e^{-jk_0r}}{r}\left(\cos\theta\left(P_x\sin\phi - P_y\cos\phi\right)\right) & (3.4) \end{cases}$$

$$\begin{cases} E_\theta(r,\theta,\phi) = -j\dfrac{k_0\eta_0}{2\pi}\dfrac{e^{-jk_0r}}{r}\left(\cos\theta\left(Q_x\sin\phi - Q_y\cos\phi\right)\right) & (3.5) \\ E_\phi(r,\theta,\phi) = -j\dfrac{k_0\eta_0}{2\pi}\dfrac{e^{-jk_0r}}{r}\left(Q_x\cos\phi + Q_y\sin\phi\right) & (3.6) \end{cases}$$

where P_x, P_y and Q_x, Q_y represent the two-dimensional Fourier transform of the electric and magnetic fields at the aperture [11] (the x and y subscripts point out that the Fourier transform is computed only for the x or y component of the field):

$$P_x = \iint_{S_a} E_{ax}(x',y')e^{jk_0(x'\sin(\theta)\cos(\phi)+y'\sin(\theta)\sin(\phi))}dx'dy' \quad (3.7)$$

$$P_y = \iint_{S_a} E_{ay}(x',y')e^{jk_0(x'\sin(\theta)\cos(\phi)+y'\sin(\theta)\sin(\phi))}dx'dy' \quad (3.8)$$

$$Q_x = \iint_{S_a} H_{ax}(x',y')e^{jk_0(x'\sin(\theta)\cos(\phi)+y'\sin(\theta)\sin(\phi))}dx'dy' \quad (3.9)$$

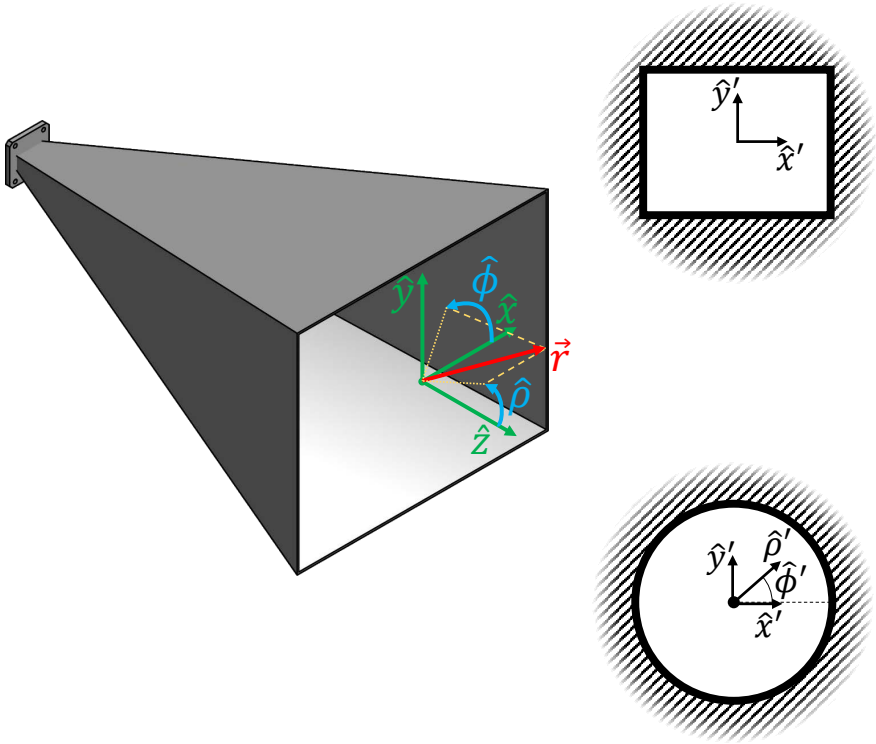

Figure 3.1: Representation of the different coordinate systems used to compute the radiation integrals. On the left, spherical coordinates used to represent the radiation pattern; on the right, local coordinate system used to write the electromagnetic field at the horn aperture in two different apertures S_a (rectangular and circular).

$$Q_y = \iint_{S_a} H_{ay}(x', y') e^{jk_0(x' \sin(\theta)\cos(\phi) + y' \sin(\theta)\sin(\phi))} dx' dy' \tag{3.10}$$

and therefore they are related by the modal impedance:

$$Q_{x,TE} = -\frac{P_{y,TE}}{Z_{TE}}, Q_{y,TE} = \frac{P_{x,TE}}{Z_{TE}}, Q_{x,TM} = -\frac{P_{y,TM}}{Z_{TM}}, Q_{y,TM} = \frac{P_{x,TM}}{Z_{TM}} \tag{3.11}$$

where $k_0 = \omega\sqrt{\mu\epsilon}$.

It is important to note that each principle may give better results for different problems and, therefore, all of them have been implemented.

3.3 Rectangular Apertures

3.3.1 Electric Field at the Aperture

The expressions for the TE and TM modes of a rectangular waveguide have been developed in Chapter 2:

$$E_{x'} = \frac{j\omega\mu n\pi}{k_c^2 b}\cos\left(\frac{m\pi x'}{a}+\frac{m\pi}{2}\right)\sin\left(\frac{n\pi y'}{b}+\frac{n\pi}{2}\right) \tag{3.12}$$

$$E_{y'} = \frac{j\omega\mu m\pi}{k_c^2 a}\sin\left(\frac{m\pi x'}{a}+\frac{m\pi}{2}\right)\cos\left(\frac{n\pi y'}{b}+\frac{n\pi}{2}\right), \tag{3.13}$$

for the TE modes and

$$E_{x'} = \frac{-\gamma m\pi}{k_c^2 a}\cos\left(\frac{m\pi x'}{a}+\frac{m\pi}{2}\right)\sin\left(\frac{n\pi y'}{b}+\frac{n\pi}{2}\right) \tag{3.14}$$

$$E_{y'} = \frac{\gamma n\pi}{k_c^2 b}\sin\left(\frac{m\pi x'}{a}+\frac{m\pi}{2}\right)\cos\left(\frac{n\pi y'}{b}+\frac{n\pi}{2}\right) \tag{3.15}$$

for the TM modes (Note that the z component is not relevant for this problem). It is important to mention that in this case the coordinate origin has been translated from the corner of the waveguide to its centre (terms $\frac{n\pi}{2}$ and $\frac{m\pi}{2}$ in the arguments of the sinusoids. This has been done to simplify the following integrations.

3.3.2 Integration of the Field at the Aperture

The components of the electric field presented on the previous section are used to compute the values P_x and P_y described in Section 3.2.

To tackle this task the following integrations will prove useful:

$$s(k_1,k_2,k_3,\tau) = \int \sin(k_1\tau+k_3)e^{jk_2\tau}d\tau = \tag{3.16}$$

$$= -\frac{k_1 e^{jk_2\tau}\cos(k_3+\tau k_1) - jk_2 e^{jk_2\tau}\sin(k_3+\tau k_1)}{k_1^2-k_2^2}, \tag{3.17}$$

$$c(k_1,k_2,k_3,\tau) = \int \cos(k_1\tau+k_3)e^{jk_2\tau}d\tau = \tag{3.18}$$

$$= \frac{k_1 e^{jk_2\tau}\sin(k_3+\tau k_1) + jk_2 e^{jk_2\tau}\cos(k_3+\tau k_1)}{k_1^2-k_2^2}. \tag{3.19}$$

The procedure starts with the TE modes, inserting (3.12) and (3.13) in (3.7) and (3.8) respectively:

$$P_{x,TE} = \int_{y'=-b/2}^{b/2}\int_{x'=-a/2}^{a/2} E_{ap,x}e^{jk(x'\sin(\theta)\cos(\phi)+y'\sin(\theta)\sin(\phi))}dx'dy' = \tag{3.20}$$

$$= \frac{j\omega\mu n\pi}{k_c^2 b}\left\{\left[s\left(\frac{n\pi}{b},k\sin(\theta)\sin(\phi),\frac{n\pi}{2},\frac{b}{2}\right) - s\left(\frac{n\pi}{b},k\sin(\theta)\sin(\phi),\frac{n\pi}{2},\frac{-b}{2}\right)\right]\right. \tag{3.21}$$

$$\left.\cdot\left[c\left(\frac{m\pi}{a},k\sin(\theta)\cos(\phi),\frac{m\pi}{2},\frac{a}{2}\right) - c\left(\frac{m\pi}{a},k\sin(\theta)\cos(\phi),\frac{m\pi}{2},\frac{-a}{2}\right)\right]\right\}, \tag{3.22}$$

and

$$P_{y,TE} = \int_{y'=-b/2}^{b/2}\int_{x'=-a/2}^{a/2} E_{ap,y} e^{jk(x'\sin(\theta)\cos(\phi)+y'\sin(\theta)\sin(\phi))}dx'dy' = \tag{3.23}$$

$$= \frac{j\omega\mu m\pi}{k_c^2 a}\left\{\left[c\left(\frac{n\pi}{b}, k\sin(\theta)\sin(\phi), \frac{n\pi}{2}, \frac{b}{2}\right) - c\left(\frac{n\pi}{b}, k\sin(\theta)\sin(\phi), \frac{n\pi}{2}, \frac{-b}{2}\right)\right]\right. \tag{3.24}$$

$$\left.\cdot\left[s\left(\frac{m\pi}{a}, k\sin(\theta)\cos(\phi), \frac{m\pi}{2}, \frac{a}{2}\right) - s\left(\frac{m\pi}{a}, k\sin(\theta)\cos(\phi), \frac{m\pi}{2}, \frac{-a}{2}\right)\right]\right\}. \tag{3.25}$$

Operating similarly for the TM Modes:

$$P_{x,TM} = \int_{y'=-b/2}^{b/2}\int_{x'=-a/2}^{a/2} E_{ap,x} e^{jk(x'\sin(\theta)\cos(\phi)+y'\sin(\theta)\sin(\phi))}dx'dy' = \tag{3.26}$$

$$= \frac{-\gamma m\pi}{k_c^2 a}\left\{\left[s\left(\frac{n\pi}{b}, k\sin(\theta)\sin(\phi), \frac{n\pi}{2}, \frac{b}{2}\right) - s\left(\frac{n\pi}{b}, k\sin(\theta)\sin(\phi), \frac{n\pi}{2}, \frac{-b}{2}\right)\right]\right. \tag{3.27}$$

$$\left.\cdot\left[c\left(\frac{m\pi}{a}, k\sin(\theta)\cos(\phi), \frac{m\pi}{2}, \frac{a}{2}\right) - c\left(\frac{m\pi}{a}, k\sin(\theta)\cos(\phi), \frac{m\pi}{2}, \frac{-a}{2}\right)\right]\right\}, \tag{3.28}$$

and

$$P_{y,TM} = \int_{y'=-b/2}^{b/2}\int_{x'=-a/2}^{a/2} E_{ap,y} e^{jk(x'\sin(\theta)\cos(\phi)+y'\sin(\theta)\sin(\phi))}dx'dy' = \tag{3.29}$$

$$= \frac{\gamma n\pi}{k_c^2 b}\left\{\left[c\left(\frac{n\pi}{b}, k\sin(\theta)\sin(\phi), \frac{n\pi}{2}, \frac{b}{2}\right) - c\left(\frac{n\pi}{b}, k\sin(\theta)\sin(\phi), \frac{n\pi}{2}, \frac{-b}{2}\right)\right]\right. \tag{3.30}$$

$$\left.\cdot\left[s\left(\frac{m\pi}{a}, k\sin(\theta)\cos(\phi), \frac{m\pi}{2}, \frac{a}{2}\right) - s\left(\frac{m\pi}{a}, k\sin(\theta)\cos(\phi), \frac{m\pi}{2}, \frac{-a}{2}\right)\right]\right\}. \tag{3.31}$$

Q_x and Q_y can be obtained using the relations in (3.11) without the need to compute any new integrations.

3.4 Circular Apertures

3.4.1 Electric Field at the Aperture

The expressions for the TE and TM modes of a circular waveguide have been developed in Chapter 2. The components needed now for TE modes are:

$$E_{\rho'} = \frac{-j\omega\mu n}{k_c^2\rho'} C_n(k_c\rho')\begin{pmatrix}-\sin(n\phi')\\ \cos(n\phi')\end{pmatrix} \tag{3.32}$$

$$E_{\phi'} = \frac{j\omega\mu}{k_c} C_n'(k_c\rho')\begin{pmatrix}\cos(n\phi')\\ \sin(n\phi')\end{pmatrix}. \tag{3.33}$$

The components needed for TM modes are

$$E_{\rho'} = \frac{-\gamma}{k_c} C_n'(k_c\rho') \begin{pmatrix} \cos(n\phi') \\ \sin(n\phi') \end{pmatrix} \tag{3.34}$$

$$E_{\phi'} = \frac{-\gamma n}{k_c^2 \rho'} C_n(k_c\rho') \begin{pmatrix} -\sin(n\phi') \\ \cos(n\phi') \end{pmatrix}. \tag{3.35}$$

3.4.2 Vectors in Rectangular Coordinates

The formulas for the different equivalence principles are developed for an electromagnetic field written with vectors in a rectangular coordinates system, but the expressions of the modes presented above are written with vectors in a cylindrical coordinates system. To juggle both formulations the previous expressions have to be written on a rectangular coordinates system using the following transformation:

$$\begin{cases} \hat{\rho}' = \cos(\phi')\hat{\mathbf{x}}' + \sin(\phi')\hat{\mathbf{y}}' & (3.36) \\ \hat{\phi}' = -\sin(\phi')\hat{\mathbf{x}}' + \cos(\phi')\hat{\mathbf{y}}' & (3.37) \end{cases}$$

TE Modes

The resultant expression of (3.32) and (3.33) after applying (3.36) and (3.37) is:

$$\begin{aligned} \vec{\mathbf{E}}_{t,ap,TE} = & \frac{-j\omega\mu n}{k_c^2\rho'} C_n(k_c\rho') \begin{pmatrix} -\sin(n\phi') \\ \cos(n\phi') \end{pmatrix} [\cos(\phi')\hat{\mathbf{x}}' + \sin(\phi')\hat{\mathbf{y}}'] \\ & + \frac{j\omega\mu}{k_c} C_n'(k_c\rho') \begin{pmatrix} \cos(n\phi') \\ \sin(n\phi') \end{pmatrix} [-\sin(\phi')\hat{\mathbf{x}}' + \cos(\phi')\hat{\mathbf{y}}'] \end{aligned} \tag{3.38}$$

And the electric field for each coordinate can be written as

$$E_{ap,x} = \frac{-j\omega\mu}{2k_c} \left[C_{n-1}(k_c\rho') \begin{pmatrix} -\sin((n-1)\phi') \\ \cos((n-1)\phi') \end{pmatrix} + C_{n+1}(k_c\rho') \begin{pmatrix} -\sin((n-1)\phi') \\ \cos((n-1)\phi') \end{pmatrix} \right], \tag{3.39}$$

$$E_{ap,y} = \frac{-j\omega\mu}{2k_c} \left[-C_{n-1}(k_c\rho') \begin{pmatrix} \cos((n-1)\phi') \\ \sin((n-1)\phi') \end{pmatrix} + C_{n+1}(k_c\rho') \begin{pmatrix} \cos((n-1)\phi') \\ \sin((n-1)\phi') \end{pmatrix} \right]. \tag{3.40}$$

TM Modes

The resultant expression of (3.34) and (3.35) after applying (3.36) and (3.37) is:

$$\vec{\mathbf{E}}_{t,ap,TM} = \frac{-\gamma}{k_c} C_n'(k_c\rho') \begin{pmatrix} \cos(n\phi') \\ \sin(n\phi') \end{pmatrix} [\cos(\phi')\hat{\mathbf{x}}' + \sin(\phi')\hat{\mathbf{y}}'] \tag{3.41}$$

$$- \frac{\gamma n}{k_c^2\rho'} C_n(k_c\rho') \begin{pmatrix} -\sin(n\phi') \\ \cos(n\phi') \end{pmatrix} [-\sin(\phi')\hat{\mathbf{x}}' + \cos(\phi')\hat{\mathbf{y}}'] \tag{3.42}$$

As it has been done for the TE modes, the electric field is separated in

$$E_{ap,x} = \frac{-\gamma}{2k_c}\left[C_{n-1}(k_c\rho')\begin{pmatrix}\cos((n-1)\phi')\\ \sin((n-1)\phi')\end{pmatrix} - C_{n+1}(k_c\rho')\begin{pmatrix}\cos((n+1)\phi')\\ \sin((n+1)\phi')\end{pmatrix}\right], \tag{3.43}$$

$$E_{ap,y} = \frac{-\gamma}{2k_c}\left[C_{n-1}(k_c\rho')\begin{pmatrix}-\sin((n-1)\phi')\\ \cos((n-1)\phi')\end{pmatrix} + C_{n+1}(k_c\rho')\begin{pmatrix}-\sin((n+1)\phi')\\ \cos((n+1)\phi')\end{pmatrix}\right]. \tag{3.44}$$

3.4.3 Integration of the Field at the Aperture

The components of the electric field presented on the previous section are used to compute the values P_x and P_y described in Section 3.2.

Defining

$$b_{n,\binom{c}{s}}(\theta,\phi) = \int_{\phi'=-\pi}^{\pi}\int_{\rho'=r_i}^{r_e} C_n(k_c\rho')\begin{pmatrix}\cos(n\phi')\\ \sin(n\phi')\end{pmatrix} e^{jk\rho'\sin(\theta)\cos(\phi-\phi')}\rho' d\rho' d\phi' = \tag{3.45}$$

$$= \begin{pmatrix}\cos(n\phi)\\ \sin(n\phi)\end{pmatrix}\frac{(2\pi j^n)}{k_c^2-k_\theta^2}\left[\xi k\sin(\theta)C_n(k_c\xi)J_n'(k_\theta\xi) - \xi k_c C_n'(k_c\xi)J_n(k_\theta\xi)\right]_{\xi=r_i}^{\xi=r_e}, \tag{3.46}$$

where the Lommel Integral has been used [12]. Note that the integration is defined between an internal and external radius. This is the general expression that also includes the case of a coaxial aperture, the result for a circular aperture can be obtained by making $r_i = 0$. For the TE modes the integrations can be calculated as follows:

$$P_{x,TE} = \int_{\phi'=-\pi}^{\pi}\int_{\rho'=r_i}^{r_e} E_{ap,x\binom{-s}{c}} e^{jk\rho'\sin(\theta)\cos(\phi-\phi')}\rho' d\rho' d\phi' = \tag{3.47}$$

$$= \frac{-j\omega\mu}{2k_c}\left(b_{n-1,\binom{-s}{c}}(\theta,\phi) + b_{n+1,\binom{-s}{c}}(\theta,\phi)\right), \tag{3.48}$$

and

$$P_{y,TE} = \int_{\phi'=-\pi}^{\pi}\int_{\rho'=r_i}^{r_e} E_{ap,y\binom{c}{s}} e^{jk\rho'\sin(\theta)\cos(\phi-\phi')}\rho' d\rho' d\phi' = \tag{3.49}$$

$$= \frac{-j\omega\mu}{2k_c}\left(-b_{n-1,\binom{c}{s}}(\theta,\phi) + b_{n+1,\binom{c}{s}}(\theta,\phi)\right). \tag{3.50}$$

Operating similarly for the TM modes:

$$P_{x,TM} = \int_{\phi'=-\pi}^{\pi}\int_{\rho'=r_i}^{r_e} E_{ap,x\binom{c}{s}} e^{jk\rho'\sin(\theta)\cos(\phi-\phi')}\rho' d\rho' d\phi' = \tag{3.51}$$

$$= \frac{-\gamma}{2k_c}\left(b_{n-1,\binom{c}{s}}(\theta,\phi) - b_{n+1,\binom{c}{s}}(\theta,\phi)\right), \tag{3.52}$$

and

$$P_{y,TM} = \int_{\phi'=-\pi}^{\pi} \int_{\rho'=r_i}^{r_e} E_{ap,y\binom{-s}{c}} e^{jk\rho' \sin(\theta)\cos(\phi-\phi')} \rho' d\rho' d\phi' = \tag{3.53}$$

$$= \frac{-\gamma}{2k_c} \left(b_{n-1,\binom{-s}{c}}(\theta,\phi) + b_{n+1,\binom{-s}{c}}(\theta,\phi) \right). \tag{3.54}$$

Q_x and Q_y can be obtained using the relations in (3.11) without the need to compute any new integrations.

3.5 Conclusions

In this chapter the radiation integrals for rectangular and circular apertures with an arbitrary configuration of modes have been deployed. The obtained formulas allow to calculate the radiation pattern of different antennas aperture antennas when they are excited by their fundamental mode but also when undesired high order modes appear at the antenna input. These computations have been entirely derived in this work, using the intermediate results found in the technical literature.

Additionally, these radiation integrals have been implemented using the three different equivalence principles. This will allow to select the most appropriate principle depending on the problem under study.

4

Horn Simulation Using Mode-Matching

4.1 Motivation

As it was stated in Chapter 1 the initial part of this work is based on the natural evolution of [1]. There, a Mode-Matching approach to horn antenna simulation was already presented. A schematic representation of this simulation process can be found in Figure 4.1. The present chapter is devoted to present this approach since it forms the basis of this project, but also their weaknesses will be highlighted, in order to illustrate the limitations of the previous works in this topic. In Chapter 5 a new and more advanced model will be proposed to overcome them.

4.2 Topology of the Model

The Mode-Matching technique is conceived, in its more classical form in microwave components, to solve closed waveguide discontinuity problems. However, analysing an antenna is not a closed but a radiation problem. Therefore when trying to create an approach for simulating horn antennas using the Mode-Matching technique it is mandatory to define a closed topology that

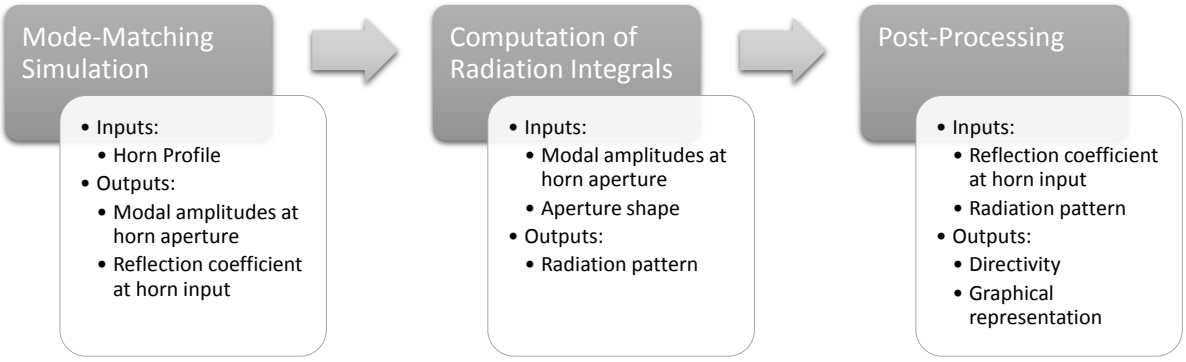

Figure 4.1: Schematic representation of the simulation process.

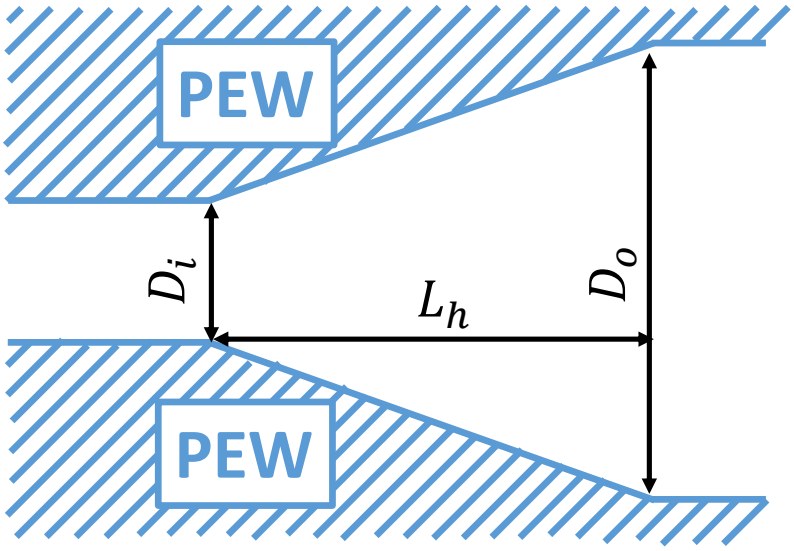

Figure 4.2: Schematic representation of the simple horn model.

approximately corresponds with the radiation problem. The better this approximated model represents the reality, the best the results that will be obtained.

A simple model that can be considered on a first approach (and indeed was the topology used in [1]) is the "two-port" model. A representation of this topology can be found in Figure 4.2.

In this topology the horn is modelled as a two-port waveguide device, where one port corresponds with the horn input and the other corresponds with the horn aperture. In this topology the horn can be seen as an impedance transformer between the impedance at the horn input and the free space impedance.

The main limitation of this topology is that it does not model lateral radiation accurately since the boundaries of the problem are set by the horn walls (instead of being surrounded by free space, as it will be the case with an antenna operating in a real scenario). This should not be a great concern since usually horn antennas have a great directivity and therefore present low levels of lateral radiation. Nevertheless it was shown in [1] that even with average directivity horn antennas this topology leads to inaccuracies in the computed Side Lobe Level (SLL)[1].

Additionally, the two-port topology is also incapable of modelling an open ended waveguide since in this topology both of the ports are terminated and therefore there is no waveguide step to analyse (indeed, the result is that there is a perfect transmission between the two ports).

4.3 Discretization of the Horn Profile

Since the Mode-Matching method characterizes waveguide steps, the profile of the horn must be modelled as a succession of these steps. This process is trivial for corrugated horns where each corrugation can be seen as a waveguide discontinuity, but it can get tricky when dealing with smooth horns. In the case of non-corrugated horns the walls are represented by a continuous

[1]Side Lobe Level: Ratio between the radiated field in the direction of maximum radiation and the radiated field on the first side lobe.

function that must be sampled to define waveguide steps in order to obtain a discrete model of the horn profile.

In [1] two different discretization methods were defined and compared, and it was demonstrated that both of them led up to the same results. They were called the "hold" and the "middle-point" methods and a depiction of both can be found at Figure 4.3 on the next page.

It is important to note that convergence of the results must be studied by increasing the number of steps in which the horn is divided until it is noticed that the differences at the results become negligible for the application under study.

4.4 Simulation Process

Once that the topology and its discrete representation are defined, the Generalized Scattering Matrix [2] of the two port device is computed using the Mode-Matching analysis and then it is used to obtain the modal amplitudes at the horn aperture. This is represented at Figure 4.4 on page 27.

To perform this analysis the number of modes considered at each waveguide section must be defined. The approach adopted is that the number of modes at the horn aperture is defined by the user and then the number of modes at each other waveguide section is computed proportionally using the ratio of the waveguide sections. It is important to consider that the number of modes at the aperture affects to the convergence and therefore several simulations should be performed progressively increasing this parameter until convergence is reached.

These modal amplitudes are used to compute the radiation pattern for the antenna under study. The electric field at the aperture must be integrated, but since

$$\vec{\mathbf{E}}_{ap} = \begin{cases} \sum_m \left\{ b_m^{TE} \vec{\mathbf{e}}_m^{TE} + b_m^{TM} \vec{\mathbf{e}}_m^{TM} \right\} & , \textit{ at horn aperture} \\ 0 & , \textit{ elsewhere} \end{cases}, \tag{4.1}$$

the radiation pattern can be computed by the combination of the radiation pattern produced by each mode. Schematically (for the actual integrals please see Chapter 3), the integrals that have to be solved are:

$$\vec{\mathbf{E}}_{rad} = \int_{S_a} \vec{\mathbf{E}}_{ap} e^{jk_0 \hat{\mathbf{r}} \cdot \vec{\mathbf{r}}} dS_a = \int_{S_a} \sum_m b_m \vec{\mathbf{e}}_m e^{jk_0 \hat{\mathbf{r}} \cdot \vec{\mathbf{r}}} dS_a = \sum_m b_m \int_{S_a} \vec{\mathbf{e}}_m e^{jk_0 \hat{\mathbf{r}} \cdot \vec{\mathbf{r}}} dS_a. \tag{4.2}$$

First the radiation pattern produced by each one of the modes at the horn aperture is computed using the formulas developed in Chapter 3, and then the radiation pattern of the antenna is obtained by the combination of the radiation pattern associated with each modes weighted by its modal amplitude (these modal amplitudes are obtained using the Mode-Matching software following the flow illustrated in Figure 4.1).

4.5 Case Studies

To demonstrate the usefulness of the presented method several antennas have been simulated using the developed Mode-Matching software and the obtained results have been compared

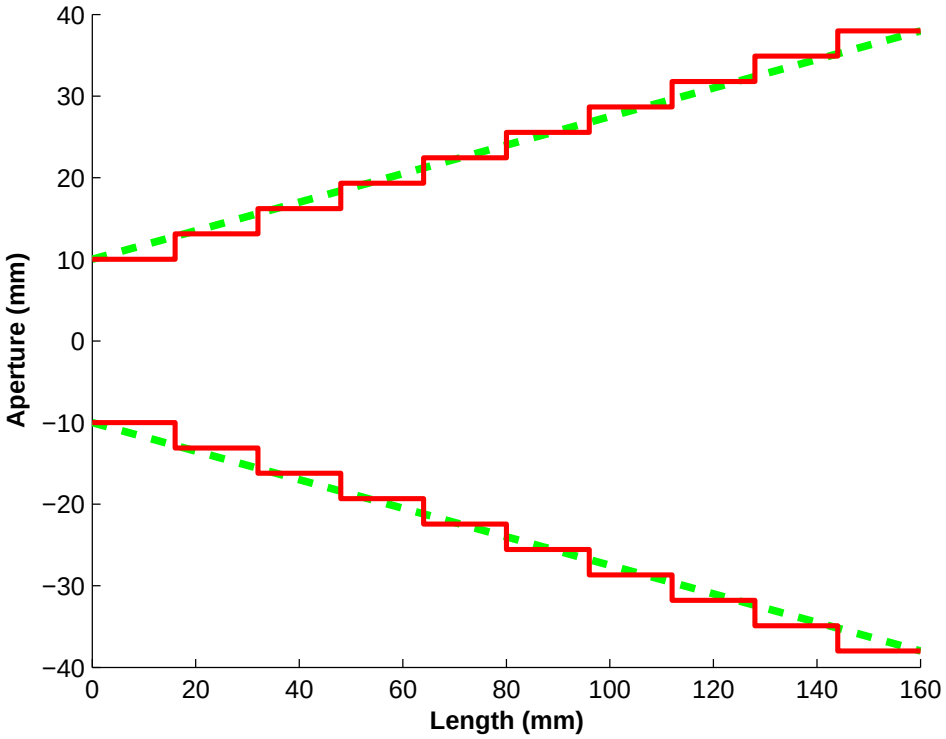

(a) Hold method

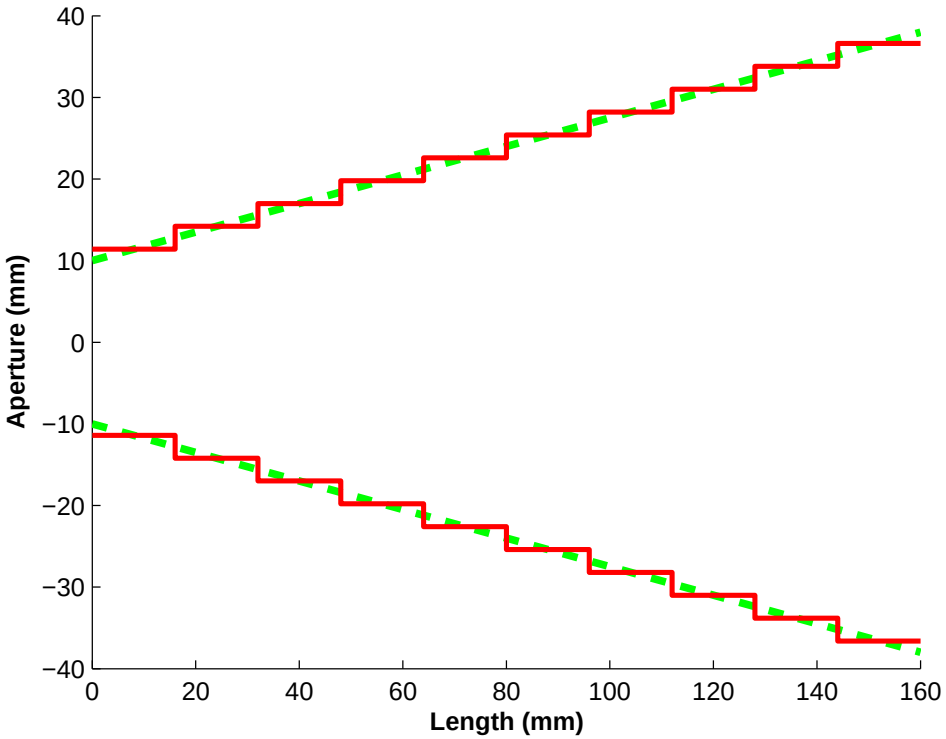

(b) Middle-point method

Figure 4.3: Representation of the two methods used to model a smooth horn. Dashed green shows the real profile and solid red the discrete one.

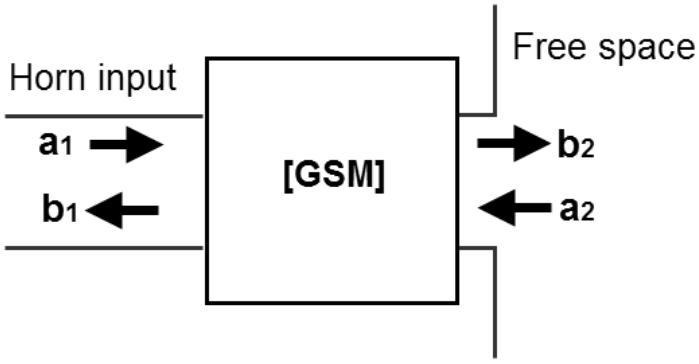

Figure 4.4: Horn antenna characterized by its GSM.

against reference models (e.g.: Simulations performed with commercial tools or data provided by other authors). In this section some of these case studies will be presented.

Since all the case studies of Chapter 5 will be horns with circular apertures this chapter will be devoted to rectangular horn antennas (the dimensions of the antennas, as well as other simulation parameters, can be found in Table 4.1 on the next page). Nevertheless, the two-port topology presented in the previous sections also allows to analyse circular horn antennas, as it was shown by [1].

In the first two cases the Mode-Matching results are compared against a simulation using the commercial tool CST Microwave Studio. The first case study consists on a pyramidal horn and the second in an E-Plane sectoral horn. The obtained radiation patterns can be found in Figures 4.5 and 4.6 respectively. It can be seen that the Mode-Matching results show a good agreement with the CST simulation. The situation where there is less agreement is the H-Plane of the sectoral horn and this phenomenon can be easily explained. In the sectoral horn the H-Plane does not have a flare angle (i.e.: In that plane the dimension of the waveguide does not change) and therefore the antenna presents a lot of lateral radiation in that plane (it can be seen that the beamwidth in the H-Plane is a lot greater than in the E-Plane). As it was stated in Section 4.2, one of the main limitations of the two-port topology is that it does not model lateral radiation accurately and therefore since this antenna presents a really big beamwidth in this plane, the radiation pattern is not computed as exactly as in the other cases.

The third case consists on a pyramidal horn presented in [13] and the Mode-Matching results are compared against the ones provided by the original author. The radiation pattern is represented in Figure 4.9 and it can be seen that the results match almost exactly in the main lobe but there are some differences in the secondary lobes. The explanation for this is that the data provided by [13] does not correspond just with a horn antenna but with a horn antenna fed by a coaxial to waveguide transition. The reason which leads to think that the transition is the source of the mismatch is found in the asymmetry of the radiation pattern at each plane; the theoretical radiation pattern of a horn antenna in a given plane has a symmetry axis along the direction of maximum radiation. The transition can affect the radiation pattern in two different ways: First, the transition may affect to the purity of the excitation at the input of the horn and; second, the coaxial line is modifying the outer shape of the antenna, which can disrupt the radiation pattern.

To demonstrate that the coaxial to waveguide transition is indeed the cause of the mismatch, the horn proposed by [13] has been simulated (without the transition) using CST Microwave Studio. The result (compared with the previous Mode-Matching simulation) can be found in

Parameter	Case 1)	Case 2)	Case 3)
a_{in}	7.112	7.112	23.000
b_{in}	3.556	3.556	11.000
$a_{aperture}$	116.109	7.112	67.500
$b_{aperture}$	77.406	63.000	50.000
L_{horn}	86.946	189.000	108.500
N_{steps}	200	200	200
N_{modes}	200	200	201

Table 4.1: Dimensions of the horns for the case studies (all values are in millimetres) and simulation parameters (number of steps used to discretize the profile and number of modes at the aperture).

Figure 4.10. As it can be seen, in this case the match is almost perfect.

4.6 Conclusions

This chapter described the process of simulating a horn antenna using the Mode-Matching technique, which can be summarized in the following steps:

1. Define the topology.
2. Discretize the model.
3. Perform Mode-Matching analysis.
4. Compute radiation pattern.
5. Present the results.

The first three steps correspond with the first block of the diagram in Figure 4.1 and fourth and fifth steps correspond with the second and third block respectively.

It is important to note that in steps two and three are defined two parameters that affect significantly to convergence, the number of steps and the number of modes at the horn aperture.

Additionally, the topology presented in this chapter is very simple and therefore it does not offer a good representation of lateral radiation. In Chapter 5 an improved model that overcomes this limitation will be presented.

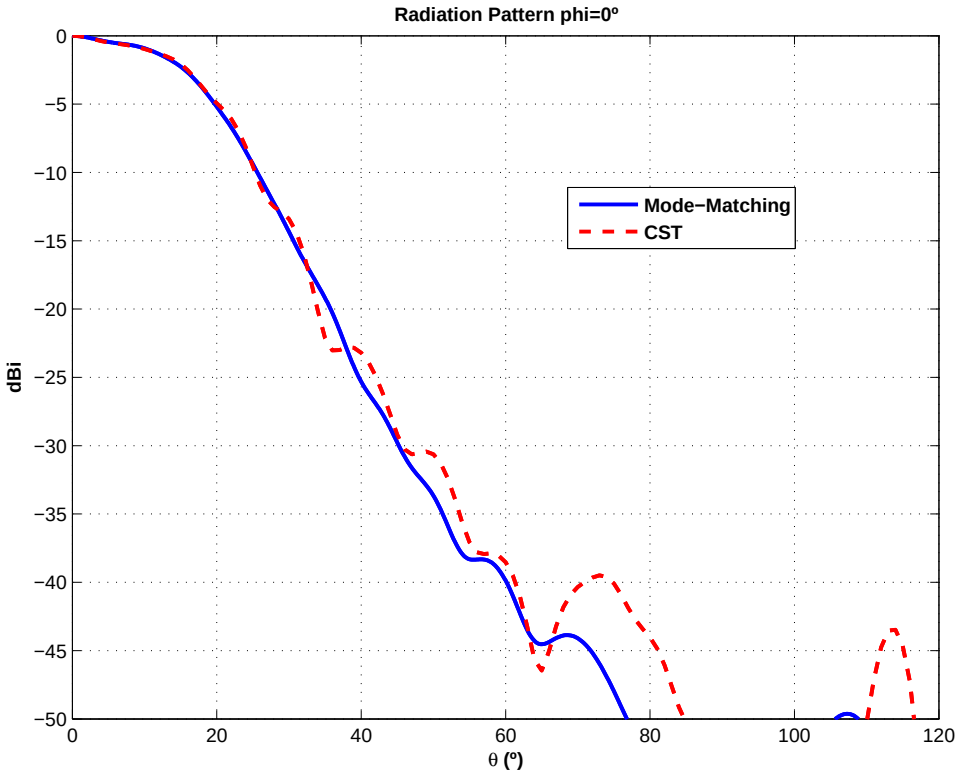

(a) H-Plane ($\phi = 0°$). $D_{0,MM} = 17.12dBi, D_{0,CST} = 16.7dBi$.

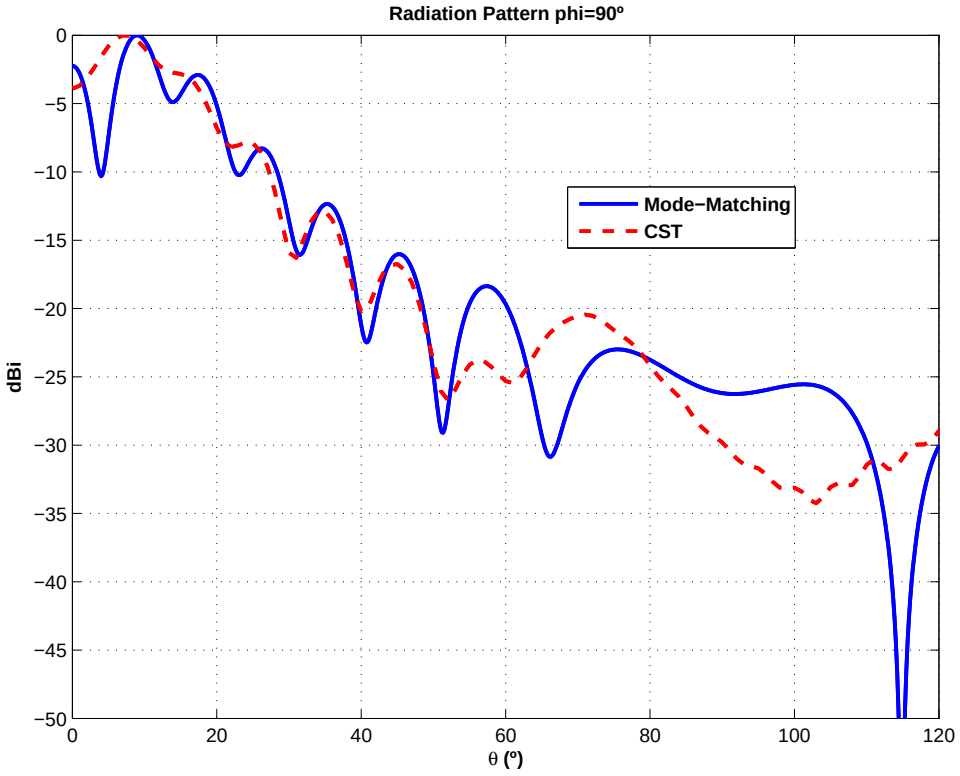

(b) E-Plane ($\phi = 90°$). $D_{0,MM} = 12.9dBi, D_{0,CST} = 14.88dBi$.

Figure 4.5: Radiation pattern (at $30GHz$) of case study 1 (see Table 5.1). Comparison between our model (Mode-Matching) and commercial software (CST).

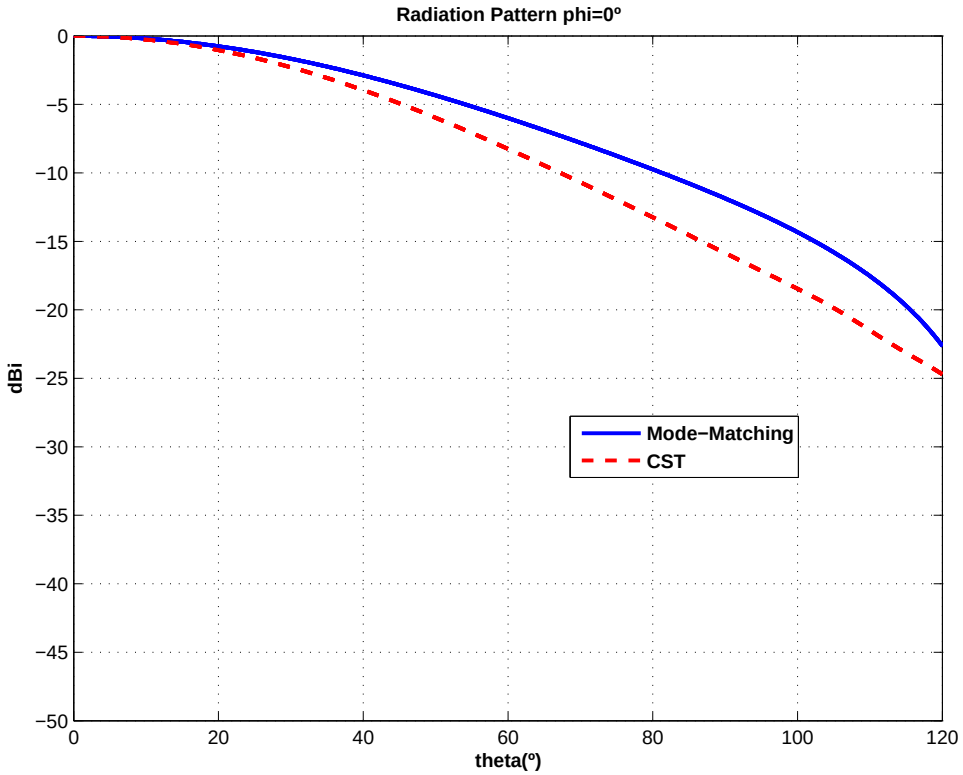

(a) H-Plane ($\phi = 0°$)

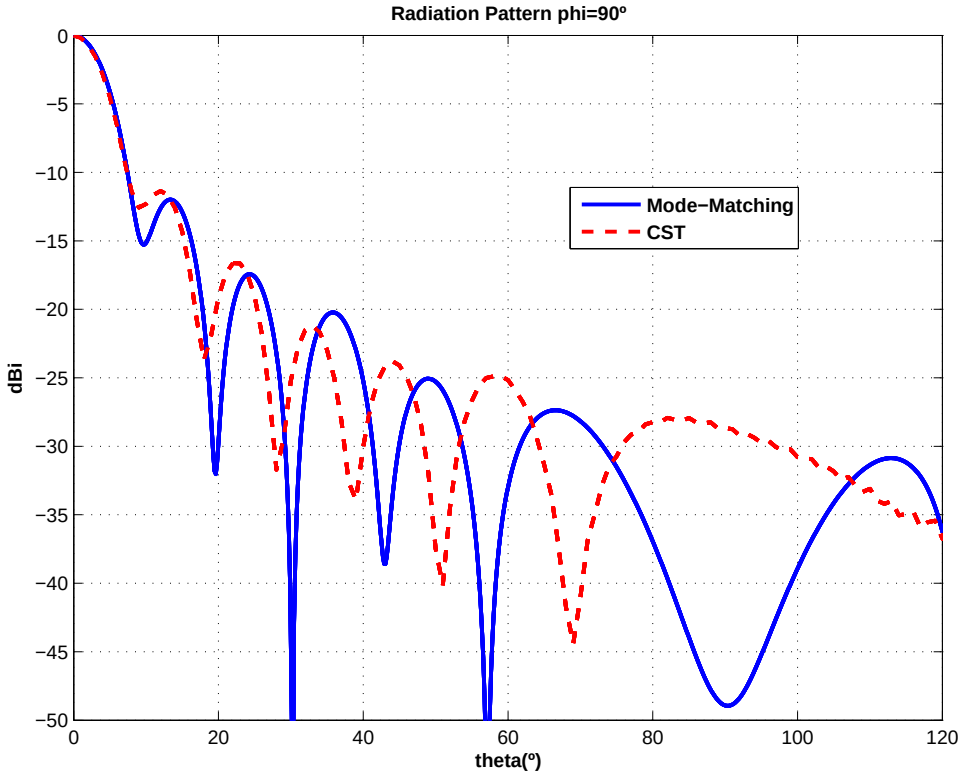

(b) E-Plane ($\phi = 90°$)

Figure 4.6: Radiation pattern (at $30GHz$) of case study 2 (see Table 5.1). $D_{0,MM} = 16.2dBi, D_{0,CST} = 17.2dBi$. Comparison between our model (Mode-Matching) and commercial software (CST).

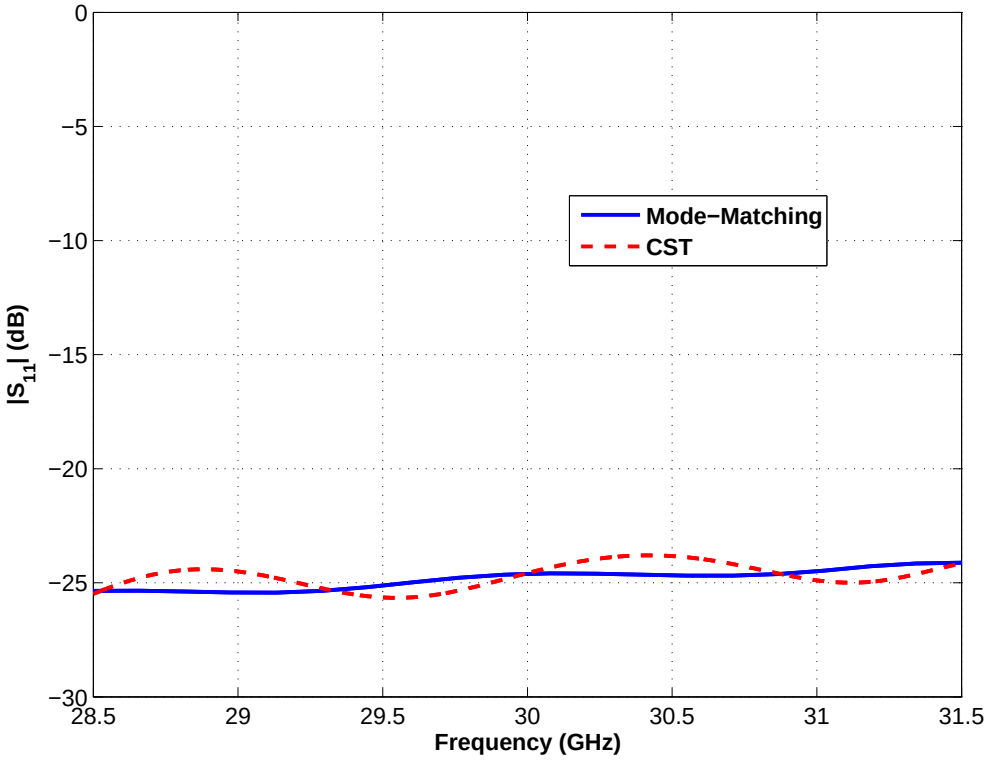

Figure 4.7: Module of the S_{11} parameter of case study 1. Comparison between our model (Mode-Matching) and commercial software (CST).

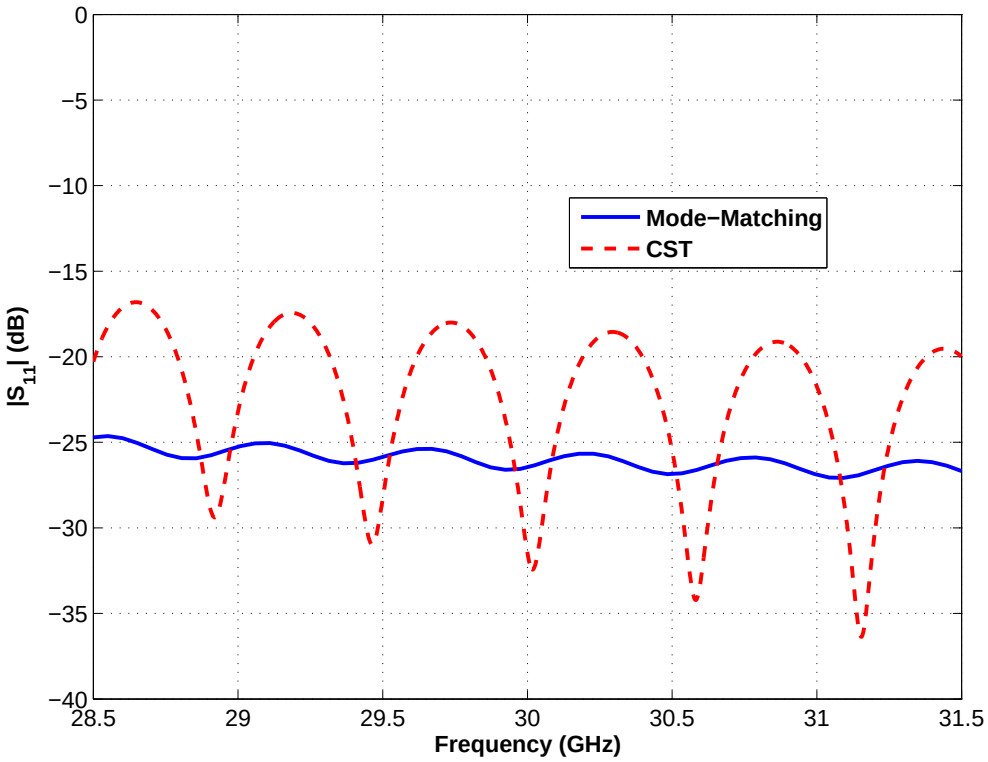

Figure 4.8: Module of the S_{11} parameter of case study 2. Comparison between our model (Mode-Matching) and commercial software (CST).

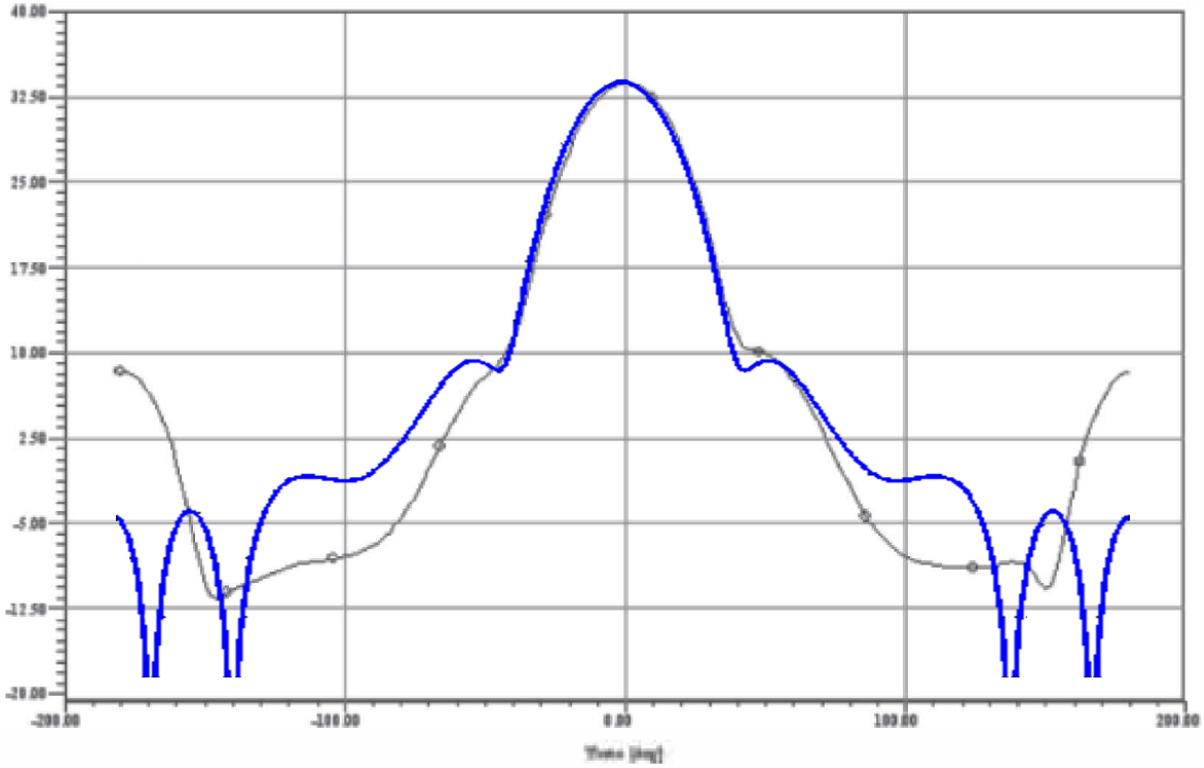

(a) H-Plane ($\phi = 0°$)

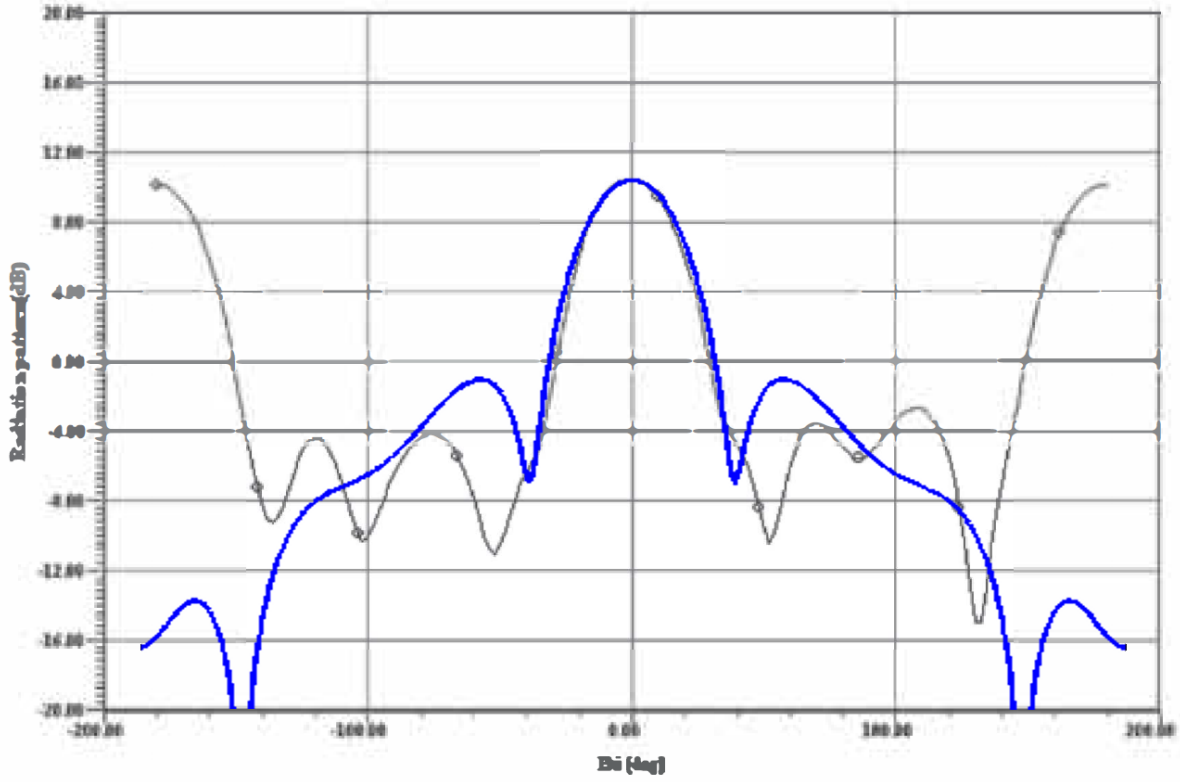

(b) E-Plane ($\phi = 90°$)

Figure 4.9: Radiation pattern (at $10GHz$) of horn the pyramidal horn presented in [13] (see Table 5.1, case study 3). The Mode-Matching results (blue) are superimposed on the ones provided by the original author (grey). $D_{0,MM} = 15.65dBi, D_{0,Ref} = 15.8dBi$.

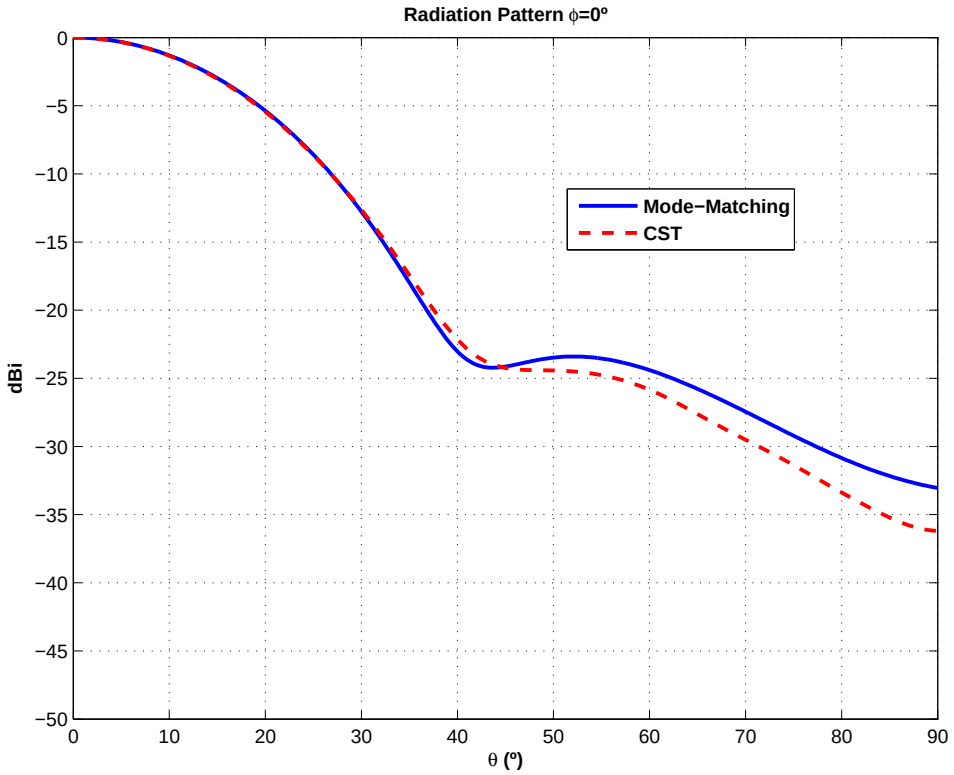

(a) H-Plane ($\phi = 0°$)

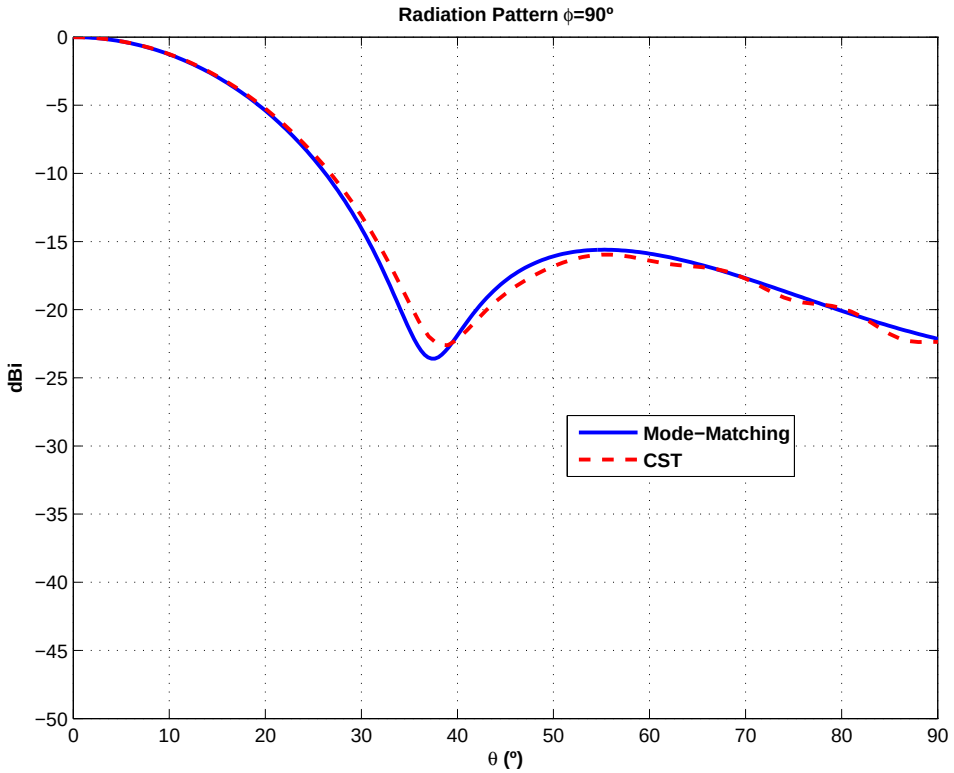

(b) E-Plane ($\phi = 90°$)

Figure 4.10: Radiation pattern of case study 3 (see Table 5.1). Mode-Matching simulation compared against CST. $D_{0,MM} = 15.65dBi, D_{0,CST} = 15.8dBi$.

5

Improved Mode-Matching Model of a Horn Antenna

5.1 Motivation

As it was stated earlier, the model presented in Chapter 4 to analyse a horn antenna using the Mode-Matching technique has some serious weaknesses. Most of them arise from the fact that it can not model the lateral radiation of the antenna properly, and therefore only highly directive ($D_0 > 12dBi$) antennas are simulated accurately.

In this chapter a more sophisticated model is presented where the horn antenna is enclosed inside of a circular waveguide. This new topology allows to model the lateral as well as the back radiation of the antenna.

A comparison between the two topologies is presented in order to demonstrate the utility of the improved model.

5.2 Presentation of the Model

A diagram representing the topology of the model can be found in Figure 5.1 on page 37. This topology is a three-port problem, including the input, the aperture, and an additional coaxial port at the horn input [14].

In this topology the horn profile is enclosed inside a bigger waveguide of diameter D_{wg} that should be around an order of magnitude greater than D_o. The boundary condition imposed by the outer waveguide is set, in different runs, as Perfect Electric Wall (PEW) and Perfect Magnetic Wall (PMW)[1]. Then the reflection coefficient of the antenna (S_{11}) will be obtained as

$$S_{11} = \frac{S_{11PEW} + S_{11PMW}}{2}, \tag{5.1}$$

and proceeding in an similar way the farfield radiation pattern can be obtained.

[1]This conditions are imposed by the PEC and PMC presented in Chapter 2.

This is introducing a boundary condition analogous to the perfectly-matched boundary [15, 16] where, by combining the results obtained by the model with PEW and PMW, the waves reflected at the outer waveguide cancel each other. This cancellation is used to approximate the scenario of an antenna radiating in the free space.

It is important to note that in this model the radiation integral is not calculated over the horn aperture but over the big waveguide of diameter D_{wg}, at the interface represented by a dashed line on Figure 5.1. It must be done on this way in order to consider the effect of backward and lateral radiation.

As it will be shown, the three-port model should provide with better results than the two-port model specially for antennas that do not have a great directivity value ($D_0 < 12dBi$).

The three-port model presents a couple of additional advantages over the two-port model. First, it can take on account the effect of w_f (the thickness of the horn aperture rim). This may be of significant importance when w_f is relatively big compared with D_o but it also allows to use the parameter w_f to model a horn with a flange.

And second, this approach allows to properly simulate an open-ended waveguide. Not only because an open waveguide has a lot of lateral radiation and therefore the three-port model gives better results when computing the radiation pattern, but also because with the two-port model it is impossible to compute the S_{11} parameter of an open waveguide. The reason for this is that when using the two-port model there is no discontinuity between the two ports and therefore a perfect transmission is obtained, which yields to a perfect adaptation ($|S_{11}| = -\infty dB$).

An example of this can be found in Figure 5.2 on page 38. The circular waveguide has a radius of $13.3975mm$ and the radiation patterns have been computed at $10GHz$.

5.3 Case Studies

In order to demonstrate the improvement achieved by the three-port model two different horn antennas will be simulated using both the two-port and the three-port models. One of them has a very high directivity value whereas the other has a low directivity. The dimensions of these horns can be found in Table 5.1 on page 42.

Both horns have also been simulated using CST microwave Studio in order to obtain a reference model to compare the Mode-Matching results with. It is expected that for Horn A both Mode-Matching models match the CST results but for Horn B the three-port model obtains a significant better match than the two-port model.

The module of the S_{11} parameter for both antennas is shown in Figure 5.3 on page 39. It can be clearly seen that the results are as expected: whereas for horn A the three-port model matches significantly better the CST results than the two-port model, this difference is not so great for the horn B.

As it can be seen in Figure 5.4 on page 40 the three-port model also improves the results obtained when computing the radiation pattern of the low directivity horn. On the other hand, as Figure 5.5 on page 41 shows, there is no big improvement on the radiation pattern of the high directivity antenna since the two-port model already provides very accurate results. Although the H-plane cut is now more accurate.

Finally, to show that not only extreme theoretical cases but also practical antennas can benefit from the Three-Port model approach, a conical antenna presented in [17] has been

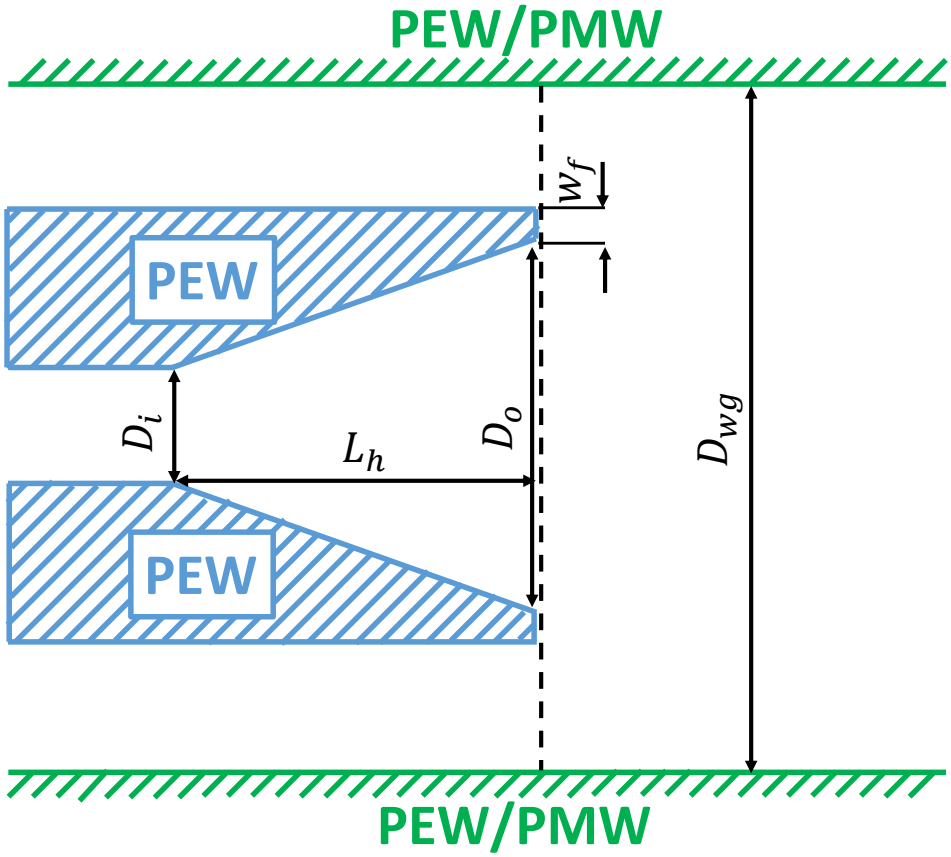

(a) Lateral view

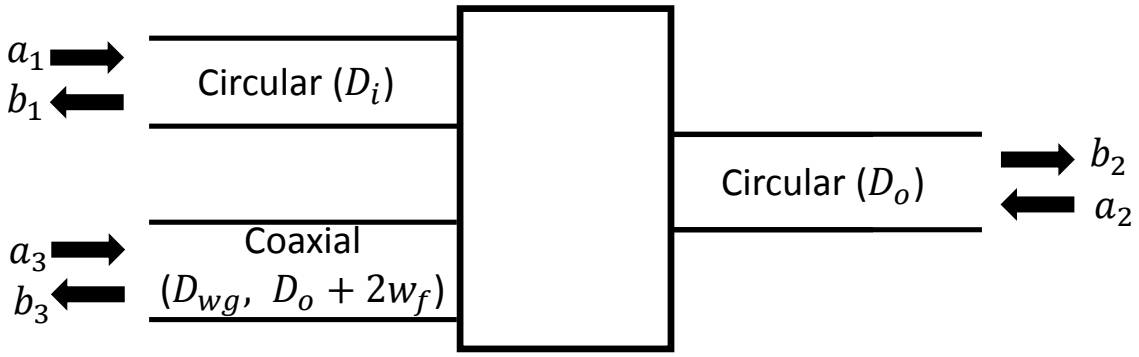

(b) Circuital representation

Figure 5.1: Representation of the improved horn model.

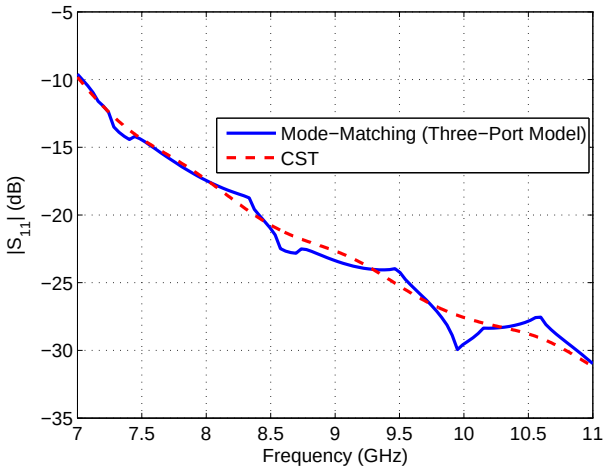

(a) Reflection coefficient

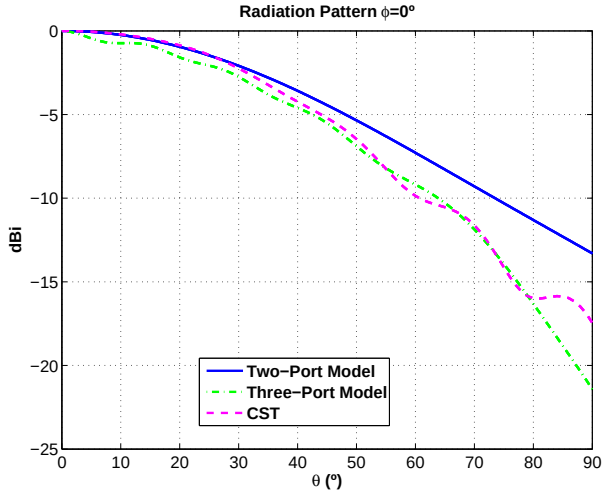

(b) Radiation pattern (at $10GHz$), H-Plane ($\phi = 0°$)

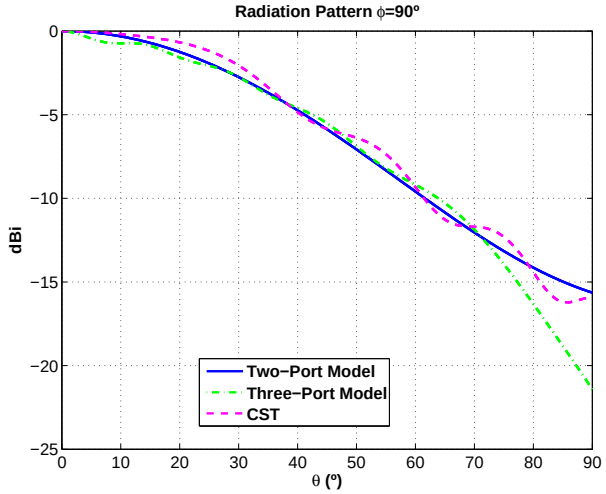

(c) Radiation pattern (at $10GHz$), E-Plane ($\phi = 90°$)

Figure 5.2: Simulation of an open-ended waveguide of $r = 13.3975mm$. No results of adaptation using the two-port model are presented because the model can not compute that parameter (in fact, it would provide perfect matching, i.e. $S_{11} = 0$ in natural units).

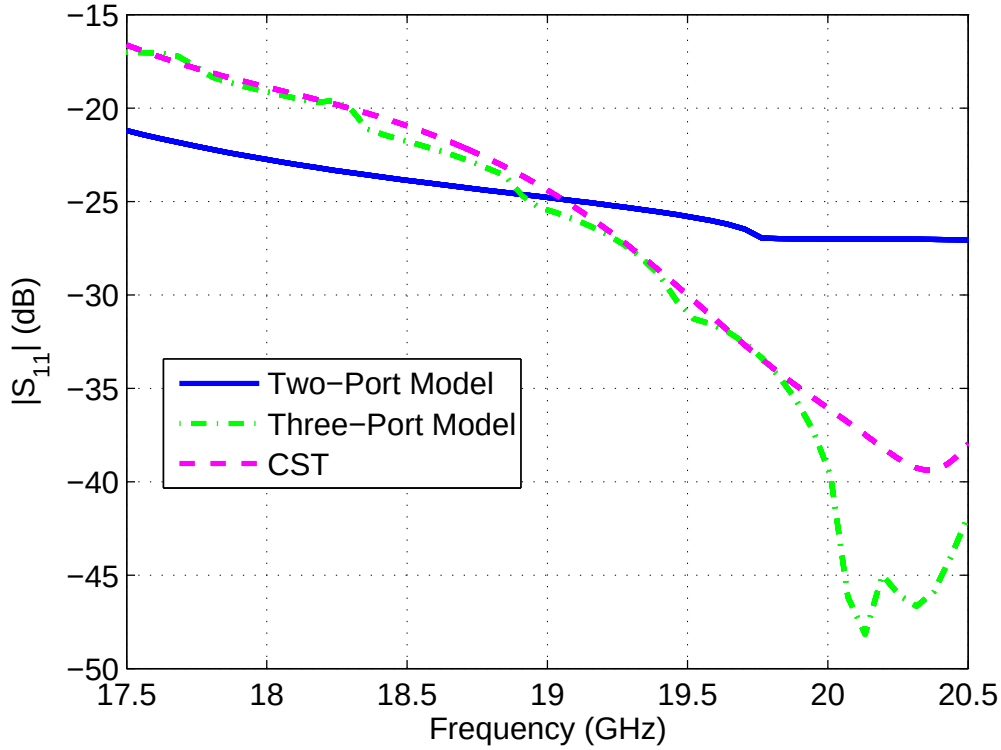

(a) Horn A

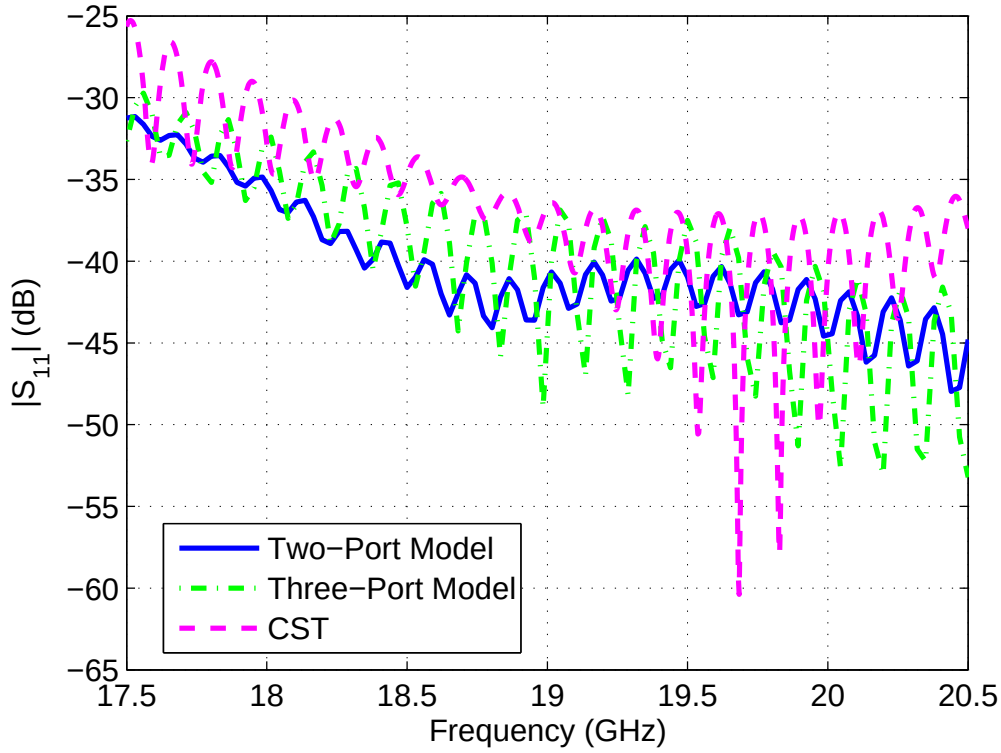

(b) Horn B

Figure 5.3: Module of the S_{11} parameter of a low directivity horn (a) and a high directive one (b) using the two-port model, the three-port model and a commercial simulator.

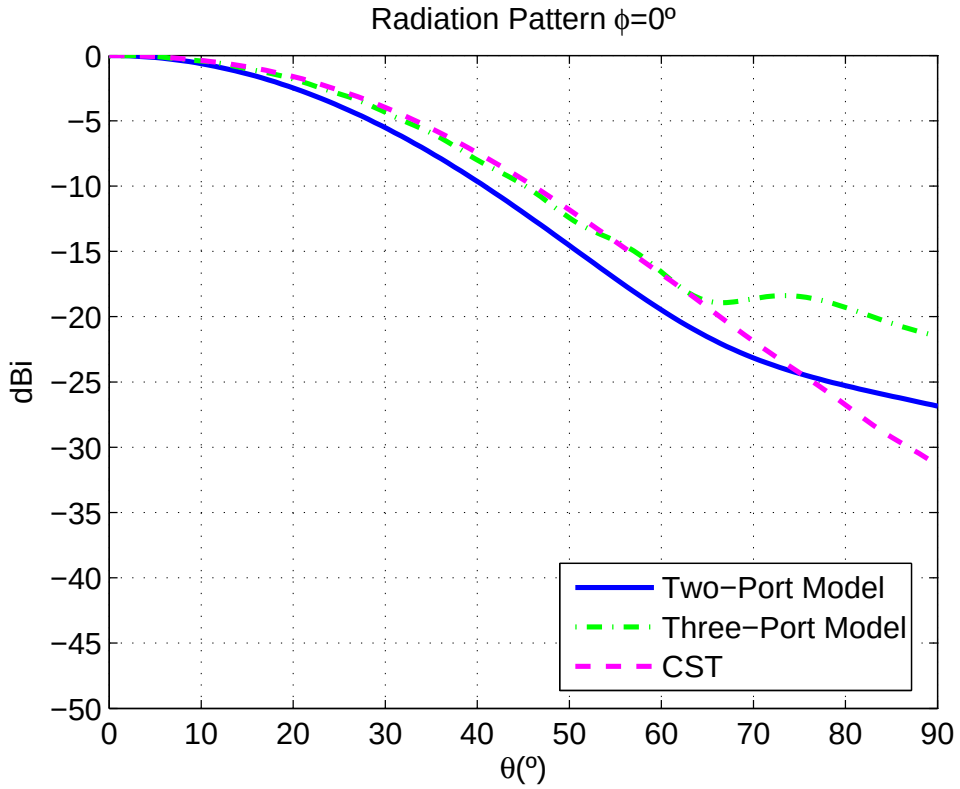

(a) H-Plane ($\phi = 0°$), $D_{0,MM,2P} = 13.17dBi, D_{0,MM,3P} = 11.94dBi, D_{0,CST} = 11.3dBi$.

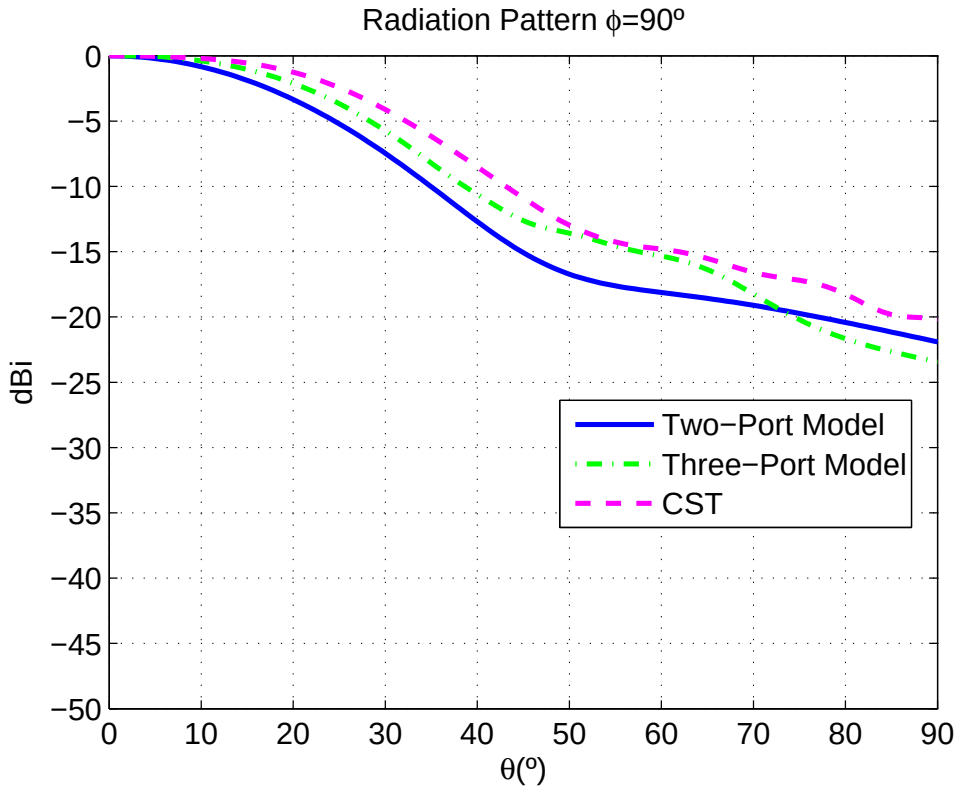

(b) E-Plane ($\phi = 90°$), $D_{0,MM,2P} = 13.17dBi, D_{0,MM,3P} = 11.89dBi, D_{0,CST} = 11.3dBi$.

Figure 5.4: Radiation pattern (at $19GHz$) of horn A (see Table 5.1) using the two-port and the three-port models, compared against a CST Microwave Studio simulation.

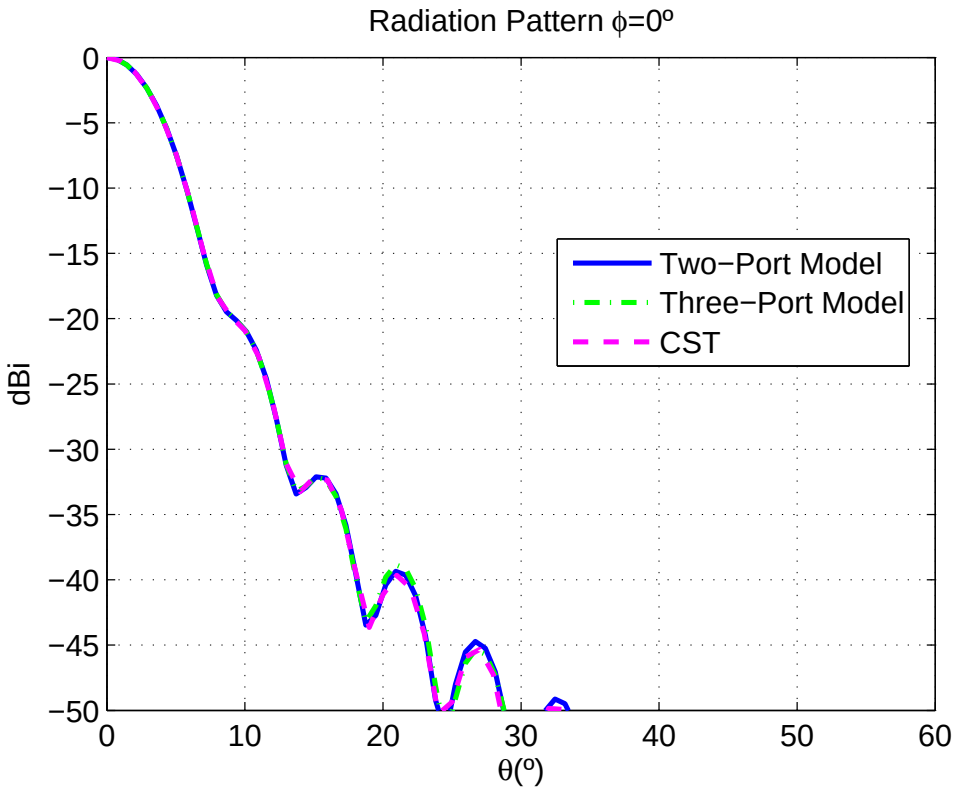

(a) H-Plane ($\phi = 0°$), $D_{0,MM,2P} = 29.52dBi, D_{0,MM,3P} = 29.57dBi, D_{0,CST} = 29.5dBi$.

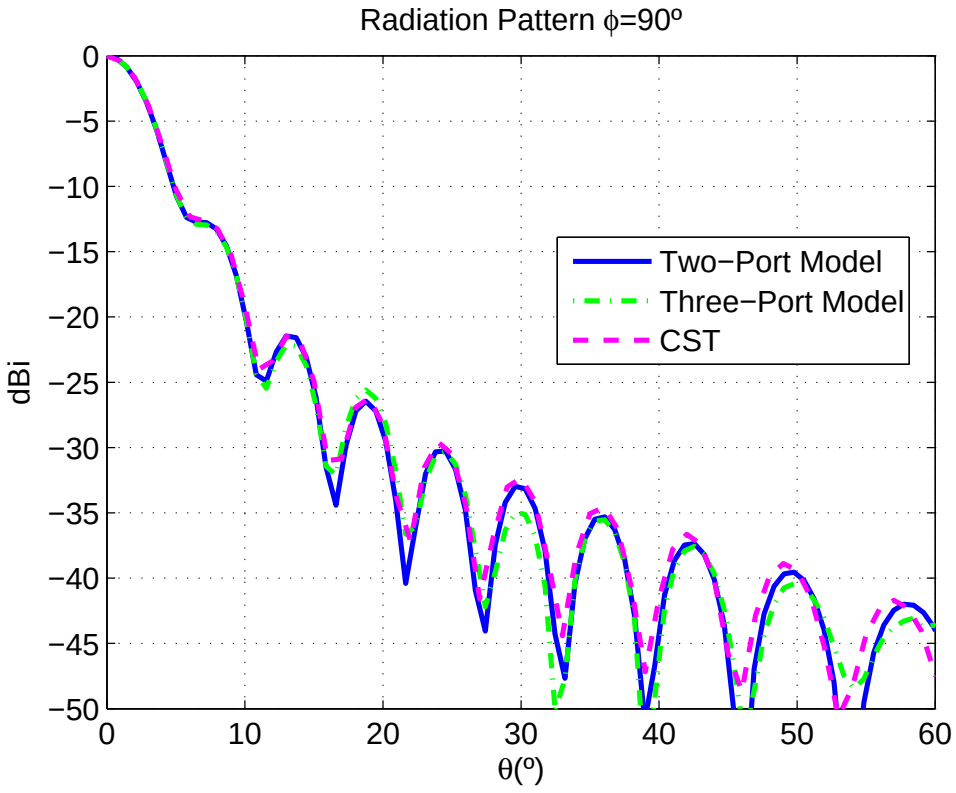

(b) E-Plane ($\phi = 90°$), $D_{0,MM,2P} = 29.52dBi, D_{0,MM,3P} = 29.57dBi, D_{0,CST} = 29.5dBi$.

Figure 5.5: Radiation pattern (at $19GHz$) of horn B (see Table 5.1) using the two-port and the three-port models, compared against a CST Microwave Studio simulation.

Parameter	Horn A)	Horn B)	Horn C)
D_i	11.56	11.56	18.00
D_o	23.80	182.20	70.00
L_h	11.64	974.05	302.50
w_f	8.20	8.20	8.20
N_{steps}	200	200	500
$N_{modes,2P}$	50	50	20
$N_{modes,3P}$	200	200	200

Table 5.1: Dimensions of the horns (all values are in millimetres) and simulation parameters (number of steps used to discretize the profile and number of modes at the aperture) for the case studies. Horn A is the low directivity horn (approximately 13dBi) and Horn B is the one with high directivity (30 dBi). Horn C is a real antenna presented in [17].

simulated using both topologies (see "Horn C" in Table 5.1). The obtained results have been superimposed with the ones obtained by a simulation using CST and they can be found in Figure 5.6 on the next page. It can be seen that in the spite of both topologies matching the main lobe with equivalent exactitude, the Three-Port model provides with better results when computing the secondary lobes. Additionally, as it can be seen in Figure 5.7 on page 44, the computation of the horn return loss also benefits from the Three-Port model.

5.4 Conclusions

In this chapter an improved model to analyse horn antennas using the Mode-Matching technique has been presented. This model overcomes some of the limitations that affected the two-port model presented in Chapter 4.

The key idea of the three-port model is to enclose the horn antenna inside a larger waveguide. This topology is still suitable for a Mode-Matching analysis but allows to model lateral radiation in a more realistic way than the two-port model.

Three case studies have been presented, showing that this approach indeed improves the accuracy of the results all the more when the antenna has a low directivity value.

Currently this topology has only been implemented for conical horns, but it could be also used to simulate rectangular horns by using a coaxial port with a rectangular inner conductor instead of a circular one.

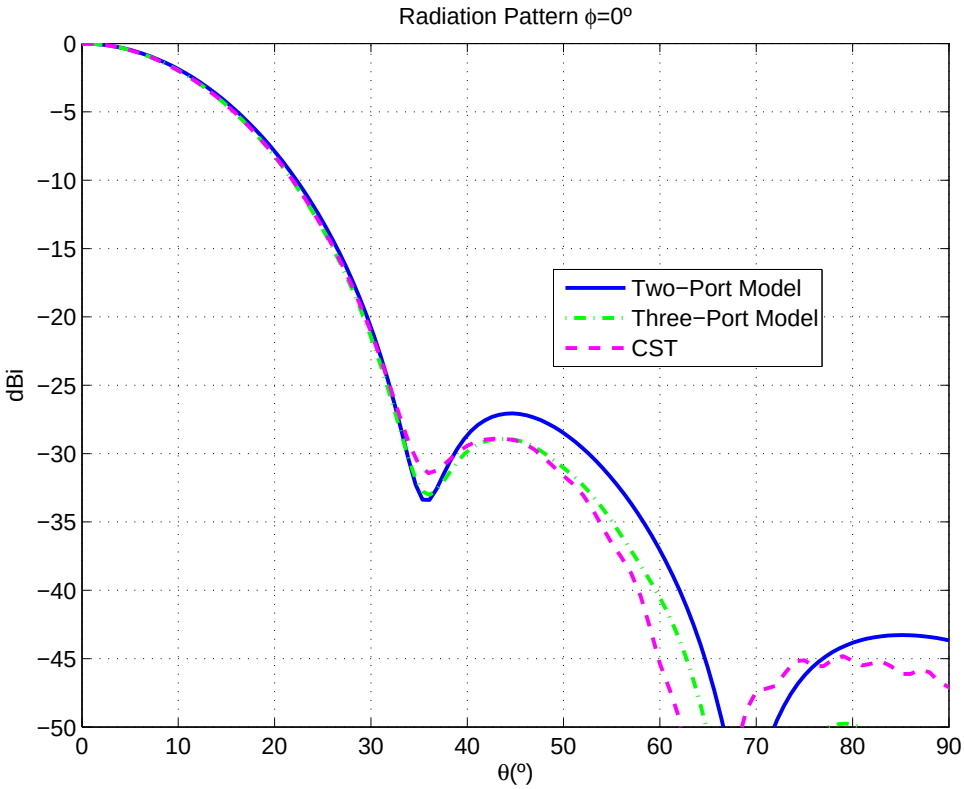

(a) H-Plane ($\phi = 0°$)$D_{0,MM,2P} = 18.42dBi, D_{0,MM,3P} = 18.47dBi, D_{0,CST} = 18.5dBi$

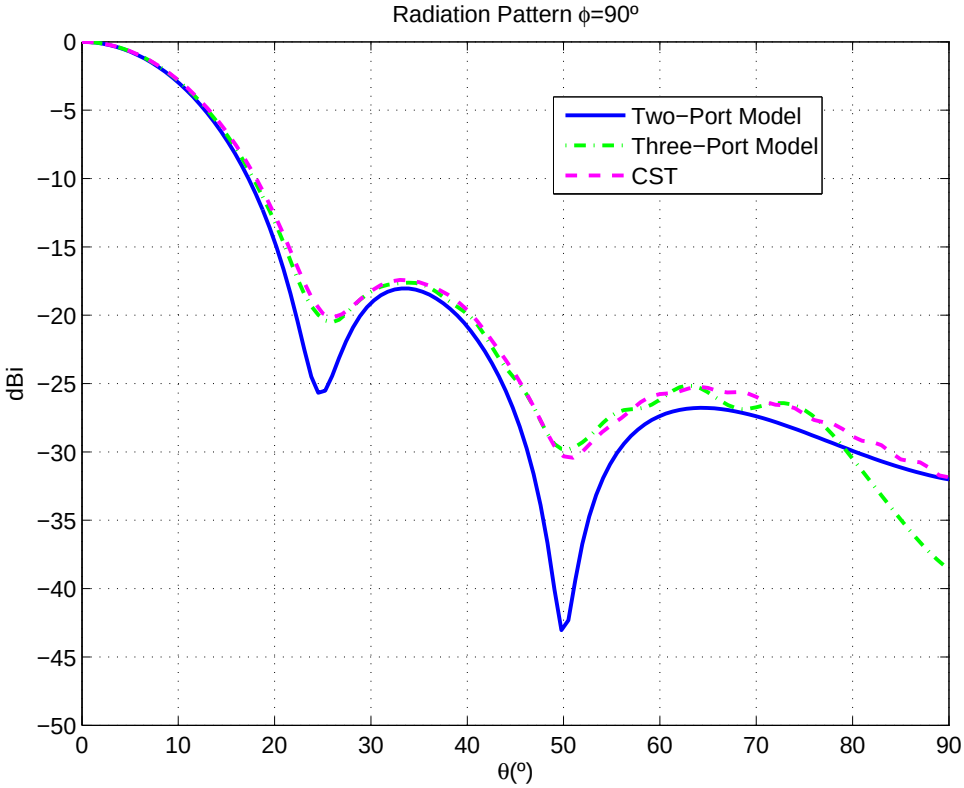

(b) E-Plane ($\phi = 90°$)$D_{0,MM,2P} = 18.42dBi, D_{0,MM,3P} = 18.47dBi, D_{0,CST} = 18.5dBi$

Figure 5.6: Radiation pattern (at $12.5GHz$) of horn C (see Table 5.1) using the two-port and the three-port models, compared against a CST Microwave Studio simulation.

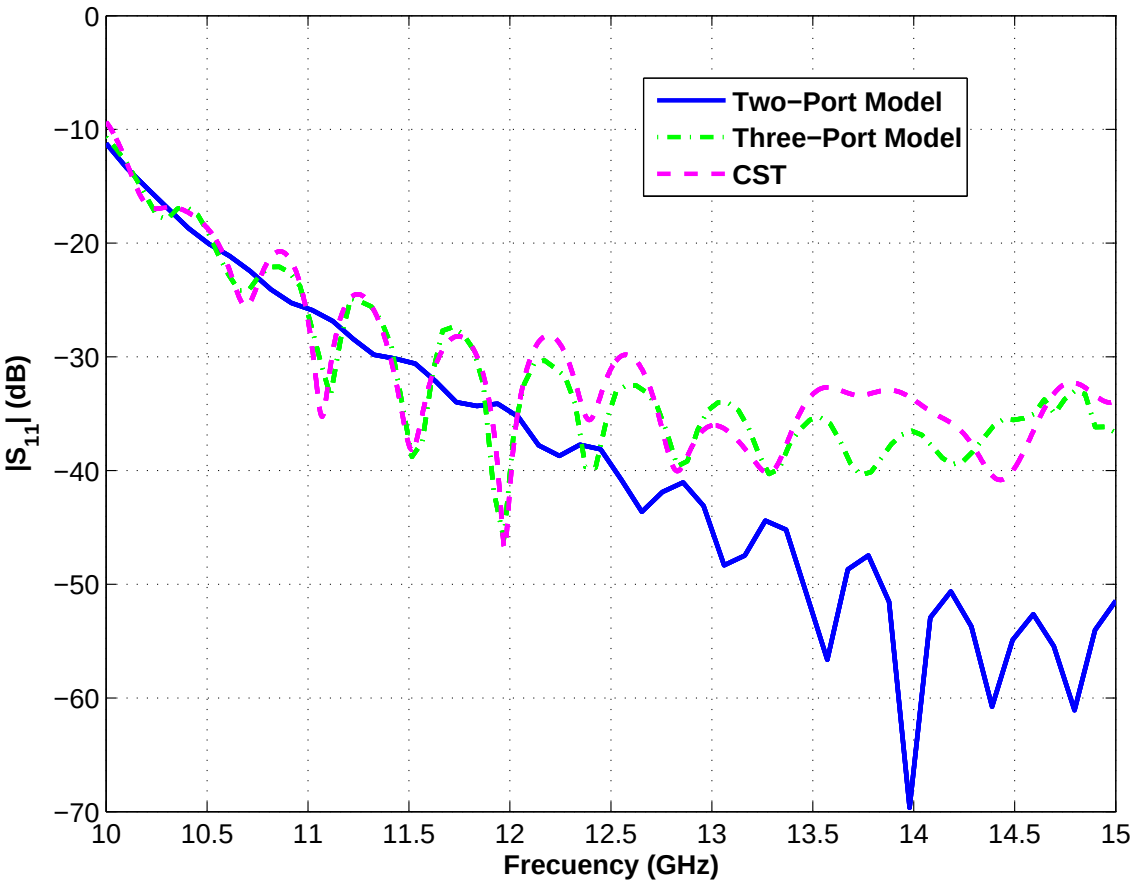

Figure 5.7: Adapation of horn C (see Table 5.1) using the two-port and the three-port models, compared against a CST Microwave Studio simulation.

6

Introduction to Additive Manufacturing: 3D-printing for Standard Waveguides and Horn Antennas

6.1 Motivation

The theoretical models presented in the previous chapters would be of reduced use if they would not relate with the reality. The way to verify this is by constructing and measuring a horn antenna previously simulated using the Mode-Matching technique. This chapter will be focused on the introduction to manufacturing.

Waveguide devices (and therefore also horn antennas) are traditionally constructed by the machining of a piece of metal (typically aluminium). This usually requires sending the design to an external manufacturer and waiting for the prototype to be constructed and sent back to the researchers.

In the recent years additive manufacturing techniques like 3D printing [1] have become very popular in the engineering and scientific communities and since the research group already owned a 3D printer, it was decided to make use of it to construct a horn antenna prototype. A photograph of the printer was shown in Figure 1.2(a).

In this chapter the employed construction process is described as well as the obtained results. It is important to note that all the presented devices have been manufactured locally by the authors of this work using the equipments available at the laboratories of the research group.

6.2 Manufacturing Process

In this section the construction process will be described taking the example of a horn antenna but, as it will be seen in section 6.3, it can be easily applied to manufacture other waveguide devices.

[1] A 3D-printer is an additive manufacturing machine that can construct three-dimensional objects using a molten filament of, typically, plastic.

6.2.1 Creating the 3D Model

After designing the antenna a 3D model of the device is created using a CAD software. In this work CST Microwave Studio was the chosen option since a 3D model had already been created to carry out a simulation of the horn, but any other software could be used. The only requisite is that the model can be exported in a format allowed by the printer software.

When creating the model it is important to add at the input of the horn a transition with the appropriate screw holes that allow to connect the antenna to the previous stage of the RF chain.

6.2.2 Printing and Polishing

The 3D model is printed using the printer specific software. The horn has been printed standing vertically on its input. This has been found to be the best orientation since it minimizes the overhanging angles, which are more difficult to print. In this case, if the flare angle would be very pronounced it could be necessary to add some support to the horn walls while printing. Typically this can be achieved using the printer software.

After printing it is important to remove any plastic residue that the extruder may have left on the piece. The printer available for these trials tended to leave very thin threads of plastic that may significantly impact on the horn performance if not removed.

Finally, as it will be shown in section 6.4 it is also important to verify that the dimensions of the printed antenna are the expected ones. Tolerance errors will have a critical impact on the horn performance, specially the errors in the input waveguide section since they will create a mismatch between the antenna and the previous device. The inner dimensions of the waveguide section as well as screw hole diameters can be checked using a vernier caliper.

6.2.3 Metallization

At this stage the antenna has been constructed using plastic, but as it is known horn antennas need to be constructed using electrical conductor. This means that the printed antenna must be metallized.

Metallization can be achieved by a wide range of procedures like electrolytic metallizing, vacuum metallizing or thermal spraying. Since the main objective of this work was finding a process that would be non expensive, simple and quick, these complex industrial procedures where discarded and the chosen option was to apply a conductive paint on the plastic antenna.

The chosen paint is composed of different acetates that act as a solvent and silver powder. After applying the paint the acetates evaporate leaving the horn coated in silver. To achieve a good conductivity it is important to apply the paint thoroughly, paying special attention to not leave any uncovered areas. It has also been found that applying a second layer of paint significantly improves the obtained conductivity.

6.3 Initial Devices for Testing

The most simple waveguide device that could be constructed is a section of rectangular waveguide. Since they are not resonant devices the mechanical tolerances will have a smaller impact

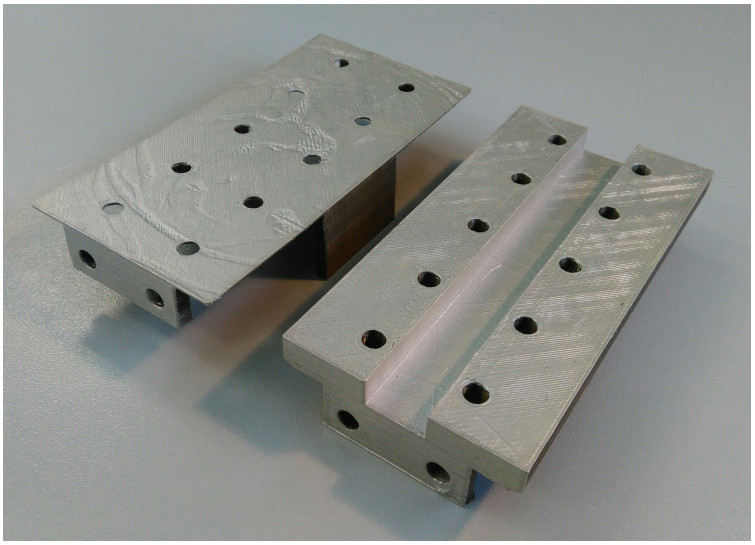

Figure 6.1: Photograph of the 3D printed rectangular waveguide (WR51).

Parameter	Value (mm)
a_{in}	12.954
b_{in}	6.477
a_{out}	51.282
b_{out}	47.691
l_{horn}	114.734
l_{WG}	21.429
$h_{thickness}$	1

Table 6.1: Dimensions of the constructed pyramidal horn.

in its performance. Additionally, as it will be shown in section 6.4, the waveguide section can be used to estimate the electrical conductivity achieved by the metallization process. The constructed waveguide section follows the WR-51 standard [8, 18] which establishes that the width of the waveguide should be $12.954mm$ and the height should be $6.477mm$. A photograph of the constructed device can be found in Figure 6.1.

Additionally, a pyramidal horn antenna has been built to demonstrate not only the described manufacturing process but also to have a reference model for comparing the results provided by the Mode-Matching software. The dimensions of the antenna can be found in Table 6.1. A picture of the final horn is shown in Figure 6.2 on the following page.

6.4 Experimental Results

All the steps involved in the fabrication of these experimental devices (already described in section 6.2) have been carried out by the author of this work. The measurements have also been performed locally using the equipments available at the Escuela Politécnica Superior EPS-UAM and research group laboratories (a photograph illustrating the measurement process was previously shown in Figure 1.3).

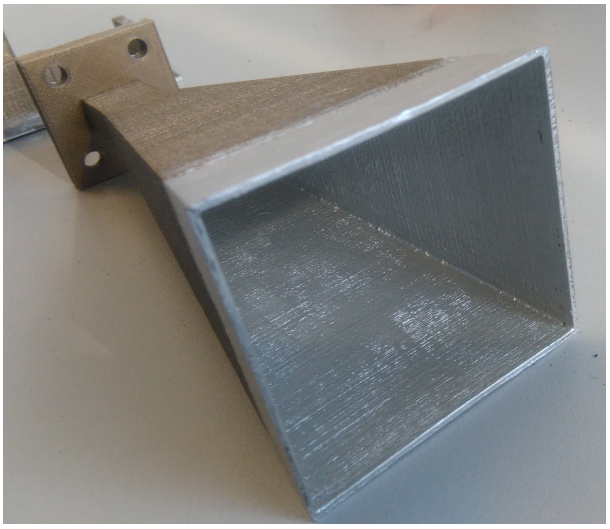

Figure 6.2: Photograph of the 3D printed antenna after the metallization process.

6.4.1 Rectangular Waveguide

The measured scattering parameters of the rectangular waveguide have been compared with a CST Microwave Studio simulation. To estimate the conductivity of the paint layer an iterative process was followed. Several simulations were carried out using conductor models with different conductivity values and the simulated scattering parameters were compared against the measured parameters. As a result, the electric conductivity achieved by the metallization process was estimated in $\sigma = 15000^{S}/_{m}$

In Figure 6.3 the scattering parameters of the conventional waveguide are represented. It can be seen that there is a good agreement between the simulated and measured values.

It is known that to achieve a good performance in a waveguide composed by different parts joined by screws, it is important that the different parts are properly tightened together to avoid the power losses caused by the surface currents propagating outside of the waveguide. To ensure this a number of screws sufficiently high must be used along the waveguide section.

Therefore, during the measurement process an interesting experiment was carried out: the rectangular waveguide was measured making use of 2, 3 and 5 of the present screw hole pairs. In Figure 6.3 can be seen that indeed the number of used screws has a significant impact on the achieved performance. The value of the transmission parameter corresponding with a conductivity of $\sigma = 15000S/m$ is achieved only when all of the screws are used. Indeed, pulling the cover of the conventional waveguide while it was connected to the network analyser produced perturbations on the measurement.

6.4.2 Horn Antenna

The resulting antenna has been measured in the anechoic chamber [2] of the Escuela Politécnica Superior, Universidad Autónoma de Madrid (see Figure 6.4). The measured radiation pattern

[2] An anechoic chamber is a room designed to absorb waves (either sound or electromagnetic waves) produced by any source inside of it and that is also isolated from external noises. In this case, an electromagnetic anechoic chamber was used.

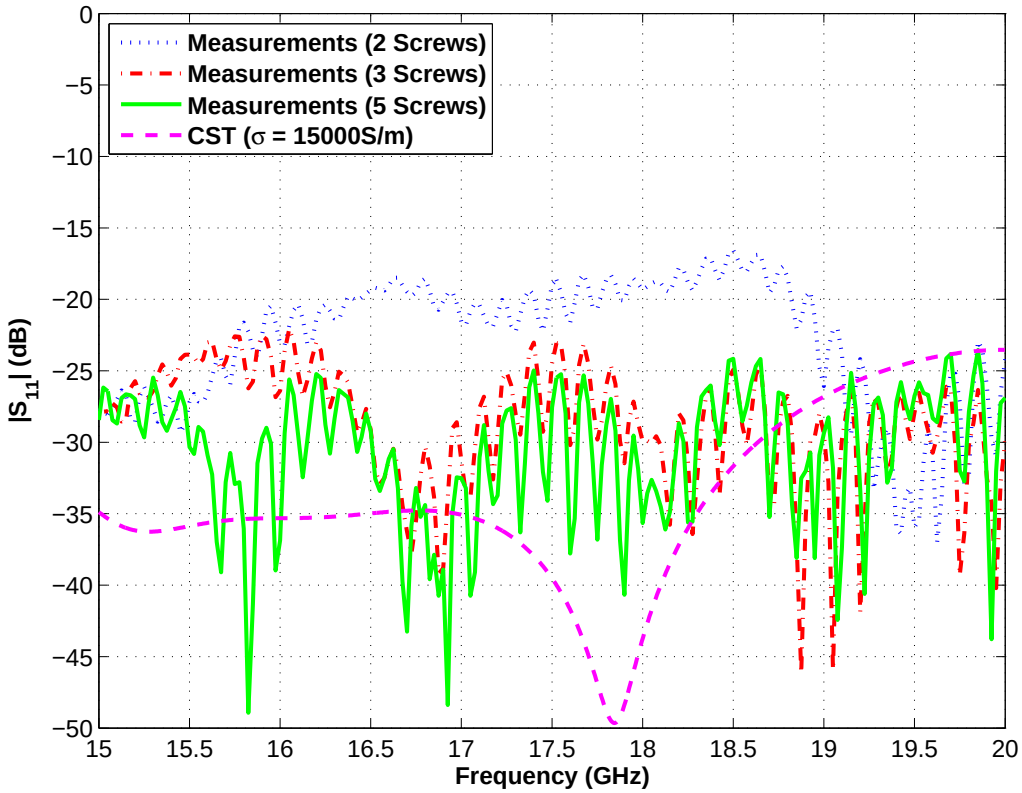

(a) Reflection

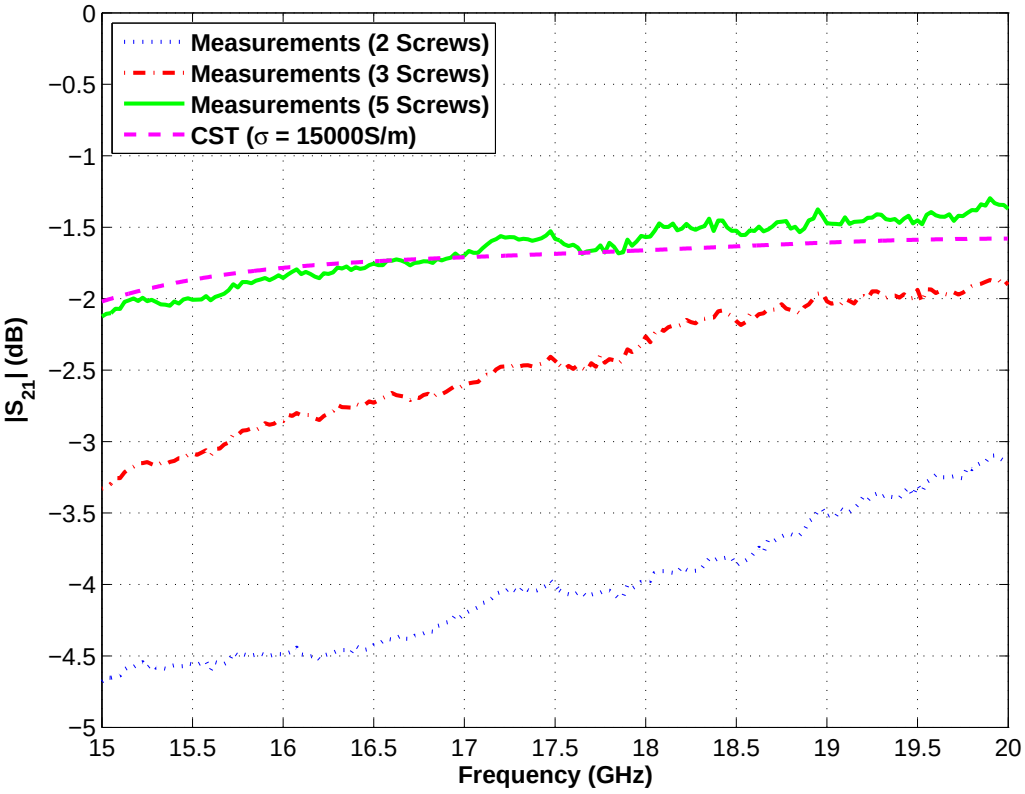

(b) Transmission

Figure 6.3: Module of the reflection and transmission parameters of the printed rectangular waveguide, compared against a CST simulation.

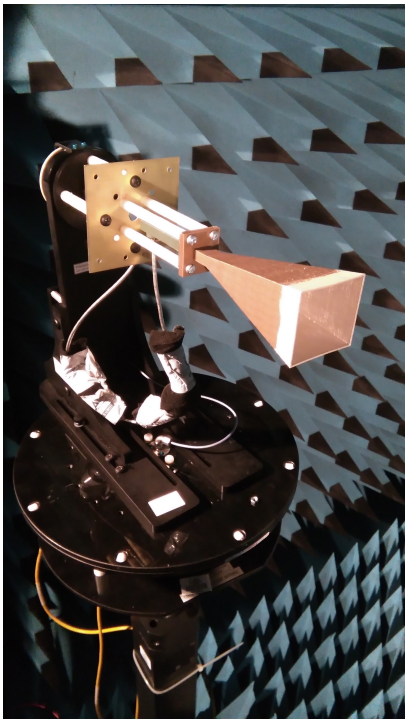

Figure 6.4: Photograph of the 3D printed pyramidal horn mounted at the anecoic chamber.

is represented in Figure 6.5 on the next page, the reflection coefficient in Figure 6.6 and the directivity in Figure 6.7.

The measurements are compared against the same parameters obtained by different simulation methods, the implemented Mode-Matching software and the commercial tool CST Microwave Studio. It can be seen that the radiation pattern matches the simulation values with great accuracy, specially considering that the simulations considered an antenna constructed of Perfect Electric Conductor (PEC) but the silver paint does not have infinite conductivity.

On the other hand, the return loss level corresponds more or less with the expected values but the resonances have been shifted. This mismatch was studied and it was found out that this displacement is caused, as it was advanced earlier, by construction tolerances. The inner dimension of the horn input were measured with a caliper and it was found that they were slightly smaller (around a 2.5%) than the design value.

To verify if this was the cause of the problem a second simulation was performed where the model dimensions corresponded with the real ones of the constructed antenna. The reflection coefficient values of this second simulation can be found in Figure 6.8 on page 53 and it can be seen that the resonances match more accurately.

It has been observed that the error introduced by the 3D printer is systematic and therefore when creating the 3D model to print this effect can be compensated by applying a correction factor to the antenna dimensions.

Finally, note that the measured gain values at different frequencies show a response similar to the simulated directivity values but around $1dB$ lower. This difference can be explained because the simulations considered a PEC antenna while the prototype is constructed using a lossy conductor.

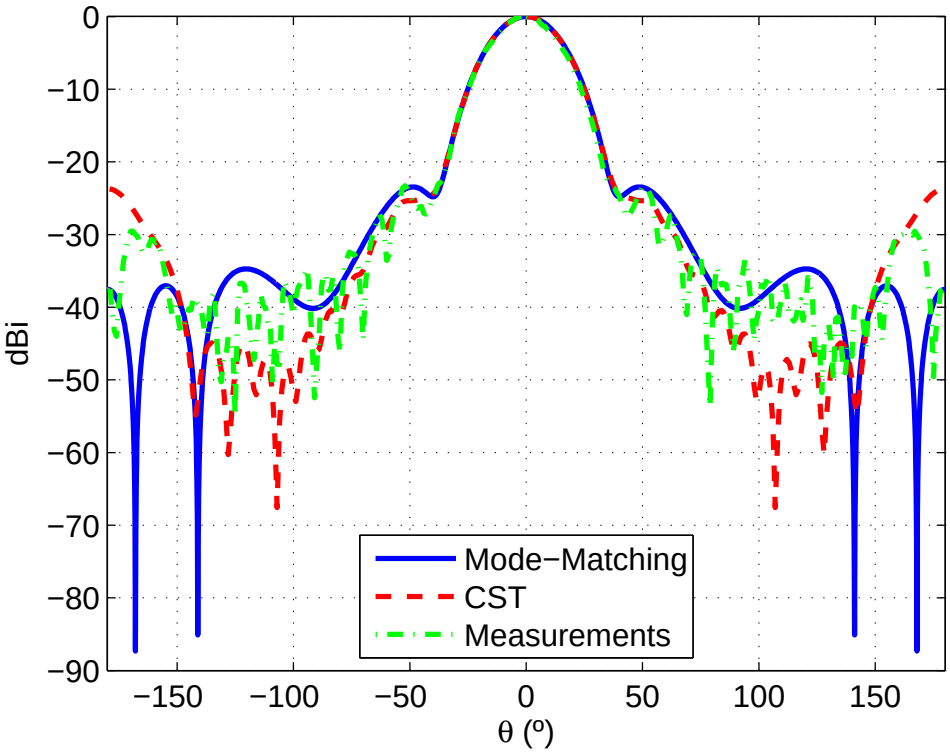

(a) H-Plane ($\phi = 0°$)

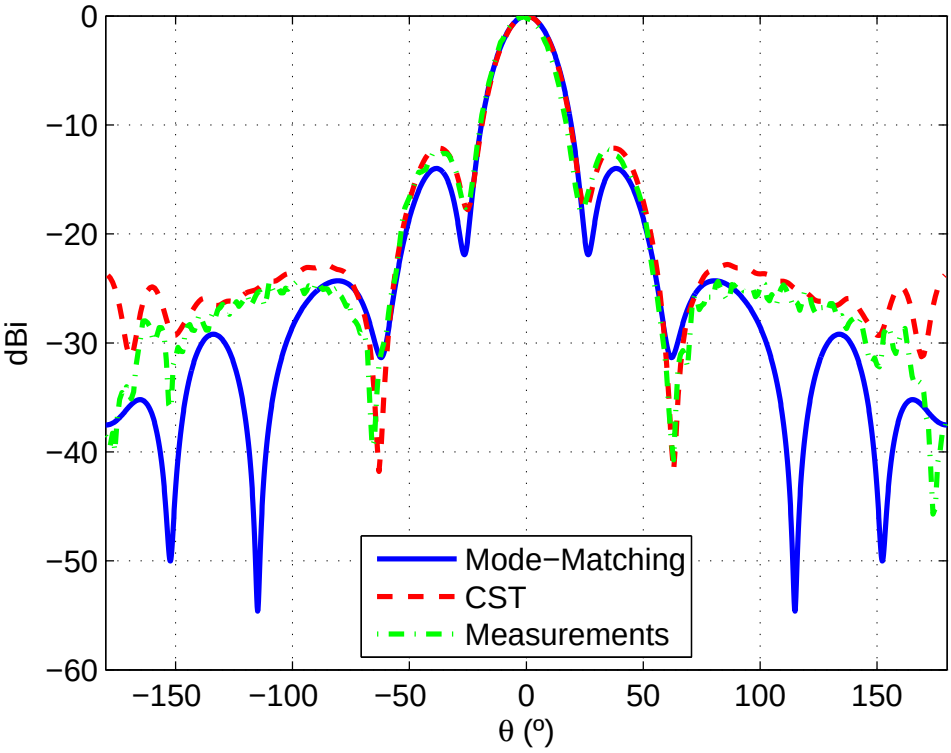

(b) E-Plane ($\phi = 90°$)

Figure 6.5: Radiation pattern (at $14GHz$) of the 3D printed pyramidal horn. The measurements are compared against different simulation tools.

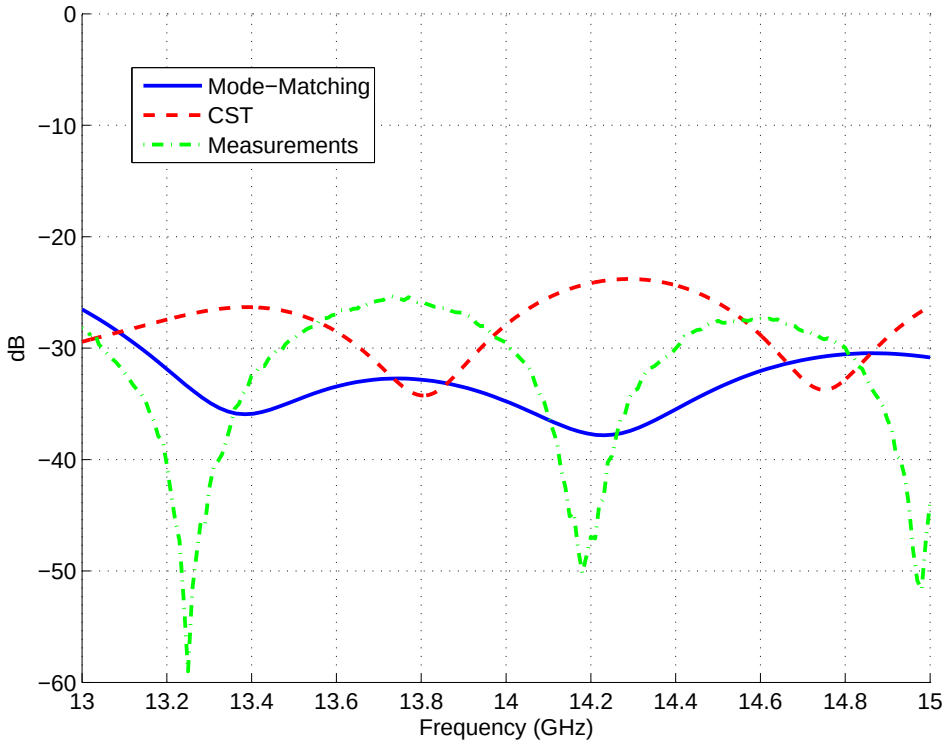

Figure 6.6: Reflection coefficient of the constructed antenna. The measurements are compared against different simulation tools.

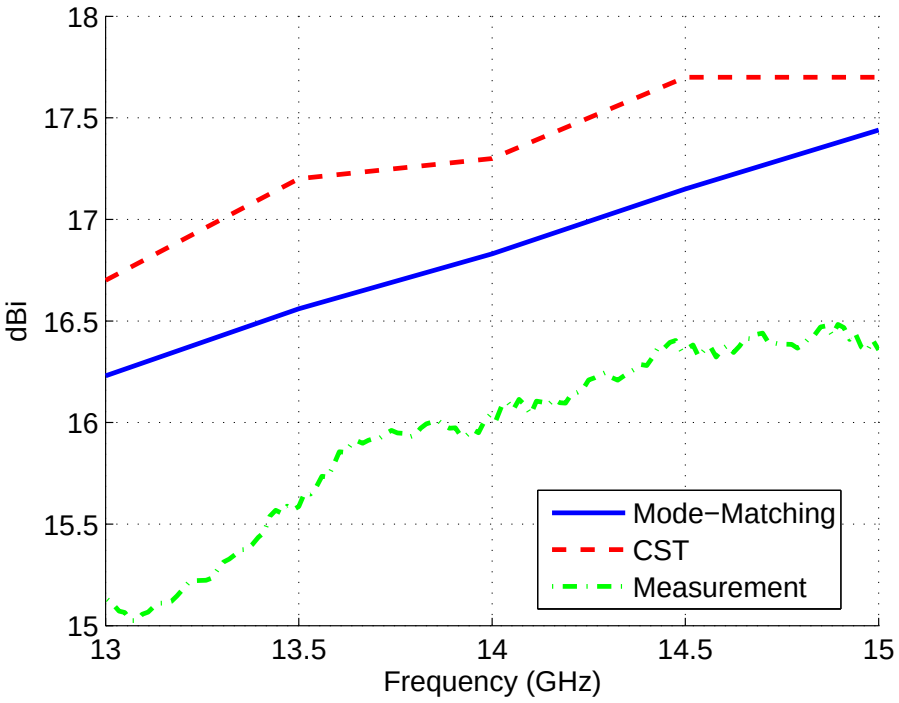

Figure 6.7: Directivity (Mode-Matching and CST) and directive gain (Measurement) of the pyramidal horn at different frequencies.

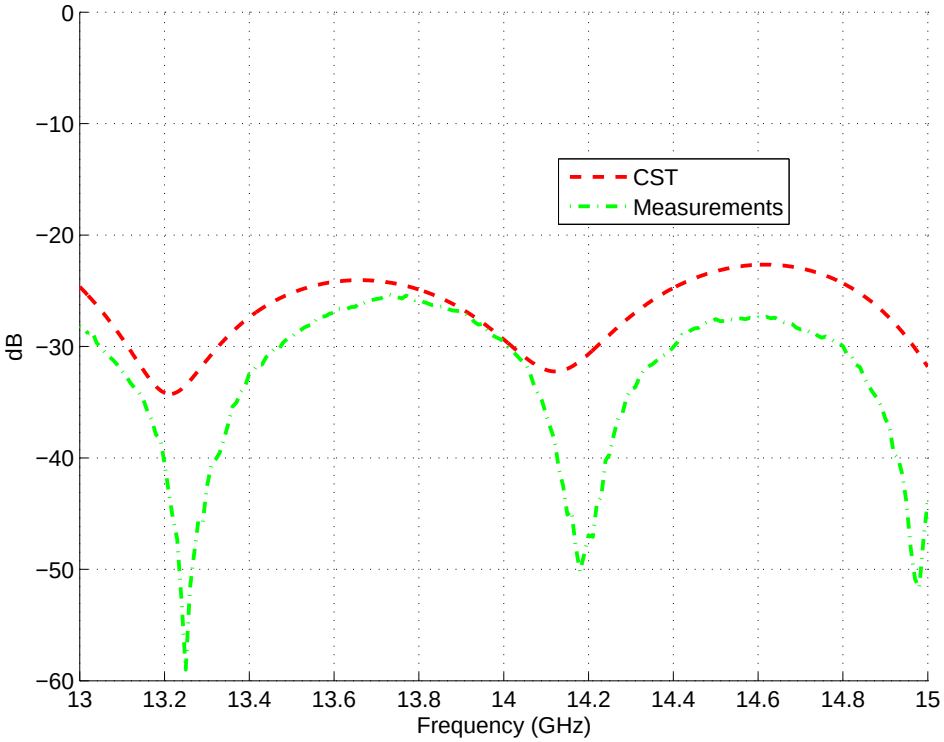

Figure 6.8: Measured reflection coefficient of the antenna compared against a simulation with a tolerance corrected model.

6.5 Conclusions

In this chapter a low cost construction method for waveguide devices has been presented. The process involves creating the body of the device using a 3D printer and then metallizing it using a silver based paint.

To demonstrate the usefulness of the process two different devices were manufactured and measured, a straight section of rectangular waveguide and a pyramidal horn antenna. The obtained parameters matched with great accuracy the simulation models (always that construction tolerances had been considered).

This construction process could be easily extended to other waveguide devices like filters or couplers. In the next chapter, more advanced devices that have been constructed following this process are presented.

7

Other Advanced 3D Printed Devices

7.1 Motivation

In the previous chapter a process for constructing waveguide devices using a 3D printer was described. There it was advanced that this process could be extended to more complex waveguide devices.

As a final step of this work an "advanced" version of each of the constructed devices has been fabricated to demonstrate that the described process is actually applicable to more sophisticated devices.

First, a gap waveguide [19, 20] was manufactured as an advanced version of the rectangular waveguide section. Additionally a comparison between the two types of waveguides has been carried out.

And second, to follow the main line of the work focused on horn antennas, a choke horn [3, 21] has been constructed. This type of antenna has a profile that will make the 3D-printing process harder than in the case of the pyramidal horn.

It is important to emphasize that the full-wave characterization of these horn antennas (that in the previous chapter, as well as the choke-horn in this chapter) has also been carried out with the modelling software developed in this work, combining the two aspects of this project: advanced electromagnetic simulation with innovative recent manufacturing techniques.

7.2 Gap Waveguide

7.2.1 Introduction

The gap waveguide is a patented technology [19, 22] for the construction of microwave devices in the frequency range of $30GHz$ to the Terahertz frequencies. The goal of this technology is to overcome that the conventional manufacturing technologies are no suitable for that frequency band since planar technologies like microstrip or substrate integrated waveguides (SIW) present

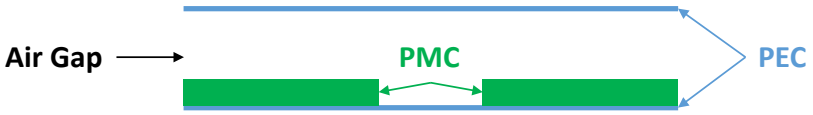

Figure 7.1: Schematic representation of the cross section of a gap waveguide.

high power loss values (that grow with the frequency) and hollow metallic waveguides have the problem of assuring good contact in the metallic joints [19].

A representation of the cross section of a gap waveguide can be found in Figure 7.1. It can be seen that it is composed by two parallel PEC surfaces separated by a certain air gap. One of the surfaces is covered by a structure simulating a PMC, leaving a narrow region of PEC surface without covering. The electromagnetic wave propagates between the two conducting plates and is guided laterally by the PMC. It has been stated previously in this work that magnetic conductors do not exist in nature, anyway it has been shown in Chapter 5 that they can be theoretically defined. Even if they are not present in nature, certain materials can be artificially modified in some ways so they emulate a magnetic conductor under certain conditions. These are known as metamaterials and their study falls well beyond the scope of this work. Anyway for the present case study it is sufficient to know that the PMC boundary is achieved by a "bed of nails" that can be seen in the photograph of Figure 7.3 [19].

This post pattern has several parameters (like their width, height or spacing) that must be selected when designing a gap waveguide device. As it is shown in [20] small changes in these parameters have a significant impact in the behaviour of the device and therefore the construction of a gap waveguide constitutes a good test to check if the 3D printing technology is precise enough to manufacture waveguide devices more sophisticated than a hollow rectangular waveguide.

7.2.2 Experimental Device

An schematic representation of the built waveguide can be found in Figure 7.2 on the next page. There the fundamental parameters of the design are presented and their values can be found in Table 7.1. That table also contains some parameters that are not represented in Figure 7.2: b is the height of the waveguide, p_h is the height of the pins and h is the gap between the top of the pins and the upper plate.

This values have been selected following the recommendations and results presented in [20], which have been adapted to manufacture a gap waveguide with a transition to a WR51 standard waveguide [18]. The reason for this is that the measurement equipment available at the laboratory required that the device had WR51 ports. A representation of the final constructed device can be found in Figure 7.3 on page 58.

7.2.3 Measurements and Evaluation

The measured scattering parameters of the device have been compared with a CST Microwave Studio simulation. The conductivity value used in the simulation is the same that was estimated in Chapter 6. In Figure 7.4 the scattering parameters of the gap waveguide are represented. It can be seen that there is a good agreement between the simulated and measured values.

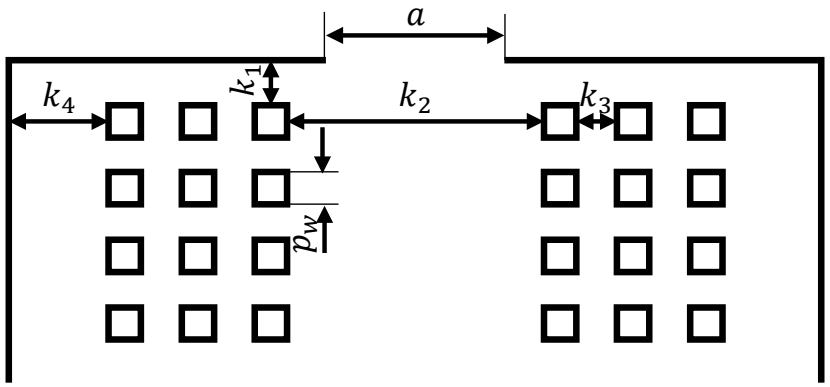

Figure 7.2: Schematic representation of the constructed gap waveguide where some of the fundamental parameters are illustrated.

Parameter	Value (mm)
k_1	$k_3/2$
k_2	b
k_3	3.5
k_4	5.0
p_w	3.0
p_h	5.477
a	12.954
b	6.477
h	1.0

Table 7.1: Dimensions of the gap waveguide.

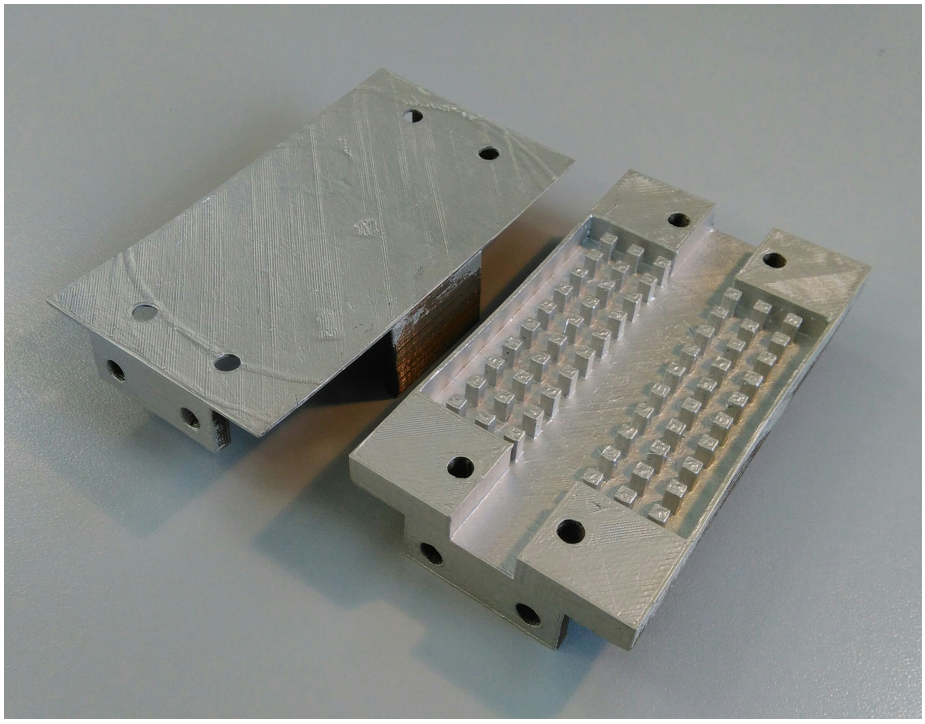

Figure 7.3: Photograph of the 3D printed gap waveguide (with WR51 transitions at both ports).

As it was advanced above there exists a certain discussion about how achieving the best performance in waveguiding systems at millimetre-wave bands and above. Gap waveguide users reason that, since hollow waveguides are hard to manufacture in just one metal piece at frequencies higher than $30GHz$ [19], they are usually not very cost-efficient because of the high number of screws needed to ensure a good metallic contact between the different pieces that constitute the device and avoid power losses caused by the surface currents flowing outside of the waveguide. Since gap waveguides are not as affected by this effect as hollow waveguides (as it is shown in [19]) the number of screws (and screw drills) could be reduced, helping to tighten the construction budget. On the other hand, gap waveguide suffers that the mechanization of the bed of nails[1] may produce an overrun that equals with the cost of introducing more screws in a hollow waveguide design.

Therefore, during the measurement process an interesting experiment was carried out: the hollow waveguide was measured making use of 2, 3 and 5 of the present screw hole pairs. In Chapter 6 was seen that the number of used screws has a significant impact on the achieved performance. The scattering parameters of both devices have been compared as it is shown in Figure 7.5 and it can be seen that the hollow waveguide can only match the performance of the gap waveguide when all of the screws are used.

This may lead to think that the gap waveguide is the best alternative since by reducing the number of screws, with respect to the conventional waveguide, the cost of the device could be reduced. Nevertheless this statement is leaving out some important facts:

- Since the construction technology is based on 3D printing, the cost of making a screw hole is negligible (there is not need to drill a piece of metal) and therefore the only cost

[1] The posts at both sides of the gap waveguide.

on adding a new screw to the design is the cost of the screw itself.

- The gap waveguide is bigger and has a shape more complex than the conventional waveguide. This two facts lead to a greater paint consumption during the metallization process (manually painting each of the posts wastes a lot of paint). Given that the paint is made of silver this can have a significant impact on the cost of the device.

Therefore, there is not a clear conclusion on which device performs better. Gap waveguides may be of special interest under certain conditions when the structure of the device or the application requirements do not allow to insert an elevated number of screws and very low losses are required. On the other hand, conventional waveguides are a well established technology and there is a great know-how on the design of these devices.

7.3 Choke Horn

7.3.1 Introduction

Choke horns are a special type of horn antenna that, unlike other horn antennas, have low directivity values. They are used in applications where the robustness and power handling capacity of horn antennas are required but also a radiation pattern with a wide beamwidth (even omnidirectional in some cases) is desired.

Since these antennas are specially well simulated using the method of moments [21] and since the implemented Mode-Matching software gave very good results for conventional horns, it seemed a good idea trying to create a prototype choke horn simulation tool based on the already developed Mode-Matching software. This first prototype modifies the three port model and places a short circuit at the coaxial port. This creates a two port model with a topology similar to the one presented in 7.6. The main limitations of this prototype is that it can only simulate choke horns with just one ring around the aperture and that, as it happens with the two-port model for horn antennas, the lateral radiation will not be modelled accurately. The later can be a serious issue since, as it was said earlier, these antennas do no present high directivity values. Nevertheless, this was just a proof of concept with the intention of checking out possible future work areas.

Constructing a horn antenna will therefore provide with real world measurements that will be used to verify the validity of the simulation software. Additionally it will serve the purpose of extending the construction process based on 3D printing to a different device that is somehow harder to construct than the basic pyramidal horn since, at it can be seen in Figure 7.8 the ring that surrounds the antenna aperture constitutes a big overhang that will require special treatment.

7.3.2 Experimental Device

The constructed choke horn is a very simple feed presented in [23]. This antenna was selected since its profile was simple enough to be simulated using the aforementioned prototype tool.

A circular to rectangular waveguide transformer had to be designed and added at the antenna input in order to allow the measure of the constructed device since all the coaxial to waveguide transitions available at the laboratory corresponded with rectangular waveguides. A representation of this antenna (without the transition) can be found in Figure 7.6 on page 62.

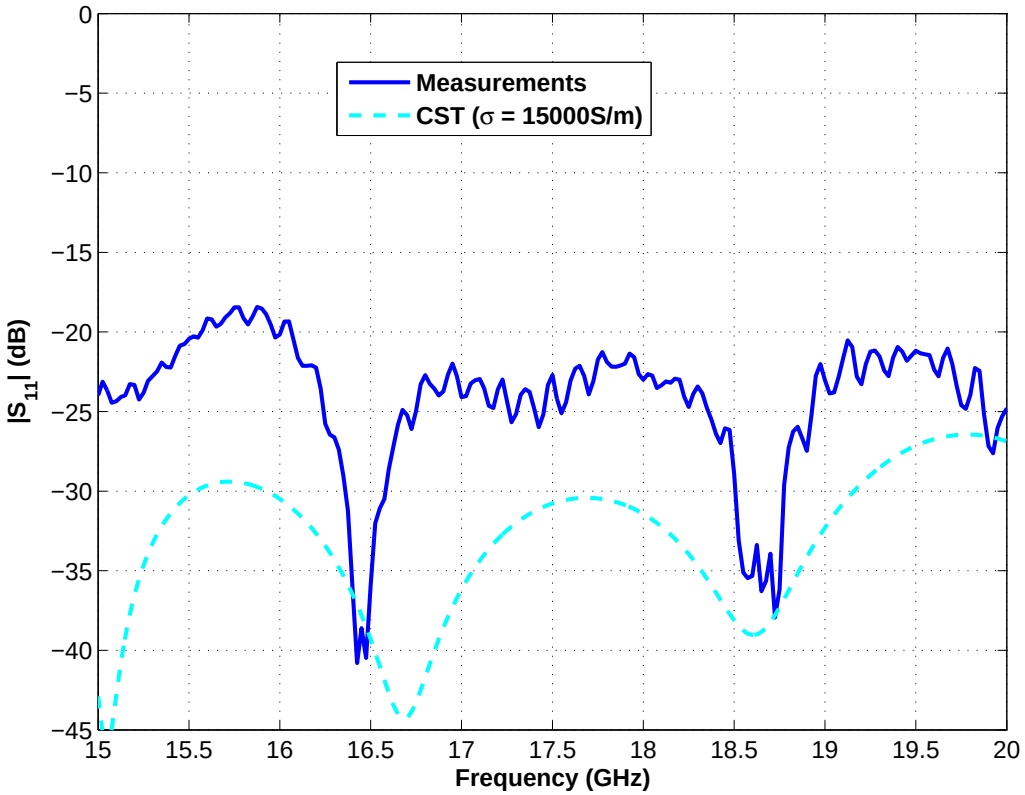

(a) Reflection

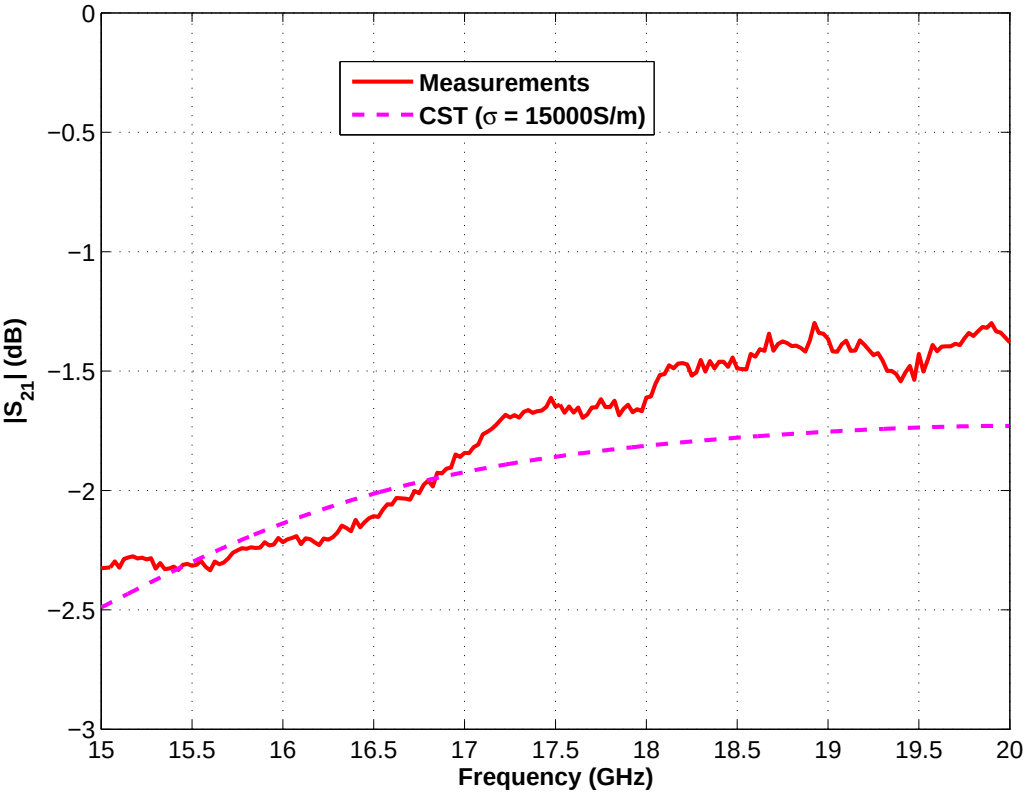

(b) Transmission

Figure 7.4: Module of the reflection and transmission parameters of the printed Gap waveguide, compared against a CST simulation.

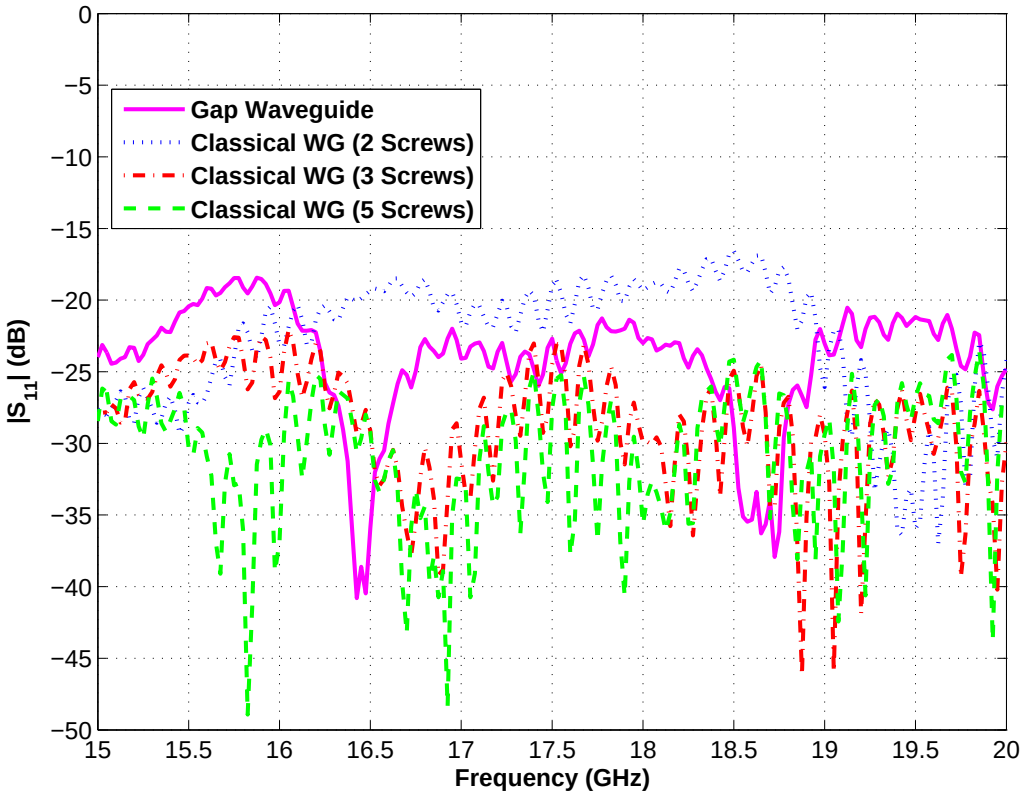

(a) Reflection

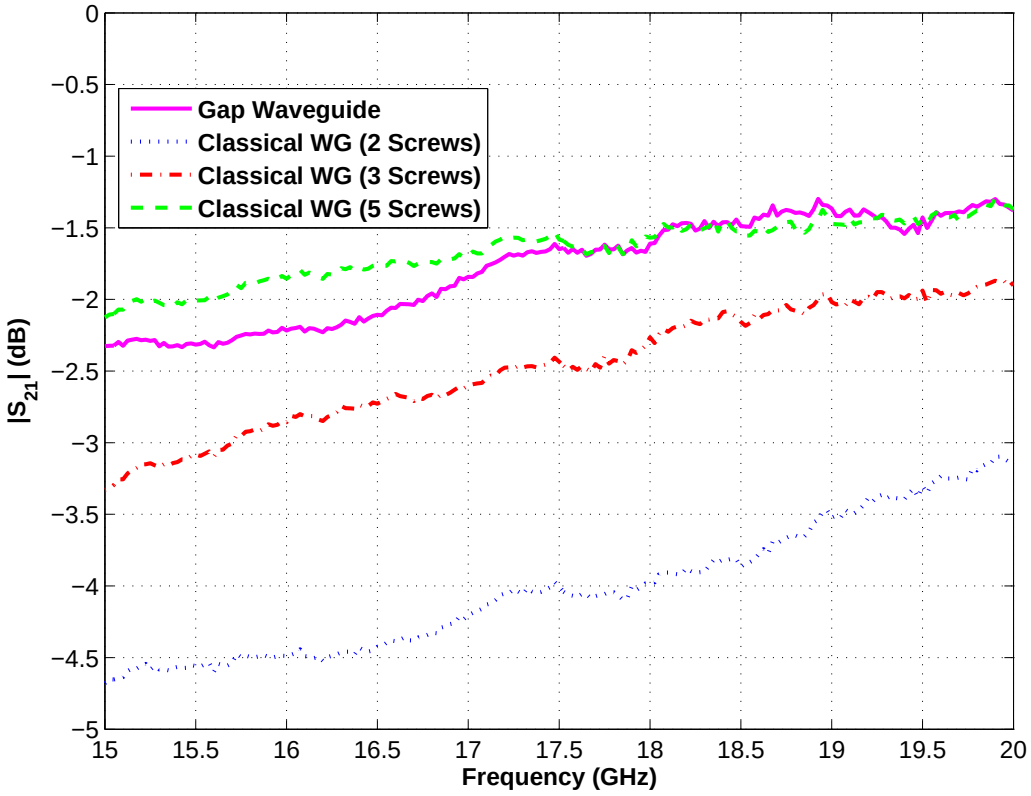

(b) Transmission

Figure 7.5: Module of the reflection and transmission parameters of the printed rectangular waveguide, compared against a CST simulation.

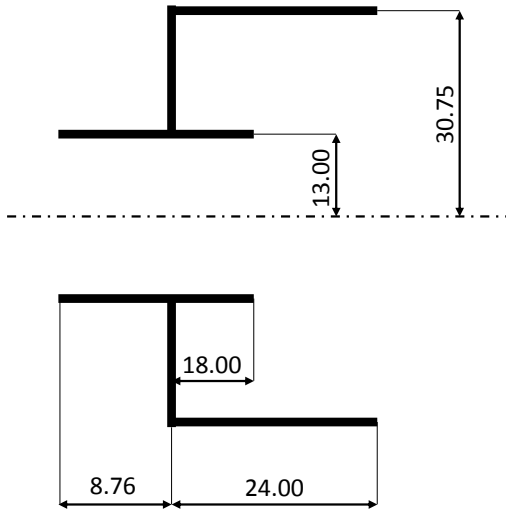

Figure 7.6: Schematic representation of the constructed choke horn [23]. All dimensions are in millimetres.

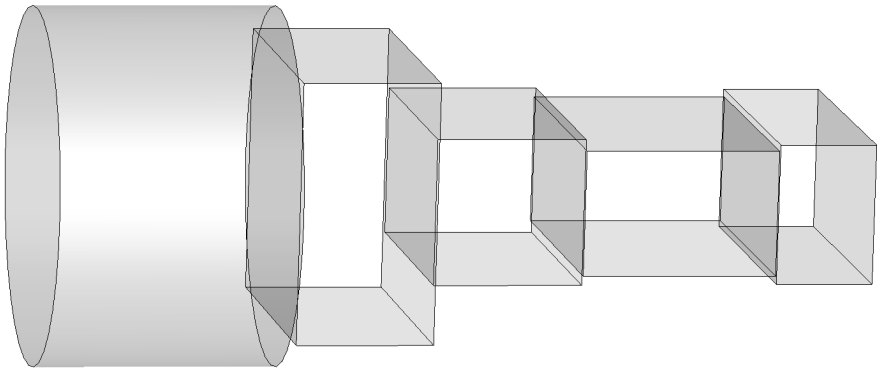

Figure 7.7: Representation of the rectangular (WR90) to circular waveguide adapter added at the input of the choke horn. Dimensions can be found at the Table 7.2.

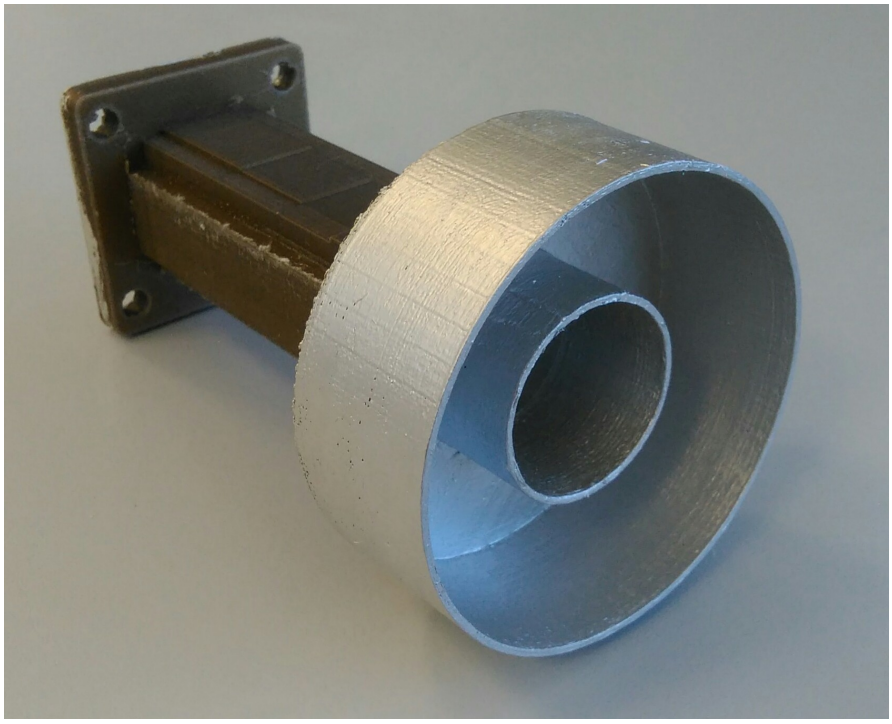

Figure 7.8: Photograph of the 3D printed choke horn (with circular to WR90 adapter).

	Width	Height	Length
WR90	22.86	10.16	27.76
Section 1	22.05	9.12	14.03
Section 2	21.06	10.63	10.79
Section 3	22.71	19.04	9.98

Table 7.2: Dimensions of the WR90 to circular waveguide adapter designed for the choke horn (All values are in millimetres).

The designed transition consists of three waveguide sections that adapt from the WR90 standard waveguide to the circular waveguide used by the choke horn. The dimensions of each section can be found in Table 7.2. In Figure 7.7 a representation of this adapter can be found and a photograph of the constructed antenna is shown in Figure 7.8.

A simulation of the adapter was carried out using different simulators (the Mode-Matching tool and CST Microwave Studio). The results can be found in Figure 7.9, which shows a good agreement between both simulation techniques. Note that port 1 corresponds with the rectangular waveguide and port 2 with the circular.

7.3.3 Measurements and Evaluation

This choke horn was measured using the same procedures employed for the pyramidal horn of chapter 6 and they have been compared against two different simulations, one of them carried out using CST Microwave Studio and the other using the Mode-Matching tool developed for this work.

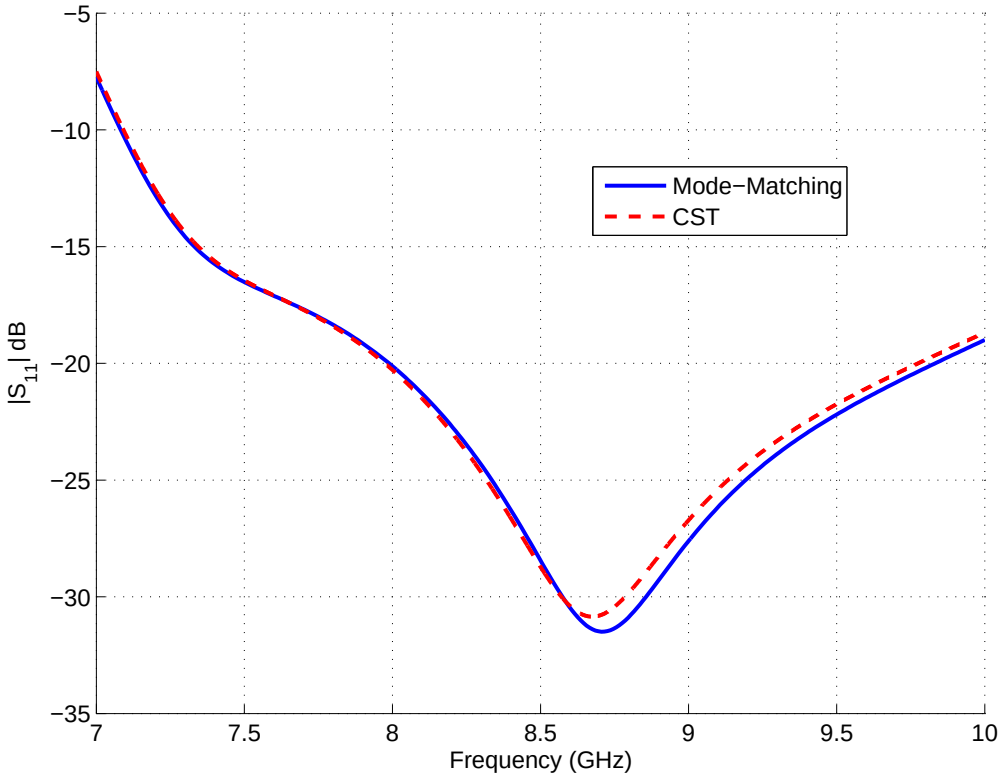

(a) $|S_{11}|$

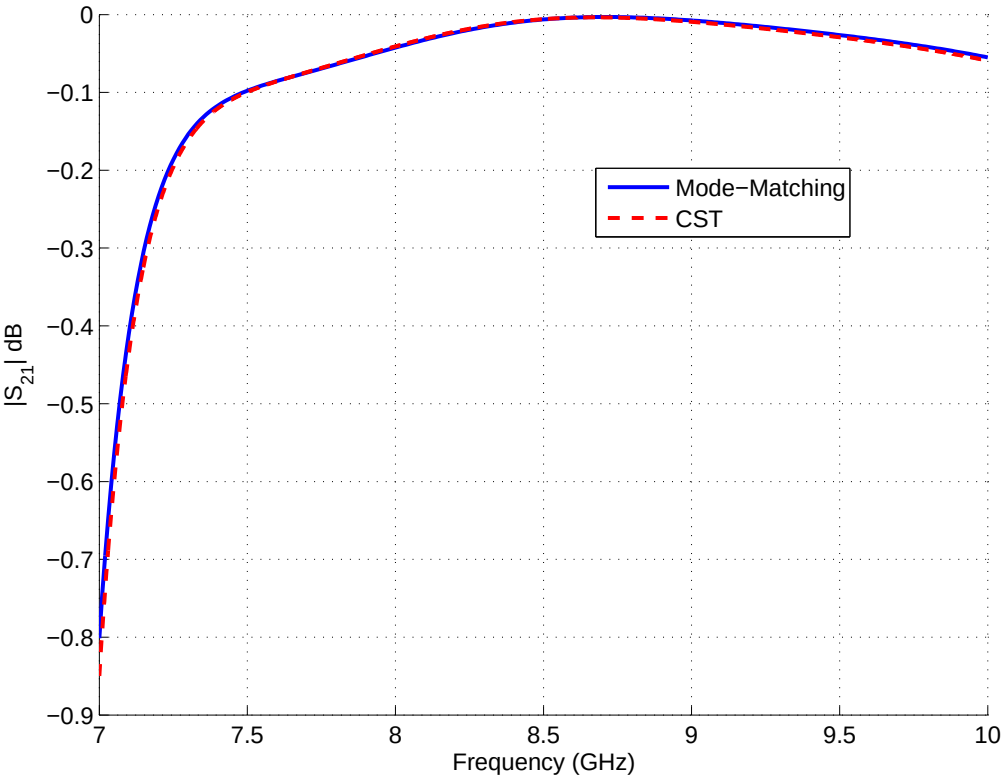

(b) $|S_{21}|$

Figure 7.9: Module of the scattering parameters of the rectangular to circular waveguide transformer added at the input of the horn antenna. The device is simulated using the developed Mode-Matching software and a commercial tool (CST Microwave Studio).

The obtained radiation pattern is represented in Figure 7.10 on the next page, the S_{11} parameter in Figure 7.11 on page 67 and the directivity in Figure 7.12. It can be seen that the measured values match the simulated ones with great accuracy, specially for the simulation with the commercial tool. It is important to note that in this case the simulations considered an antenna made of perfect electric conductor.

The reason that the simulation with the commercial tool is achieving better results than the Mode-Matching approach (specially for the S_{11} parameter) lies on the employed topology. As it was advanced in section 7.3.1 the software prototype for choke horn analysis is based on the three-port topology for conventional horn antenna simulation, where the outer waveguide corresponds in this case with the outer ring of the choke. Therefore this approach leads again to a two-port model, with all the limitations associated to this kind of topologies that were already described in Chapter 4. Since the choke horn under study does no have a big directivity value (indeed its directivity is around $7dBi$) it presents a lot of lateral radiation that is not being modelled correctly. Future work will include an improved model for this case, specially for the return loss, since the radiation pattern is well predicted.

Anyway, this work serves as a first validation of the choke horn simulation using the Mode-Matching technique. The obtained results are very promising and therefore they open a new work line towards the development of a Mode-Matching tool for choke horn simulation. More sophisticated profiles shall be considered (having several concentric rings at the aperture) and a three-port topology similar to the one presented in Chapter 5 could be adopted to overcome the problem of the lateral radiation.

7.4 Conclusions

In this chapter the construction process created for the fabrication of waveguides and horn antennas has been extended to more sophisticated devices. A gap waveguide and a choke horn have been constructed and measured. Additionally, the prototype of a software tool for choke horn simulation has been developed.

The measured parameters have been compared with simulation models of the devices obtaining a good match and therefore this chapter opens a promising line of future work. Following these steps several devices that were being constructed by a specialized manufacturer can now be constructed locally at the university laboratories.

In addition to the research perspective, this will also help to improve the quality of the teaching in the areas of microwave engineering since from now on several devices that were only designed and simulated by the students (as part of their practical training) can also be constructed and measured.

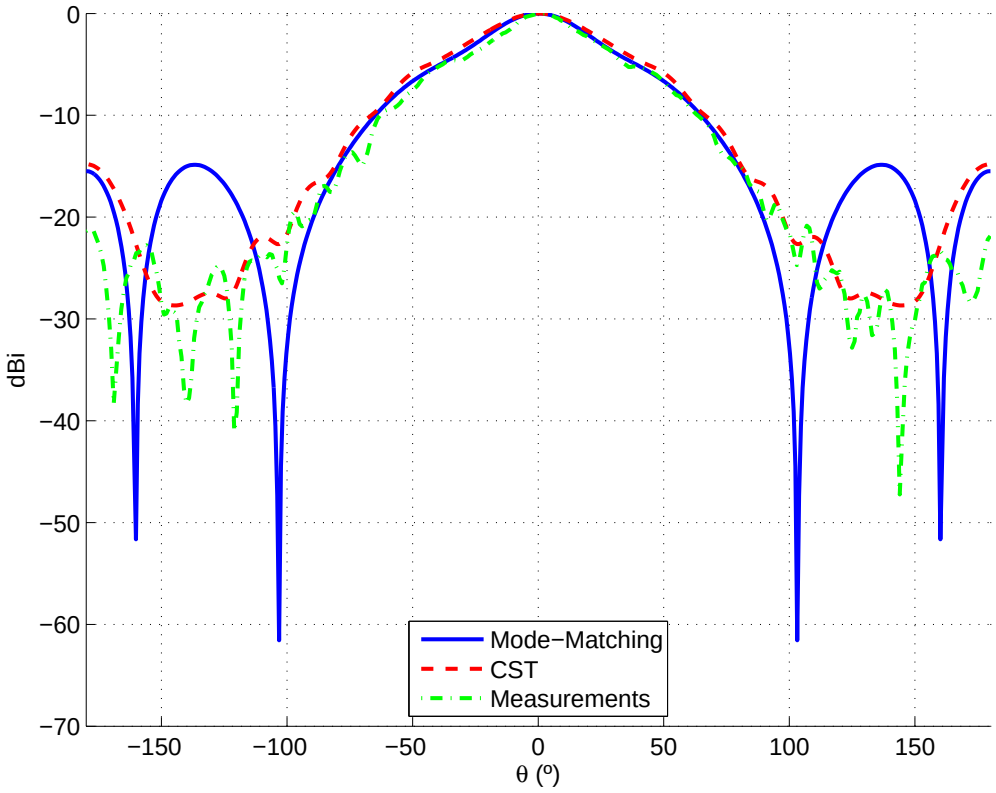

(a) H-Plane ($\phi = 0°$)

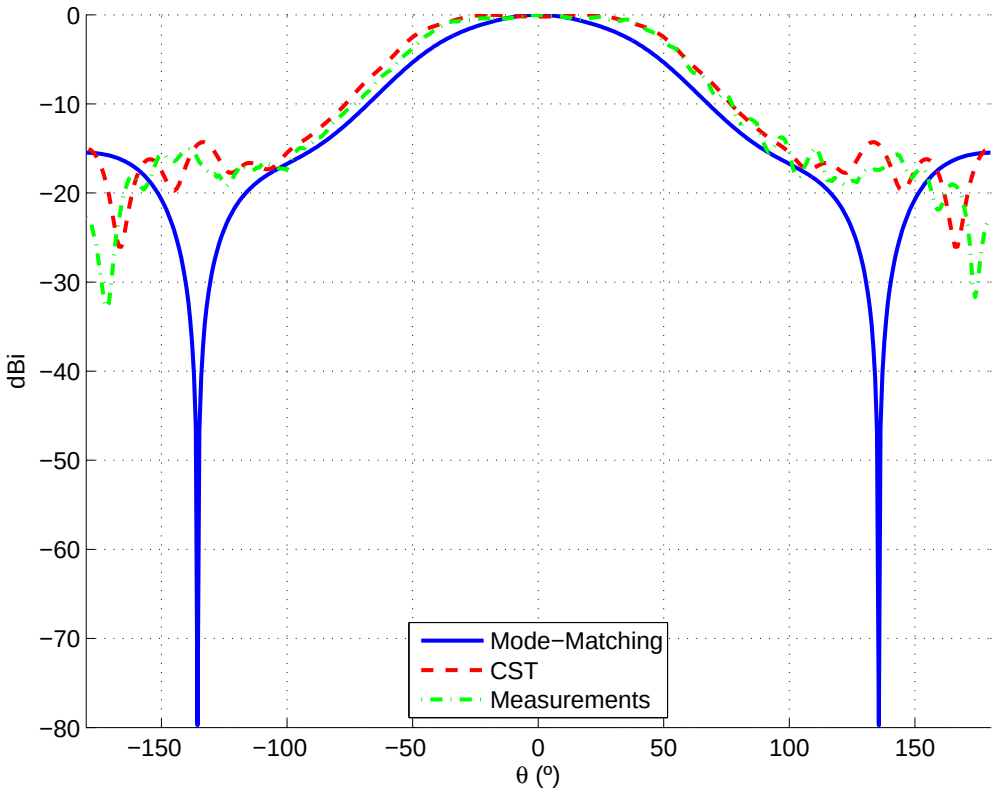

(b) E-Plane ($\phi = 90°$)

Figure 7.10: Radiation pattern (at $8.5GHz$) of the 3D printed choke horn. The measurements are compared against different simulation tools.

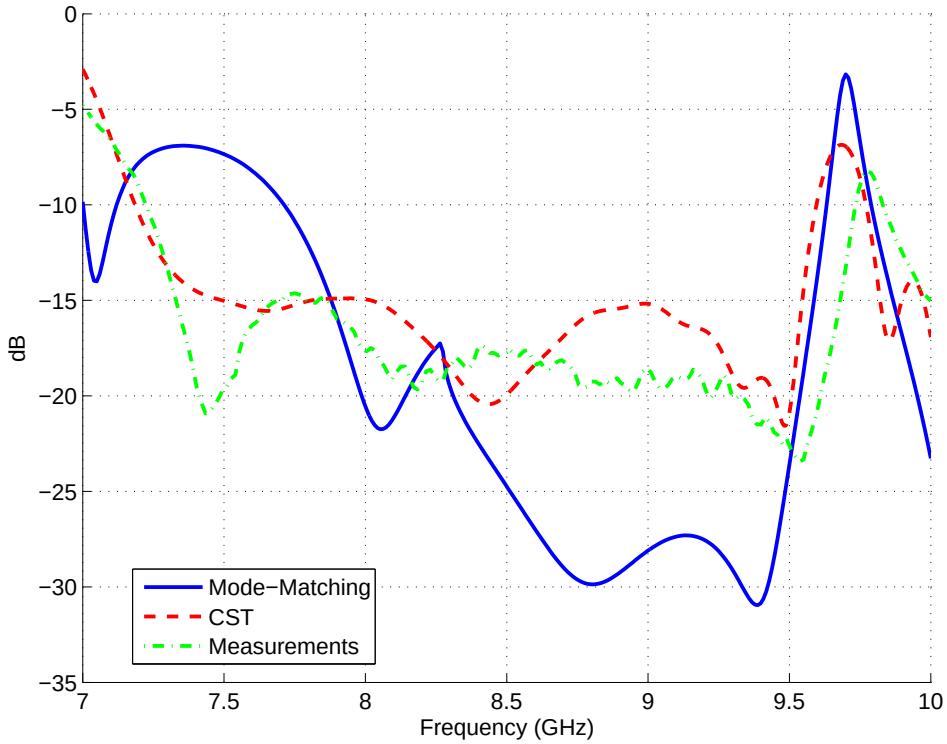

Figure 7.11: Reflection coefficient of the constructed choke horn. The measurements are compared against different simulation tools.

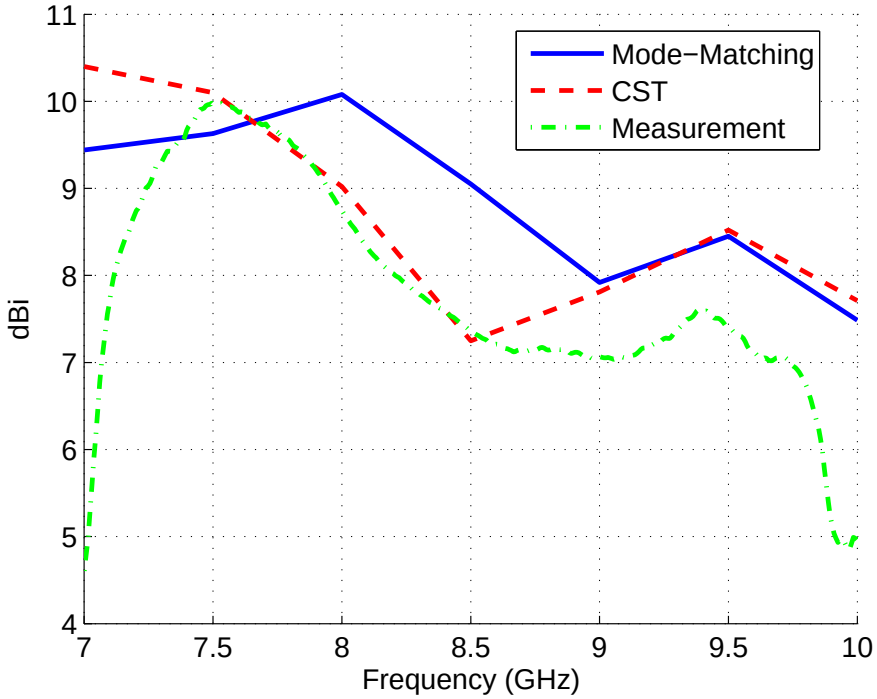

Figure 7.12: Directivity (Mode-Matching and CST) and directive gain (Measurement) of the choke horn at different frequencies.

8

Conclusions and Future Work

8.1 Conclusions

This work has been focused on the fast and low-cost prototyping of horn antennas. In order to achieve this two parallel and complementary work, two main paths have been set: one related with software (electromagnetic modelling translated into computational code) and other related with hardware (implementation of the 3D models with low-cost tools).

The software path has been devoted to the creation of a tool for efficient horn antenna analysis and simulation using the Mode-Matching method. Thanks to the use of a quasi-analytical method, the achieved computation times are significantly shorter than those achieved by commercial (general purpose) tools. This work improves the previous implementation of this formulation, to overcome some of its limitations and increase its accuracy and its applicability to new types of geometries.

Since horn antennas have a lot of similarities with waveguides, their study requires the understanding of waveguide modes. Therefore the earlier stages of this work were dedicated to study them and to the development of a formulation with general expressions that would allow to implement software models as complete as possible. This is a very important part in the work, since it required to study different sources and make our own derivations because the expressions were not fully detailed in the technical literature.

The next step consisted in computing the radiation integrals of both circular and rectangular apertures for an electromagnetic field composed by an arbitrary set of modes. These integrations have been computed for a general case where the approximation of great apertures is not used and an arbitrary set of modes at the aperture is considered. The obtained formulas will be used in the developed software to compute the radiation pattern of the horn antenna. The derivation of this formulation is another part of this work to remark since the literature does not usually cover these derivations with enough detail (typically the general problem is formulated along with the particularization of the equations for a simplified case where only the fundamental mode is considered).

Two different topologies have been presented for horn antenna simulation using the Mode-

Matching technique. Since the first one proved itself not enough accurate for certain problems, a more sophisticated model was developed using a combination of Perfect Electric Wall and Perfect Magnetic Wall boundary conditions. This advanced model has shown that it can provide with simulation results as good as commercial tools even in extreme conditions where the simple approach began to fail.

It is important to note that the main advantage of the developed simulation tool is the high efficiency of the numerical method used. Therefore this software demands far less computational resources than other commercial and general purpose tools.

As a final experiment in the software path, the developed software has been modified to create a prototype for a choke horn simulator. The simulations performed with this tool have shown good agreement with the reference models.

The hardware path has been focused on creating a construction process that will allow to manufacture horn antennas in a fast and inexpensive way, using only the facilities in our research group. This process is based on a 3D printer and it consists in constructing the profile of the horn using plastic and later apply a metallization layer using a silver paint. This manufacturing process has proved to be fairly precise since the measurements of the constructed devices match the simulated values with great accuracy. Another advantage of this technique is that it allows to construct a waveguide device in less than twenty four hours without the need of external labour.

A pyramidal horn antenna has been constructed using this procedure and also it has been measured using the equipments available at EPS-UAM. The obtained measurements show great agreement with the simulation results provided by the Mode-Matching tool and therefore it set the basis to try the construction of other waveguide devices.

The same process has been used to construct a rectangular waveguide with good results. It has even been applied to the manufacturing of more advanced devices like gap waveguides or choke horns, all of whom have shown a good agreement between the measured and simulated values.

This work, therefore, has presented two convergent work flows that join the advanced modelling of microwave devices with the newest and trendiest manufacturing techniques.

8.2 Future Work

The software developed in this work is very sophisticated and it allows to study the effect of higher order modes in an RF chain feeding a horn antenna. Of course it could also be used as a complementary tool to those that are already being used or it could even be extended to the teaching environment. Low cost manufacturing by 3D printing can be used for implementing true three-dimensional structures, while common undergraduate courses usually have an experimental part based only on planar technology as microstrip.

This work has also opened a future work door in the field of device manufacturing. The excellent results obtained for all of the constructed devices shows a promising research path that is almost unexplored.

Glossary

- **Antenna**: A device used to radiate or receive electromagnetic waves.
- **Beamwidth**: Angular distance measured on the radiation pattern between points of a given power value.
- **Corrugations**: At a horn antenna. Slots carved at the inner surface of the horn. They produce the effect of having the same radiation pattern at both main planes.
- **Directivity**: Of an antenna. Relation between the power density radiated in the direction of strongest emission versus the power density radiated by an isotropical antenna.
- **Evanescent mode**: A waveguide mode that it is not propagating at the operation frequency. They may appear next to discontinuities or next to the generator but they do not travel far since they become attenuated quickly.
- **Far field**: Electromagnetic region far from the antenna where the radiation pattern does not change with the distance.
- **Fundamental mode**: Of a transmission medium. The mode with the lowest cutoff frequency.
- **GSM**: Stands for Generalized Scattering Matrix. The term *Generalized* refers to the fact that the matrix takes on account not only propagating modes but the evanescent ones too.
- **High order mode**: Of a transmission medium. All the modes that are not the fundamental.
- **Horn**: Antenna composed by a flaring waveguide. They present high directivity values and low losses.
- **Main lobe**: Of a radiation pattern, the lobe with the greatest value.
- **Microwave**: Range of the electromagnetic spectrum from $300MHz$ to $300GHz$.
- **Mode-Matching**: Quasi-analytical waveguide analysis method.
- **PEC**: Stands for Perfect Electric Conductor.
- **PMC**: Stands for Perfect Magnetic Conductor.
- **Propagating mode**: A waveguide mode that is propagating at the operation frequency.
- **Radiation pattern**: Of an antenna. Representation of how the radiated power variates with the angular direction.

- **Scattering matrix**: Matrix that relates the power waves incident and scattered at the different ports of a device.
- **Side lobe**: Of a radiation pattern. All the lobes that are not the main lobe.
- **TE**: Of a waveguide mode. Stands for "Transverse Electric", meaning that the electric field does not have a component along the propagation direction.
- **TM**: Of a waveguide mode. Stands for "Transverse Magnetic", meaning that the magnetic field does not have a component along the propagation direction.
- **Waveguide**: Metallic pipe used as a transmission medium.
- **Waveguide mode**: Each of the solutions of the wave equation inside a waveguide.

Bibliography

[1] L. Polo López. "Análisis y diseño de antenas de bocina con perfiles arbitrarios mediante análisis modal". B.S. Thesis, Universidad Autónoma de Madrid, Escuela Politécnica Superior, June 2014.

[2] J.A. Ruiz-Cruz, J.R. Montejo-Garai, and J.M. Rebollar. *Passive Microwave Components and Antennas*, chapter "Computer Aided Design of Waveguide Devices by Mode-Matching Methods". In-Tech, 2010.

[3] T.A. Milligan. *Modern Antenna Design.* Wiley, 2005.

[4] C.A. Balanis. *Antenna Theory: Analysis and Design.* Wiley, 2015.

[5] A. Ludwig. "Radiation pattern synthesis for circular aperture horn antennas". *IEEE Transactions on Antennas and Propagation*, 14(4):434–440, Jul 1966.

[6] C.A. Leal Sevillano. "Análisis de bocinas mediante el método de Ajuste Modal". Personal Communication (Notes from a Master course).

[7] C. Barnatt. *3D Printing: The Next Industrial Revolution.* ExplainingTheFuture.com, 2013.

[8] D.M. Pozar. *Microwave Engineering.* Wiley, 2004.

[9] R.E. Collin. *Foundations for Microwave Engineering, 2nd Edition.* Wiley India Pvt. Limited, 2007.

[10] J. Uher, J. Bornemann, and U. Rosenberg. *Waveguide Components for Antenna Feed Systems: Theory and CAD.* Artech House Antennas and Propagation Library. Artech House, 1993.

[11] Warren L. Stutzman and G.A. Thiele. *Antenna theory and design.* J. Wiley, 1998.

[12] F. Bowman. *Introduction to Bessel Functions.* Dover Books on Mathematics. Dover Publications, 1958.

[13] F. Muhammad, H. Khan, and N. Saeed. "Design and simulation of high gain, low loss X-band pyramidal horn antenna for broadband applications". *City University Research Journal*, 02(02):138–146, Jul 2012.

[14] J. D. Baños-Polglase and J. M. Rebollar. "Coaxial probes with finite ground plane". *Electronics Letters*, 24(5):291–292, Mar 1988.

[15] Z. Shen and R. H. MacPhie. "Input admittance of a multilayer insulated monopole antenna". *IEEE Transactions on Antennas and Propagation*, 46(11):1679–1686, Nov 1998.

[16] Z. Shen. *Modal expansion analysis of monopole and microstrip antennas.* PhD thesis, University of Waterloo, 1998.

[17] J. M. Reiter and F. Arndt. "Full-wave analysis of circular waveguide horn antennas including the outer wall geometry with an hybrid MM/BCMM method". In *Antennas and Propagation Society International Symposium, 1996. AP-S. Digest*, volume 3, pages 1984–1987 vol.3, July 1996.

[18] Spinner Group. Cross reference for hollow metallic waveguides, August 2014. Retrieved from `http://www.spinner-group.com/upload/TD_00036_2782.pdf`.

[19] P.-S. Kildal, E. Alfonso, A. Valero-Nogueira, and E. Rajo-Iglesias. "Local Metamaterial-Based Waveguides in Gaps Between Parallel Metal Plates". *Antennas and Wireless Propagation Letters, IEEE*, 8:84–87, 2009.

[20] H. Raza, Jian Yang, P.-S. Kildal, and E. Alfonso. Resemblance between gap waveguides and hollow waveguides. *Microwaves, Antennas Propagation, IET*, 7(15):1221–1227, December 2013.

[21] A.D. Olver, P.J.B Clarricoats, A.A. Kishk, and L. Shafai. *Microwave Horns and Feeds*. Electromagnetic waves series. IEE, 1994.

[22] P.S. Kildal. Waveguides and transmission lines in gaps between parallel conducting surfaces, July 28 2011. US Patent App. 13/002,950.

[23] A. Kumar. "Reduce cross-polarization in reflector-type antennas". *Microwaves*, 17:48–51, March 1978.

A

Radiation Integral of a Rectangular Aperture

A.1 Electric Field at the Aperture

The expressions for the TE and TM modes of a rectangular waveguide have been developed in chapter 2.

$$E_{x'} = \frac{j\omega\mu n\pi}{k_c^2 b}\cos\left(\frac{m\pi x'}{a}+\frac{m\pi}{2}\right)\sin\left(\frac{n\pi y'}{b}+\frac{n\pi}{2}\right) \tag{A.1}$$

$$E_{y'} = \frac{j\omega\mu m\pi}{k_c^2 a}\sin\left(\frac{m\pi x'}{a}+\frac{m\pi}{2}\right)\cos\left(\frac{n\pi y'}{b}+\frac{n\pi}{2}\right), \tag{A.2}$$

for the TE modes and

$$E_{x'} = \frac{-\gamma m\pi}{k_c^2 a}\cos\left(\frac{m\pi x'}{a}+\frac{m\pi}{2}\right)\sin\left(\frac{n\pi y'}{b}+\frac{n\pi}{2}\right) \tag{A.3}$$

$$E_{y'} = \frac{\gamma n\pi}{k_c^2 b}\sin\left(\frac{m\pi x'}{a}+\frac{m\pi}{2}\right)\cos\left(\frac{n\pi y'}{b}+\frac{n\pi}{2}\right), \tag{A.4}$$

for the TM modes (Note that the z component is not relevant for this problem). Therefore:

$$\vec{\mathbf{E}}_{t,ap,TE} = \frac{j\omega\mu n\pi}{k_c^2 b}\cos\left(\frac{m\pi x'}{a}+\frac{m\pi}{2}\right)\sin\left(\frac{n\pi y'}{b}+\frac{n\pi}{2}\right)\hat{\mathbf{x}}' \tag{A.5}$$

$$+\frac{j\omega\mu m\pi}{k_c^2 a}\sin\left(\frac{m\pi x'}{a}+\frac{m\pi}{2}\right)\cos\left(\frac{n\pi y'}{b}+\frac{n\pi}{2}\right)\hat{\mathbf{y}}' \tag{A.6}$$

$$\vec{\mathbf{E}}_{t,ap,TM} = \frac{-\gamma m\pi}{k_c^2 a}\cos\left(\frac{m\pi x'}{a}+\frac{m\pi}{2}\right)\sin\left(\frac{n\pi y'}{b}+\frac{n\pi}{2}\right)\hat{\mathbf{x}}' \tag{A.7}$$

$$+\frac{\gamma n\pi}{k_c^2 b}\sin\left(\frac{m\pi x'}{a}+\frac{m\pi}{2}\right)\cos\left(\frac{n\pi y'}{b}+\frac{n\pi}{2}\right)\hat{\mathbf{y}}' \tag{A.8}$$

It is important to mention that in this case the coordinate origin has been translated from the corner of the waveguide to its centre (terms $\frac{n\pi}{2}$ and $\frac{m\pi}{2}$ in the arguments of the sinusoids. This has been done to simplify the following integrations.

A.2 Integration of the Field at the Aperture

The components of the electric field presented on the previous section are used to compute the values of P_x and P_y described in Section 4.2.

To tackle this task the following integrations will prove useful:

$$s(k_1,k_2,k_3,\tau) = \int \sin(k_1\tau + k_3)e^{jk_2\tau}d\tau = \tag{A.9}$$

$$= -\frac{k_1 e^{jk_2\tau}\cos(k_3+\tau k_1) - jk_2 e^{jk_2\tau}\sin(k_3+\tau k_1)}{k_1^2-k_2^2}, \tag{A.10}$$

$$c(k_1,k_2,k_3,\tau) = \int \cos(k_1\tau + k_3)e^{jk_2\tau}d\tau = \tag{A.11}$$

$$= \frac{k_1 e^{jk_2\tau}\sin(k_3+\tau k_1) + jk_2 e^{jk_2\tau}\cos(k_3+\tau k_1)}{k_1^2-k_2^2}. \tag{A.12}$$

The procedure starts with the TE modes, inserting (3.12) and (3.13) in (3.7) and (3.8) respectively:

$$P_{x,TE} = \int_{y'=-b/2}^{b/2}\int_{x'=-a/2}^{a/2} E_{ap,x}e^{jk(x'\sin(\theta)\cos(\phi)+y'\sin(\theta)\sin(\phi))}dx'dy' = \tag{A.13}$$

$$= \frac{j\omega\mu n\pi}{k_c^2 b}\int_{y'=-b/2}^{b/2}\sin\left(\frac{n\pi y'}{b}+\frac{n\pi}{2}\right)e^{jky'\sin(\theta)\sin(\phi)}dy' \tag{A.14}$$

$$\int_{x'=-a/2}^{a/2}\cos\left(\frac{m\pi x'}{a}+\frac{m\pi}{2}\right)e^{jkx'\sin(\theta)\cos(\phi)}dx' = \tag{A.15}$$

$$= \frac{j\omega\mu n\pi}{k_c^2 b}\left\{\left[s\left(\frac{n\pi}{b},k\sin(\theta)\sin(\phi),\frac{n\pi}{2},\frac{b}{2}\right) - s\left(\frac{n\pi}{b},k\sin(\theta)\sin(\phi),\frac{n\pi}{2},\frac{-b}{2}\right)\right]\right. \tag{A.16}$$

$$\left.\cdot\left[c\left(\frac{m\pi}{a},k\sin(\theta)\cos(\phi),\frac{m\pi}{2},\frac{a}{2}\right) - c\left(\frac{m\pi}{a},k\sin(\theta)\cos(\phi),\frac{m\pi}{2},\frac{-a}{2}\right)\right]\right\}, \tag{A.17}$$

and

$$P_{y,TE} = \int_{y'=-b/2}^{b/2}\int_{x'=-a/2}^{a/2} E_{ap,y}e^{jk(x'\sin(\theta)\cos(\phi)+y'\sin(\theta)\sin(\phi))}dx'dy' = \tag{A.18}$$

$$= \frac{j\omega\mu m\pi}{k_c^2 a}\int_{y'=-b/2}^{b/2}\cos\left(\frac{n\pi y'}{b}+\frac{n\pi}{2}\right)e^{jky'\sin(\theta)\sin(\phi)}dy' \tag{A.19}$$

$$\int_{x'=-a/2}^{a/2}\sin\left(\frac{m\pi x'}{a}+\frac{m\pi}{2}\right)e^{jkx'\sin(\theta)\cos(\phi)}dx' = \tag{A.20}$$

$$= \frac{j\omega\mu m\pi}{k_c^2 a}\left\{\left[c\left(\frac{n\pi}{b},k\sin(\theta)\sin(\phi),\frac{n\pi}{2},\frac{b}{2}\right) - c\left(\frac{n\pi}{b},k\sin(\theta)\sin(\phi),\frac{n\pi}{2},\frac{-b}{2}\right)\right]\right. \tag{A.21}$$

$$\left.\cdot\left[s\left(\frac{m\pi}{a},k\sin(\theta)\cos(\phi),\frac{m\pi}{2},\frac{a}{2}\right) - s\left(\frac{m\pi}{a},k\sin(\theta)\cos(\phi),\frac{m\pi}{2},\frac{-a}{2}\right)\right]\right\}, \tag{A.22}$$

Operating similarly for the TM modes:

$$P_{x,TM} = \int_{y'=-b/2}^{b/2} \int_{x'=-a/2}^{a/2} E_{ap,x} e^{jk(x' \sin(\theta)\cos(\phi) + y' \sin(\theta)\sin(\phi))} dx' dy' = \tag{A.23}$$

$$= \frac{-\gamma m\pi}{k_c^2 a} \int_{y'=-b/2}^{b/2} \sin\left(\frac{n\pi y'}{b} + \frac{n\pi}{2}\right) e^{jky' \sin(\theta)\sin(\phi)} dy' \tag{A.24}$$

$$\int_{x'=-a/2}^{a/2} \cos\left(\frac{m\pi x'}{a} + \frac{m\pi}{2}\right) e^{jkx' \sin(\theta)\cos(\phi)} dx' = \tag{A.25}$$

$$= \frac{-\gamma m\pi}{k_c^2 a} \left\{ \left[s\left(\frac{n\pi}{b}, k\sin(\theta)\sin(\phi), \frac{n\pi}{2}, \frac{b}{2}\right) - s\left(\frac{n\pi}{b}, k\sin(\theta)\sin(\phi), \frac{n\pi}{2}, \frac{-b}{2}\right) \right] \right. \tag{A.26}$$

$$\left. \cdot \left[c\left(\frac{m\pi}{a}, k\sin(\theta)\cos(\phi), \frac{m\pi}{2}, \frac{a}{2}\right) - c\left(\frac{m\pi}{a}, k\sin(\theta)\cos(\phi), \frac{m\pi}{2}, \frac{-a}{2}\right) \right] \right\}, \tag{A.27}$$

and

$$P_{y,TM} = \int_{y'=-b/2}^{b/2} \int_{x'=-a/2}^{a/2} E_{ap,y} e^{jk(x' \sin(\theta)\cos(\phi) + y' \sin(\theta)\sin(\phi))} dx' dy' = \tag{A.28}$$

$$= \frac{\gamma n\pi}{k_c^2 b} \int_{y'=-b/2}^{b/2} \cos\left(\frac{n\pi y'}{b} + \frac{n\pi}{2}\right) e^{jky' \sin(\theta)\sin(\phi)} dy' \tag{A.29}$$

$$\int_{x'=-a/2}^{a/2} \sin\left(\frac{m\pi x'}{a} + \frac{m\pi}{2}\right) e^{jkx' \sin(\theta)\cos(\phi)} dx' = \tag{A.30}$$

$$= \frac{\gamma n\pi}{k_c^2 b} \left\{ \left[c\left(\frac{n\pi}{b}, k\sin(\theta)\sin(\phi), \frac{n\pi}{2}, \frac{b}{2}\right) - c\left(\frac{n\pi}{b}, k\sin(\theta)\sin(\phi), \frac{n\pi}{2}, \frac{-b}{2}\right) \right] \right. \tag{A.31}$$

$$\left. \cdot \left[s\left(\frac{m\pi}{a}, k\sin(\theta)\cos(\phi), \frac{m\pi}{2}, \frac{a}{2}\right) - s\left(\frac{m\pi}{a}, k\sin(\theta)\cos(\phi), \frac{m\pi}{2}, \frac{-a}{2}\right) \right] \right\}. \tag{A.32}$$

Q_x and Q_y can be obtained using the relations in (3.11) without the need to compute any new integrations.

B

Radiation Integral of a Circular Aperture

B.1 Electric Field at the Aperture

The expressions for the TE and TM modes of a circular waveguide have been developed in Chapter 2. The components needed now for TE modes are:

$$E_{\rho'} = \frac{-j\omega\mu n}{k_c^2\rho'} C_n(k_c\rho') \begin{pmatrix} -\sin(n\phi') \\ \cos(n\phi') \end{pmatrix} \tag{B.1}$$

$$E_{\phi'} = \frac{j\omega\mu}{k_c} C_n'(k_c\rho') \begin{pmatrix} \cos(n\phi') \\ \sin(n\phi') \end{pmatrix}. \tag{B.2}$$

The components needed for TM modes are:

$$E_{\rho'} = \frac{-\gamma}{k_c} C_n'(k_c\rho') \begin{pmatrix} \cos(n\phi') \\ \sin(n\phi') \end{pmatrix} \tag{B.3}$$

$$E_{\phi'} = \frac{-\gamma n}{k_c^2\rho'} C_n(k_c\rho') \begin{pmatrix} -\sin(n\phi') \\ \cos(n\phi') \end{pmatrix}. \tag{B.4}$$

And therefore:

$$\vec{\mathbf{E}}_{ap,TE} = \frac{-j\omega\mu n}{k_c^2\rho'} C_n(k_c\rho') \begin{pmatrix} -\sin(n\phi') \\ \cos(n\phi') \end{pmatrix} \hat{\rho}' + \frac{j\omega\mu}{k_c} C_n'(k_c\rho') \begin{pmatrix} \cos(n\phi') \\ \sin(n\phi') \end{pmatrix} \hat{\phi}' \tag{B.5}$$

$$\vec{\mathbf{E}}_{ap,TM} = \frac{-\gamma}{k_c} C_n'(k_c\rho') \begin{pmatrix} \cos(n\phi') \\ \sin(n\phi') \end{pmatrix} \hat{\rho}' + \frac{-\gamma n}{k_c^2\rho'} C_n(k_c\rho') \begin{pmatrix} -\sin(n\phi') \\ \cos(n\phi') \end{pmatrix} \hat{\phi}' \tag{B.6}$$

B.1.1 Vectors in Rectangular Coordinates

The formulas for the different equivalence principles are developed for an electromagnetic field written in a rectangular coordinates system, but the expressions of the modes presented above

are written with vectors in a cylindrical coordinates system. To juggle both formulations the previous expressions have to be written on a rectangular coordinates using the following transformation:

$$\begin{cases} \hat{\rho}' = \cos(\phi')\hat{\mathbf{x}}' + \sin(\phi')\hat{\mathbf{y}}' & \text{(B.7)} \\ \hat{\phi}' = -\sin(\phi')\hat{\mathbf{x}}' + \cos(\phi')\hat{\mathbf{y}}' & \text{(B.8)} \end{cases}$$

TE Modes

The resultant expression of (B.5) after applying (B.7) and (B.8) is:

$$\vec{\mathbf{E}}_{ap,TE} = \frac{-j\omega\mu n}{k_c^2\rho'} C_n(k_c\rho') \begin{pmatrix} -\sin(n\phi') \\ \cos(n\phi') \end{pmatrix} [\cos(\phi')\hat{\mathbf{x}}' + \sin(\phi')\hat{\mathbf{y}}'] \quad \text{(B.9)}$$

$$+\frac{j\omega\mu}{k_c} C_n'(k_c\rho') \begin{pmatrix} \cos(n\phi') \\ \sin(n\phi') \end{pmatrix} [-\sin(\phi')\hat{\mathbf{x}}' + \cos(\phi')\hat{\mathbf{y}}']. \quad \text{(B.10)}$$

And the electric field for each coordinate can be written as:

$$E_{ap,x} = \frac{-j\omega\mu n}{k_c^2\rho'} C_n(k_c\rho') \begin{pmatrix} -\sin(n\phi') \\ \cos(n\phi') \end{pmatrix} \cos(\phi') - \frac{j\omega\mu}{k_c} C_n'(k_c\rho') \begin{pmatrix} \cos(n\phi') \\ \sin(n\phi') \end{pmatrix} \sin(\phi') = \quad \text{(B.11)}$$

$$= \frac{-j\omega\mu}{k_c} \left[\frac{n}{k_c\rho'} C_n(k_c\rho') \begin{pmatrix} -\sin(n\phi) \\ \cos(n\phi) \end{pmatrix} \cos(\phi') + C_n'(k_c\rho') \begin{pmatrix} \cos(n\phi) \\ \sin(n\phi) \end{pmatrix} \sin(\phi') \right] = \quad \text{(B.12)}$$

$$= \frac{-j\omega\mu}{k_c} \left[\frac{1}{2} \left(C_{n-1}(k_c\rho') + C_{n+1}(k_c\rho') \right) \begin{pmatrix} -\sin(n\phi') \\ \cos(n\phi') \end{pmatrix} \cos(\phi') + \right. \quad \text{(B.13)}$$

$$\left. \frac{1}{2} \left(C_{n-1}(k_c\rho') - C_{n+1}(k_c\rho') \right) \begin{pmatrix} \cos(n\phi') \\ \sin(n\phi') \end{pmatrix} \sin(\phi') \right] = \quad \text{(B.14)}$$

$$= \frac{-j\omega\mu}{2k_c} \left\{ C_{n-1}(k_c\rho') \left[\begin{pmatrix} -\sin(n\phi') \\ \cos(n\phi') \end{pmatrix} \cos(\phi') + \begin{pmatrix} \cos(n\phi') \\ \sin(n\phi') \end{pmatrix} \sin(\phi') \right] + \right. \quad \text{(B.15)}$$

$$\left. C_{n+1}(k_c\rho') \left[\begin{pmatrix} -\sin(n\phi') \\ \cos(n\phi') \end{pmatrix} \cos(\phi') - \begin{pmatrix} \cos(n\phi') \\ \sin(n\phi') \end{pmatrix} \sin(\phi') \right] \right\} = \quad \text{(B.16)}$$

$$= \frac{-j\omega\mu}{2k_c} \left[C_{n-1}(k_c\rho') \begin{pmatrix} -\sin((n-1)\phi') \\ \cos((n-1)\phi') \end{pmatrix} + C_{n+1}(k_c\rho') \begin{pmatrix} -\sin((n-1)\phi') \\ \cos((n-1)\phi') \end{pmatrix} \right] \quad \text{(B.17)}$$

$$E_{ap,y} = \frac{-j\omega\mu n}{k_c^2\rho'} C_n(k_c\rho') \begin{pmatrix} -\sin(n\phi') \\ \cos(n\phi') \end{pmatrix} \sin(\phi') + \frac{j\omega\mu}{k_c} C_n'(k_c\rho') \begin{pmatrix} \cos(n\phi') \\ \sin(n\phi') \end{pmatrix} \cos(\phi') = \tag{B.18}$$

$$= \frac{-j\omega\mu}{k_c} \left[\frac{n}{k_c\rho'} C_n(k_c\rho') \begin{pmatrix} -\sin(n\phi) \\ \cos(n\phi) \end{pmatrix} \sin(\phi') - C_n'(k_c\rho') \begin{pmatrix} \cos(n\phi) \\ \sin(n\phi) \end{pmatrix} \cos(\phi') \right] = \tag{B.19}$$

$$= \frac{-j\omega\mu}{k_c} \left\{ \frac{1}{2} \left[C_{n-1}(k_c\rho') + C_{n+1}(k_c\rho') \right] \begin{pmatrix} -\sin(n\phi') \\ \cos(n\phi') \end{pmatrix} \sin(\phi') - \right. \tag{B.20}$$

$$\left. \frac{1}{2} \left[C_{n-1}(k_c\rho') - C_{n+1}(k_c\rho') \right] \begin{pmatrix} \cos(n\phi') \\ \sin(n\phi') \end{pmatrix} \cos(\phi') \right\} = \tag{B.21}$$

$$= \frac{-j\omega\mu}{2k_c} \left\{ C_{n-1}(k_c\rho') \left[\begin{pmatrix} -\sin(n\phi') \\ \cos(n\phi') \end{pmatrix} \sin(\phi') - \begin{pmatrix} \cos(n\phi') \\ \sin(n\phi') \end{pmatrix} \cos(\phi') \right] + \right. \tag{B.22}$$

$$\left. C_{n+1}(k_c\rho') \left[\begin{pmatrix} -\sin(n\phi') \\ \cos(n\phi') \end{pmatrix} \sin(\phi') + \begin{pmatrix} \cos(n\phi') \\ \sin(n\phi') \end{pmatrix} \cos(\phi') \right] \right\} = \tag{B.23}$$

$$= \frac{-j\omega\mu}{2k_c} \left[-C_{n-1}(k_c\rho') \begin{pmatrix} \cos((n-1)\phi') \\ \sin((n-1)\phi') \end{pmatrix} + C_{n+1}(k_c\rho') \begin{pmatrix} \cos((n-1)\phi') \\ \sin((n-1)\phi') \end{pmatrix} \right] \tag{B.24}$$

TM Modes

The resultant expression of (B.6) after applying (B.7) and (B.8) is:

$$\vec{\mathbf{E}}_{t,ap,TM} = \frac{-\gamma}{k_c} C_n'(k_c\rho') \begin{pmatrix} \cos(n\phi') \\ \sin(n\phi') \end{pmatrix} [\cos(\phi')\hat{\mathbf{x}}' + \sin(\phi')\hat{\mathbf{y}}'] \tag{B.25}$$

$$- \frac{\gamma n}{k_c^2\rho'} C_n(k_c\rho') \begin{pmatrix} -\sin(n\phi') \\ \cos(n\phi') \end{pmatrix} [-\sin(\phi')\hat{\mathbf{x}}' + \cos(\phi')\hat{\mathbf{y}}']. \tag{B.26}$$

As it has been done for the TE modes, the electric field is separated in:

$$E_{ap,x} = \frac{-\gamma}{k_c} C_n'(k_c\rho') \begin{pmatrix} \cos(n\phi') \\ \sin(n\phi') \end{pmatrix} \cos(\phi') + \frac{\gamma n}{k_c^2\rho'} C_n(k_c\rho') \begin{pmatrix} -\sin(n\phi') \\ \cos(n\phi') \end{pmatrix} \sin(\phi') = \tag{B.27}$$

$$= \frac{-\gamma}{k_c} \left[C_n'(k_c\rho') \begin{pmatrix} \cos(n\phi') \\ \sin(n\phi') \end{pmatrix} \cos(\phi') - \frac{n}{k_c\rho'} C_n(k_c\rho') \begin{pmatrix} -\sin(n\phi') \\ \cos(n\phi') \end{pmatrix} \sin(\phi') \right] = \tag{B.28}$$

$$= \frac{-\gamma}{k_c} \left\{ \frac{1}{2} \left[C_{n-1}(k_c\rho') - C_{n+1}(k_c\rho') \right] \begin{pmatrix} \cos(n\phi') \\ \sin(n\phi') \end{pmatrix} \cos(\phi') \right. \tag{B.29}$$

$$\left. - \frac{1}{2} \left[C_{n-1}(k_c\rho') + C_{n+1}(k_c\rho') \right] \begin{pmatrix} -\sin(n\phi') \\ \cos(n\phi') \end{pmatrix} \sin(\phi') \right\} = \tag{B.30}$$

$$= \frac{-\gamma}{2k_c} \left\{ C_{n-1}(k_c\rho') \left[\begin{pmatrix} \cos(n\phi') \\ \sin(n\phi') \end{pmatrix} \cos(\phi') - \begin{pmatrix} -\sin(n\phi') \\ \cos(n\phi') \end{pmatrix} \sin(\phi') \right] \right. \tag{B.31}$$

$$\left. - C_{n+1}(k_c\rho') \left[\begin{pmatrix} \cos(n\phi') \\ \sin(n\phi') \end{pmatrix} \cos(\phi') + \begin{pmatrix} -\sin(n\phi') \\ \cos(n\phi') \end{pmatrix} \sin(\phi') \right] \right\} = \tag{B.32}$$

$$= \frac{-\gamma}{2k_c} \left[C_{n-1}(k_c\rho') \begin{pmatrix} \cos((n-1)\phi') \\ \sin((n-1)\phi') \end{pmatrix} - C_{n+1}(k_c\rho') \begin{pmatrix} \cos((n+1)\phi') \\ \sin((n+1)\phi') \end{pmatrix} \right] \tag{B.33}$$

$$E_{ap,y} = \frac{-\gamma}{k_c} C_n'(k_c\rho') \begin{pmatrix} \cos(n\phi') \\ \sin(n\phi') \end{pmatrix} \sin(\phi') - \frac{\gamma n}{k_c^2 \rho'} C_n(k_c\rho') \begin{pmatrix} -\sin(n\phi') \\ \cos(n\phi') \end{pmatrix} \cos(\phi') = \tag{B.34}$$

$$= \frac{-\gamma}{k_c} \left[C_n'(k_c\rho') \begin{pmatrix} \cos(n\phi') \\ \sin(n\phi') \end{pmatrix} \sin(\phi') + \frac{n}{k_c\rho'} C_n(k_c\rho') \begin{pmatrix} -\sin(n\phi') \\ \cos(n\phi') \end{pmatrix} \cos(\phi') \right] = \tag{B.35}$$

$$= \frac{-\gamma}{k_c} \left\{ \frac{1}{2} \left[C_{n-1}(k_c\rho') - C_{n+1}(k_c\rho') \right] \begin{pmatrix} \cos(n\phi') \\ \sin(n\phi') \end{pmatrix} \sin(\phi') \right. \tag{B.36}$$

$$\left. + \frac{1}{2} \left[C_{n-1}(k_c\rho') + C_{n+1}(k_c\rho') \right] \begin{pmatrix} -\sin(n\phi') \\ \cos(n\phi') \end{pmatrix} \cos(\phi') \right\} = \tag{B.37}$$

$$= \frac{-\gamma}{2k_c} \left\{ C_{n-1}(k_c\rho') \left[\begin{pmatrix} \cos(n\phi') \\ \sin(n\phi') \end{pmatrix} \sin(\phi') + \begin{pmatrix} -\sin(n\phi') \\ \cos(n\phi') \end{pmatrix} \cos(\phi') \right] \right. \tag{B.38}$$

$$\left. - C_{n+1}(k_c\rho') \left[\begin{pmatrix} \cos(n\phi') \\ \sin(n\phi') \end{pmatrix} \sin(\phi') - \begin{pmatrix} -\sin(n\phi') \\ \cos(n\phi') \end{pmatrix} \cos(\phi') \right] \right\} = \tag{B.39}$$

$$= \frac{-\gamma}{2k_c} \left[C_{n-1}(k_c\rho') \begin{pmatrix} -\sin((n-1)\phi') \\ \cos((n-1)\phi') \end{pmatrix} - C_{n+1}(k_c\rho') \begin{pmatrix} \sin((n+1)\phi') \\ -\cos((n+1)\phi') \end{pmatrix} \right] = \tag{B.40}$$

$$= \frac{-\gamma}{2k_c} \left[C_{n-1}(k_c\rho') \begin{pmatrix} -\sin((n-1)\phi') \\ \cos((n-1)\phi') \end{pmatrix} + C_{n+1}(k_c\rho') \begin{pmatrix} -\sin((n+1)\phi') \\ \cos((n+1)\phi') \end{pmatrix} \right] \tag{B.41}$$

B.2 Integration of the Field at the Aperture

The components of the electric field presented on the previous section are used to compute the values of P_x and P_y described in section 3.2.

Defining

$$b_{n,\binom{c}{s}}(\theta,\phi) = \int_{\phi'=-\pi}^{\pi} \int_{\rho'=r_i}^{r_e} C_n(k_c\rho') \begin{pmatrix} \cos(n\phi') \\ \sin(n\phi') \end{pmatrix} e^{jk\rho' \sin(\theta)\cos(\phi-\phi')} \rho' d\rho' d\phi' = \tag{B.42}$$

$$= \begin{pmatrix} \cos(n\phi) \\ \sin(n\phi) \end{pmatrix} \frac{(2\pi j^n)}{k_c^2 - k_\theta^2} \left[\xi k \sin(\theta) C_n(k_c\xi) J_n'(k_\theta\xi) - \xi k_c C_n'(k_c\xi) J_n(k_\theta\xi) \right]_{\xi=r_i}^{\xi=r_e}, \tag{B.43}$$

where the Lommel Integral has been used [12]. Note that the integration is defined between an internal and external radius. This is the general expression that also includes the case of a coaxial aperture, the result for a circular aperture can be obtained by making $r_i = 0$. For the TE modes the integrations can be calculated as follows:

$$P_{x,TE} = \int_{\phi'=-\pi}^{\pi} \int_{\rho'=r_i}^{r_e} E_{ap,x\binom{-s}{c}} e^{jk\rho' \sin(\theta)\cos(\phi-\phi')} \rho' d\rho' d\phi' = \tag{B.44}$$

$$= \frac{-j\omega\mu}{2k_c} \int_{\phi'=-\pi}^{\pi} \int_{\rho'=r_i}^{r_e} \left[C_{n-1}(k_c\rho') \begin{pmatrix} -\sin((n-1)\phi') \\ \cos((n-1)\phi') \end{pmatrix} \right. \tag{B.45}$$

$$\left. + C_{n+1}(k_c\rho') \begin{pmatrix} -\sin((n+1)\phi') \\ \cos((n+1)\phi') \end{pmatrix} \right] e^{jk\rho' \sin(\theta)\cos(\phi-\phi')} \rho' d\rho' d\phi' = \tag{B.46}$$

$$= \frac{-j\omega\mu}{2k_c} \left(b_{n-1,\binom{-s}{c}}(\theta,\phi) + b_{n+1,\binom{-s}{c}}(\theta,\phi) \right), \tag{B.47}$$

and

$$P_{y,TE} = \int_{\phi'=-\pi}^{\pi} \int_{\rho'=r_i}^{r_e} E_{ap,y\binom{c}{s}} e^{jk\rho' \sin(\theta)\cos(\phi-\phi')} \rho' d\rho' d\phi' = \tag{B.48}$$

$$= \frac{-j\omega\mu}{2k_c} \int_{\phi'=-\pi}^{\pi} \int_{\rho'=r_i}^{r_e} \left[-C_{n-1}(k_c\rho') \begin{pmatrix} \cos((n-1)\phi') \\ \sin((n-1)\phi') \end{pmatrix} \right. \tag{B.49}$$

$$\left. + C_{n+1}(k_c\rho') \begin{pmatrix} \cos((n+1)\phi') \\ \sin((n+1)\phi') \end{pmatrix} \right] e^{jk\rho' \sin(\theta)\cos(\phi-\phi')} \rho' d\rho' d\phi' = \tag{B.50}$$

$$= \frac{-j\omega\mu}{2k_c} \left(-b_{n-1,\binom{c}{s}}(\theta,\phi) + b_{n+1,\binom{c}{s}}(\theta,\phi) \right). \tag{B.51}$$

Operating similarly for the TM modes:

$$P_{x,TM} = \int_{\phi'=-\pi}^{\pi} \int_{\rho'=r_i}^{r_e} E_{ap,x\binom{c}{s}} e^{jk\rho' \sin(\theta)\cos(\phi-\phi')} \rho' d\rho' d\phi' = \tag{B.52}$$

$$= \frac{-\gamma}{2k_c} \int_{\phi'=-\pi}^{\pi} \int_{\rho'=r_i}^{r_e} \left[C_{n-1}(k_c\rho') \begin{pmatrix} \cos((n-1)\phi') \\ \sin((n-1)\phi') \end{pmatrix} \right. \tag{B.53}$$

$$\left. - C_{n+1}(k_c\rho') \begin{pmatrix} \cos((n+1)\phi') \\ \sin((n+1)\phi') \end{pmatrix} \right] e^{jk\rho' \sin(\theta)\cos(\phi-\phi')} \rho' d\rho' d\phi' = \tag{B.54}$$

$$= \frac{-\gamma}{2k_c} \left(b_{n-1,\binom{c}{s}}(\theta,\phi) - b_{n+1,\binom{c}{s}}(\theta,\phi) \right), \tag{B.55}$$

and

$$P_{y,TM} = \int_{\phi'=-\pi}^{\pi} \int_{\rho'=r_i}^{r_e} E_{ap,y\binom{-s}{c}} e^{jk\rho' \sin(\theta)\cos(\phi-\phi')} \rho' d\rho' d\phi' = \tag{B.56}$$

$$= \frac{-\gamma}{2k_c} \int_{\phi'=-\pi}^{\pi} \int_{\rho'=r_i}^{r_e} \left[C_{n-1}(k_c\rho') \begin{pmatrix} -\sin((n-1)\phi') \\ \cos((n-1)\phi') \end{pmatrix} \right. \tag{B.57}$$

$$\left. + C_{n+1}(k_c\rho') \begin{pmatrix} -\sin((n+1)\phi') \\ \cos((n+1)\phi') \end{pmatrix} \right] e^{jk\rho' \sin(\theta)\cos(\phi-\phi')} \rho' d\rho' d\phi' = \tag{B.58}$$

$$= \frac{-\gamma}{2k_c} \left(b_{n-1,\binom{-s}{c}}(\theta,\phi) + b_{n+1,\binom{-s}{c}}(\theta,\phi) \right). \tag{B.59}$$

Q_x and Q_y can be obtained using the relations in (3.11) without the need to compute any new integrations.